REDUCING UNCERTAINTY IN THE CHARACTERIZATION AND MODELING OF REACTIVE TRANSPORT PROCESSES IN BLENDED CEMENT MORTAR

By

Joshua R. Arnold

Dissertation

Submitted to the Faculty of the

Graduate School of Vanderbilt University

in partial fulfillment of the requirements

for the degree of

DOCTOR OF PHILOSOPHY

in

Environmental Engineering

May, 2014

Nashville, Tennessee

Approved:

Professor David S. Kosson

Professor Andrew C. Garrabrants

Professor John Ayers

Dr. Christine Langton

Professor J.C.L. Meeussen

Professor Florence Sanchez

Dr. Hans van der Sloot

DEDICATION

To my mother and father, without whom I should have long since perished

To my brother for continually challenging my ways of thinking, and

To my grandmother for the enthusiastic encouragement of my lifelong education.

To all my family and friends for lifting my spirits and

To the people of earth, who may hopefully benefit from this work.

ACKNOWLEDGMENT

This work was prepared with the financial support by the U. S. Department of Energy, under Cooperative Agreement Number DE-FC01-06EW07053 entitled 'The Consortium for Risk Evaluation with Stakeholder Participation III' awarded to Vanderbilt University. This research was carried out as part of the Cementitious Barriers Partnership supported by U.S. DOE Office of Environmental Management. The opinions, findings, conclusions, or recommendations expressed herein are those of the authors and do not necessarily represent the views of the Department of Energy or Vanderbilt University.

TABLE OF CONTENTS

Page

LIST OF TABLES

LIST OF FIGURES

LIST OF ABBREVIATIONS AND SYMBOLS

List of abbreviations

AN	ammonium nitrate solution
BFS	blast furnace slage
BSEM	backscatter scanning electron microscopy
C-S-H	calcium silicate hydrate
DDLP	Delon, Desolneux, Lisani, and Petro segmentation algorithm
DI	deionized water solution
EDX	enery dispersive X-ray analysis
FAF	class F fly ash
FD	finite difference
LDA	linear discriminant analysis
LEN	local electroneutral
LHS	Latin hypercube sampling
keV	kilo-electron volts
M	moles per liter
M-S-H	magnesium silicate hydrate
MIP	mercury intrusion porosimetry
MS	magnesium sulfate, $MgSO_4$
NC	sodium carbonate, Na_2CO_3
NP	Nerst-Planck
NS	sodium sulfate, Na_2SO_4
OPC	ordinary Portland cement
PBE	Poisson-Boltzmann equation
PC	Portland cement
PDE	partial differential equation
PVA	partial volume averaging
QS	quartz sand
SCM	supplementary cementitious material
SVC	structural vault concrete analogue

List of abbreviations, continued

USEPA	United States Environmental Protection Agency
w/b	water-to-binder ratio
WF	waste form solution
XRF	X-ray fluourescence

List of English symbols

C_i	concentration of species i in solution
d_{KO}	depth of electron interaction volume
D_i	phenomenolical diffusion coefficient
D_i^{obs}	observed diffusion coefficient
D_i^u	ionic diffusion coefficient
e	elementary electron charge
E_0	SEM excitation energy
F	Faraday's constant
F_i	rate of reaction of species i
J_i	flux of species i
k_B	Boltzmann's constant
K_i, K_ℓ	thermodynamic stability constant of species i, ℓ
M_p	moles of primary species p
N_A	Avogadro's number
R	ideal gas constant
R	retardation factor
S_i	sorbed concentration of species i
T	temperature
Z_{ave}	average charge
z_i	formal charge of species i

List of Greek symbols

α_q	reacted fraction of component q
γ_i	activity coefficient of species i
ϵ	dielectric constant
ϵ_0	permittivity of free space
ϵ_r	relative perimittivity coefficient
μ_i	chemical potential of species i
ρ	density
τ	tortuosity
$\nu_{pi}, \nu_{p\ell}$	stoichiometric coefficient of species p in species i, ℓ
ϕ	porosity
ψ	electric potential

CHAPTER 1

1. INTRODUCTION

1.1. Motivation

For two millennia, anecdotal knowledge has sustained the practice of cement-based construction, the success of which is evidenced by the perseverance of several iconic structures of the Roman Empire. In modern times, the requirements of cementitious structures are constantly evolving; the burgeoning demand for infrastructure in the developing world and the concomitant need to minimize environmental and economic costs can very likely only be met with the use of concrete construction. Already in the last half century, the incorporation of byproducts and "waste" materials, such as blast furnace slag, coal combustion fly ash, municipal waste ash, and a myriad of others, has become a prevalent strategy for reducing the economic and carbon costs of Portland cement production while, in some cases, simultaneously improving the physical and chemical properties of the composite cement system. Moreover, the technological advances of the last quarter-century, particularly the advent of nano-engineered materials, have spurred the quest for newer, "smarter" cementitious composites designed to suit a plethora of needs. The common thread among these novel materials, sundry as they may be, is that they push the envelope of mechanistic understanding well beyond the scope of anecdotal knowledge at a pace that empiricism struggles to maintain. It is within this envelope that the "virtual laboratory" lies; modeling allows the interplay of physico-chemical behaviors to be examined within regimes that are impractical or impossible to access through actual experimentation. The onus on the scientist and engineer, then, is to model these systems in ways which are sensitive to the variations likely to occur throughout the lifetime of the system, and this may be accomplished, perhaps most effectively, through investigation of the fundamental mechanisms that govern physico-chemical behaviors. Such an approach avails itself to the problem of uncertainty analysis especially, in that the influence of individual component mechanisms on the holistic system response may be ascertained, whereas purely empirical models may only be varied in terms of parameters that may possess little to no physical significance. Furthermore, as the understanding of fundamental mechanisms improves, this new information may be assimilated into mechanistic models with

relative ease, allowing the examination of new interconnected behaviors, and it is through the elucidation of these interconnections that the virtual laboratory proves its worth.

A prime example of mechanistic-based modeling of inaccessible regimes is the prediction of the long-term performance of cementitious barriers used in nuclear waste management applications. Such predictions assess the behavior of the engineered system with respect to both contaminant retention and structural integrity, which entails mechanistic modeling of the system's physico-chemical behavior and quantifying the uncertainty about those model predictions. The Cementitious Barriers Partnership (CBP, http://cementbarriers.org/) is charged with the task of developing software tools that aim to reduce uncertainties in the performance assessment of cementitious barriers. The CBP has made considerable progress towards its goal on three general fronts: characterization, modeling, and uncertainty quantification. A significant amount of experimental characterization has been performed by the CBP, both in defining reference cementitious materials for study, which are representative of those used in practice [1], and in the rigorous measurement of their chemical and physical properties [2-4]. Considerable progress has also been made in both demonstrating state-of-the-art modeling capabilities [5-8], improving phenomenological models [9, 10], and in quantifying the uncertainties inherent in both models and measurements [11, 12]. It is within the CBP framework that this dissertation thesis resides.

The aim of this work is to elucidate the origins and relative magnitudes of uncertainties within the *reactive transport* modeling of externally-induced aging processes in cementitious systems. An "externally-induced aging process" is herein defined as a perturbation of the physico-chemical cement-based system due to its disequilibrium with the ambient environment. Thus, autogeneous aging processes are neglected, but even so, the scope of this definition is vast. Therefore, externally-induced aging processes are further restricted to those due to aqueous phase diffusive transport between the cementitious porewater and an external reservoir, namely "leaching". The cementitious material studied in this work is a CBP reference material, a blended cement mortar supplemented with ground granulated iron blast furnace slag and coal combustion fly ash. These two supplementary cementitious materials have found widespread utility commercially as well as in nuclear waste management applications.

This work identifies critical parametric and model uncertainties within three core aspects of mechanistic reactive transport modeling for blended cementitious materials: mass transport, mass

conservation, and thermodynamic characterization. Mass transport encompasses the modeling of ionic motion due to diffusive processes, that is, the interaction of aqueous species, as well as the interaction of aqueous species with charged surfaces. Mass conservation entails the parameterization of total elemental mass which is considered to be reactive within the cementitious matrix, and thermodynamic characterization concerns the partitioning of that mass into various solid and aqueous species. Comparing and contrasting both modeling methods and experimental techniques in these core areas facilitate the identification of the origins of uncertainties.

1.2. Research Goal and Specific Objectives

The goal of the research presented here is the identification of uncertainties in the experimental characterization and simulation of aging processes in a blended cement mortar. The specific objectives are:

1. To assess the differences in predicted rate of release from cementitious materials as a result of either assuming a Fickian or Nernst-Planck-Poisson model of solute transport.
2. To model the electric double layer on idealized cementitious pore walls for measured blended cement porewater compositions and to assess the potential impacts of the electric double layer on the rate of transport through the cement pore space.
3. To develop a method of quantifying the extent of anhydrous particle reaction in blended cement mortars for the purpose of informing geochemical reactive transport modeling of cement.
4. To model the equilibrium chemistry of a blended cement mortar using thermodynamic parameters developed for the description of ordinary Portland cement systems and to assess the ability of this set of parameters to describe the blended cement chemistry by comparison to experimental data.
5. To employ reactive transport modeling to describe the transient chemical behaviors of a blended cement mortar monolith as the result of exposure to various external aging solutions and to evaluate the applicability of Portland cement thermodynamic parameters for describing this system.

In Chapter 2, the transport process itself is scrutinized, as the Fickian diffusion model is compared to the Nernst-Planck (NP) charge-coupling migration model within the context of reactive transport in a fictitious Portland cement. The application of the NP model to a reactive system with homogeneous aqueous phase reactions is, to the author's knowledge, the first of its kind for cementitious materials. In Chapter 3, the Poisson-Boltzmann equation (PBE), which describes the electrostatics of the electric double layer in the vicinity of charged surfaces, is solved for a real blended cement porewater composition without "usual and customary" assumptions that are typically not applicable to cement-based systems. With the PBE solution for hypothetical pores and experimental measurements of pore size distributions of a blended cement mortar, inductive arguments are made for considering the electric double layer as a potentially significant factor in determining the transient movement of ions within cementitious porewaters.

Chapter 4 departs from the diffusive process in order to demonstrate a novel method of characterizing and quantifying the extent of reaction of highly heterogeneous blended cement systems, supplemented with iron blast furnace slag and coal combustion residue, using probabilistic techniques applied to backscattered scanning electron microscopic and energy dispersive X-ray spectroscopic information. Extent of reaction is a key parameter for determining the chemical properties of systems containing supplementary cementitious materials, and the reliable quantification of the degree of reaction in supplementary cementitious materials has been identified as a major need within the field [13]. In Chapter 5, the extent of reaction is used to determine the masses of the "partial equilibrium assemblage", that is, the mass of major constituents within the reacted portion of a blended cement system. A set of solid phase equilibrium constants developed for describing Portland cement systems is used in conjunction with the reacted to mass to compute the pH-dependent solubility of the same blended cement system. Given that the reaction product of ashes and slags in cement systems are largely unknown, the comparison of these simulations to batch leaching experiments serve as a guide for assessing the limitations of current thermodynamic data for describing these complex systems.

Chapter 6 is the culmination of the results of the previous four chapters in that the transient leaching behavior of the blended cement is modeled and compared to experimentally measured values of major constituent release. In this study, cement monoliths are exposed to external aging solutions which are intended to elicit the mineralogical changes expected in natural

environments. The ability of the Portland cement solid phases to characterize the monolith leaching behavior is evaluated and the potential limitations of the current thermodynamic understanding of these systems are highlighted.

CHAPTER 2

2. IONIC TRANSPORT IN CEMENT-BASED MATERIALS

Abstract

The local electroneutral form of the Nernst-Planck (NP) equations, derived from the null-current assumption, is employed to model the transport of multiple ionic species in aqueous solution. Predictions of primary ion solubility profiles are compared to those of the more common Fickian diffusion model within the context of a practical problem, leaching of a hydrated Portland cement paste. Differences between Fickian and NP transport are highlighted for three distinct external solution leaching scenarios: deionized water, ammonium nitrate solution, and a diluted porewater from a cementitious low-activity nuclear waste form. Although small differences are observed in the case of deionized water leaching, differences of as much as a factor of four are observed in the concentration profiles of certain species in the ammonium nitrate and simulated waste form solution leaching cases. Thus, the choice of transport model may influence predictions of contaminant release and degradation rates.

2.1. Introduction

Understanding the fundamental mechanisms of ion transport is key to assessing the long-term performance of cementitious materials. Whether predicting the rate of decalcification, of ingress of chloride, or of release of radionuclides from a cementitious waste matrix, there exists an unequivocal need for describing solute transport. Traditionally, transport phenomena in porous cementitious media have been described using the Fickian diffusion model; however, more complex electro-diffusion models have been proposed recently with the goal of improving predictive capability. One of complexities of ionic transport in porous cements arises from the presence of numerous (≈ 50) ionic species in the pore solution. In this article, we investigate the differences in ionic concentrations predicted by two distinct transport models, namely Fickian diffusion and electro-diffusion, and address a fundamental question: what is the importance of

the Coulombic interactions between the numerous ions in the cement pore solution as well as those present in the external environment?

The first model to describe solute transport in the absence of advection be attributed to Adolf Fick who, in 1855 [14], first put forth the observation that a solute diffuses proportionally to its concentration gradient. Existing studies on leaching commonly employ the Fickian diffusion model to describe the transport of only a few ionic species thereby neglecting the physical constraint that the solution remain electroneutral. Another common practice is to employ single diffusion coefficient for all species in solution, which, when starting from an electroneutral initial condition, serves to maintain local electroneutrality [11, 15, 16]. Experimentally obtaining ion-specific Fickian diffusion coefficients may be both tedious and challenging because of their dependence upon the system state, as evidenced by the large number of empirical concentration-dependent diffusion coefficients found in the literature [17-21]. In contrast, the Nernst-Planck (NP) transport model provides a mechanism for maintaining electroneutrality (in the absence of applied potential), and may account for some concentration-dependent diffusive behavior given an appropriate chemical activity model. In 1888, Walther Nernst asserted that the transport of an ion is proportional to its electrochemical potential gradient. The NP model has been adopted and amended by a number of disciplines, most notably for describing ionic transport in proteins [22-25], in highly concentrated and ionic liquids [26-29], in nanofluidic channels [30-33], and in clays [34-39].

For modeling transport in cementitious materials, the application of the NP model has gained popularity in recent decades. Samson and co-workers [40, 41] employed the NP to the problem of describing ionic migration under an applied electric current for the interpretation of accelerated migration experiments, and a handful of studies have applied the NP to describe ionic migration in cementitious materials for various purposes [41-46]. Snyder and Marchand [47] carried out an experimental investigation of the case of zero external potential in nonreactive porous frit exposed to various initial and boundary conditions; their findings indicated that simple Fickian diffusion could not adequately describe multi-ionic diffusion and in some cases the fitted value of the Fickian diffusion coefficient became negative, that is, a species was transported against its concentration gradient. Samson and Marchand [48] also found close agreement between their NP results and experimental measurement of sulfate ingress fronts but

did not compare their results to the Fickian case. Galíndez and Molinero [49] compared Fickian and NP transport model results of sulfate attack of a cement paste using a limited number of ionic species and found that the NP model predicted the presence of near-surface gypsum front, whereas the Fickian model did not. These findings suggest that the Coulombic coupling of ions manifest in the NP model may be a significant factor in determining net transport rates. What has not been clearly established, however, is an explicit comparison of the Fickian and NP formulations in the absence of an applied external field within the context of a reactive transport simulation. Moreover, the long-term impacts of coupling of NP transport simulation with homogeneous reactions in the aqueous phase have not been fully addressed for cementitious systems [50]. Given that durability predictions depend upon transport predictions and that lifetime performance assessment in turn depends upon durability predictions, a salient question is whether the concentrations computed by the Fickian and NP models yield substantially different results.

The purpose of this article is to directly compare the Fickian and NP mass transport models within the context of a practical problem: aggressive leaching of a Portland cement. The three aggressive leaching solutions considered herein, pertinent to testing and field performance conditions, are deionized water, ammonium nitrate solution, and diluted porewater from a simulated low-activity waste form; each of these leachants represents a distinctly different class of solution: an infinitely dilute solution, a concentrated ($\approx$ 1M) single-salt solution, and a concentrated ($\approx$ 1M) multi-ionic solution, respectively. The investigation of these three solutions provides a basis for determining the conditions under which the differences between the Fickian and NP models may be important.

The remainder of this article is organized as follows. In Section 2, the geometry and conceptual model for simulation of the problem are outlined, and the governing equations and approximations of the reactive transport model are given for both the Fickian and NP transport model formulations. Due to its relative ease of implementation and computational efficiency, the finite difference (FD) method of numerical approximation has been employed in this work to simulate both Fickian and NP solute transport. In contrast to previous studies which employed an explicit form of the FD method for solving the NP system of equations [34, 35] the present work invokes the fully implicit FD method with Newton-Raphson iteration to account for the

nonlinear nature of the NP equations while allowing for arbitrarily large stable simulated time step intervals. Section 3 presents the aqueous and solid phase thermodynamic parameters necessary for calculating chemical equilibrium. The reactive transport of 81 aqueous species is considered in this work, which requires 81 ionic diffusion coefficients for the NP model. These diffusion coefficients remain unknown quantities for many of the aqueous species found to be relevant in geologic media and commonly used in Portland cement modeling. In [49], six values of ionic diffusion coefficient were provided for the approximately 30 aqueous species modeled, creating some ambiguity as to the values prescribed for each ion. In this work, however, an empirical relationship is proposed for correlating ionic diffusion coefficients for the ions in question to both their formal charge and van der Waals volumes, which is discussed in Section 3.3. Section 4 compares the Fickian and NP ionic transport models for four example cases, first within an inert porous medium and then within a reactive hydrated ordinary Portland cement (PC), considering the aforementioned external solutions in contact with the cementitious material. Section 5 recapitulates the major findings of each example case and summarizes the practical significance of these findings within the context of cementitious material leaching.

2.2. Models and methods

2.2.1. Simulation geometry

All simulations are performed at standard temperature and pressure for the one-dimensional case of a porous medium of length $\ell = 0.02$ [m], porosity $\phi = 0.20$ [m^3 connected porosity per m^3 total], and skeletal density of 2200 [kg/m^3]. The simulation domain consists of 21 nodes equally spaced at intervals of 1 mm. A single face of the medium, at $x = 0$ is exposed to an external solution of infinite volume such that the concentrations at the specimen-solution interface are fixed (Dirichlet boundary). Concentrations are also fixed at the opposite face, at $x = \ell$, to the initial porewater concentrations (Dirichlet boundary).

2.2.2. Reactive transport model formulation

In a saturated reactive porous medium, the mass conservation expression must reflect the dissolution and precipitation reactions, that is,

$$\frac{\partial C_i}{\partial t} = -\frac{\partial J_i}{\partial x} - F_i \tag{2.1}$$

where $C_i(x,t)$ [mol/m^3] refers to the concentration of i^{th} species in the pore solution at spatial location x [m] and time t [s], and J_i [mol/m^2/s] is the flux of species i. The reactive rate term F_i [mol/m^3/s] representing a phase change of i from the aqueous phase to a solid precipitate phase. Directly solving Eq. (2.1) is complex because the reactive term depends simultaneously on C_i which requires an iterative scheme that can be computationally expensive [50]. In this work, the sequential non-iterative algorithm (SNIA) has been employed [48, 51, 52], wherein the chemical equilibrium and transport equations are solved in a staggered approach. In the first step, the reaction terms are neglected in order to solve for concentration $\tilde{C}_i$ which is not necessarily in chemical equilibrium, as given by,

$$\frac{\partial \tilde{C}_i}{\partial t} = -\frac{\partial J_i}{\partial x} \tag{2.2}$$

Throughout this chapter, $\tilde{C}_i$ is referred to as the "uncorrected" concentration, because in the second step of SNIA, the corrected concentration C_i at the next time step is found from $\tilde{C}_i$ by solving for chemical equilibrium as described in Section 2.2.3.

Since Eq. (2.1) is derived from mass balance, it is generally valid with the flux J_i given by either the Fickian or NP transport model. As this chapter is concerned with the comparison of these two models, it is necessary to clarify the mathematical differences between them, which is described next.

Fickian diffusion model: For a nonreactive porous medium, the one-dimensional parabolic partial differential equation describing the conservation of mass within an infinitesimally small control volume may be written as [14, 53, 54]

$$J_i = -\tau D_i \frac{\partial \tilde{C}_i}{\partial x} \tag{2.3}$$

where τ (≤ 1) is the tortuosity factor [m/m], which in the one-dimensional case is a scalar quantity. The true physical significance of τ is not an entirely settled issue [55], but in this work, τ represents the physical resistance to diffusion resulting from increased diffusion path length

within a porous microstructure. The above Eq. (2.3) is generally valid for neutral (non-charged) species, but not for ionic (charged) species if the system is to remain electrically neutral. When considering the diffusion of only two oppositely charged species, that is $i = \{1,2\}$ and $\text{sign}(z_1) = -\text{sign}(z_2)$, the Coulombic coupling between charges requires that both species move at an equivalent rate [56]:

$$D_1 = D_2 = \frac{|z_1| + |z_2|}{|z_1|/D_1^u + |z_2|/D_2^u} \tag{2.4}$$

where z_i is charge and D_i^u is herein termed the ionic diffusion coefficient at infinite dilution [m^2/s]. Thus, Eq. (2.3) is valid for describing diffusion in a dilute binary system provided that the phenomenological diffusivity D_i is the same for both ions. If more than two ionic species are present in solution, D_i can no longer be defined independently of the system state because coupling of electrostatic forces occurs among all charged species, which necessitates the use of the NP model described next.

Nernst-Planck (NP) model: The electrostatic coupling between multiple (i.e. more than two) ionic species can be described by considering the electrochemical potential μ_i for each species separately as,

$$\mu_i = \mu_i^0 + \mathrm{R}T\ln\left(\gamma_i \tilde{C}_i\right) + z_i \mathrm{F}\psi \tag{2.5}$$

with μ_i^0 [J/mol] equal to the chemical potential at standard state, R [J/mol/K] the ideal gas constant, T [K] the absolute temperature, γ_i the activity coefficient, F [C/mol] Faraday's constant, and ψ [V] the electric potential within the medium. Nernst hypothesized that the flux, J_i, is proportional to the gradient in μ_i

$$J_i = -\tau D_i^u \left(\left(\frac{\partial \ln \gamma_i}{\partial \ln \tilde{C}_i} + 1 \right) \nabla \tilde{C}_i + \frac{z_i \tilde{C}_i \mathrm{F}}{\mathrm{R}T} \nabla \psi \right), \tag{2.6}$$

and by invoking the null current condition, that is, $I \equiv \sum_i z_i J_i = 0$, the gradient in potential can be eliminated as an unknown such that the local electroneutral (LEN) diffusion form of ionic flux can be written as [57-61],

$$J_i = -\tau D_i^u \left(\left(\frac{\partial \ln \gamma_i}{\partial \ln \tilde{C}_i} + 1 \right) \nabla \tilde{C}_i - \frac{z_i \tilde{C}_i}{\left(\sum_i z_i^2 D_i^u \tilde{C}_i \right)} \sum_j z_j D_j^u \left(\frac{\partial \ln \gamma_j}{\partial \ln \tilde{C}_j} + 1 \right) \nabla \tilde{C}_j \right). \quad (2.7)$$

Note that for neutral species, the second term of Eq. (2.7) becomes zero, and the flux only depends upon the activity gradient of that species.

By collecting like terms for the one-dimensional case, Eq. (2.7) can be written concisely as

$$J_i = \tau \sum_j \left(D_{ij} \left(\frac{\partial \ln \gamma_j}{\partial \ln \tilde{C}_j} + 1 \right) \frac{\partial \tilde{C}_j}{\partial x} \right) \quad (2.8)$$

where D_{ij} is defined as

$$D_{ij} \equiv \delta_{ij} D_i^u - \frac{z_i z_j D_i^u D_j^u \tilde{C}_i}{\sum_p z_p^2 D_p^u \tilde{C}_p}, \quad (2.9)$$

and δ_{ij} is the Kronecker delta function [62]:

$$\delta_{ij} = \begin{cases} 0, for\ i \neq j \\ 1, for\ i = j \end{cases}. \quad (2.10)$$

Eq. (2.7) clearly demonstrates that the ionic flux depends not only on the concentration gradient of species i but also on the concentration gradients of all other charged species in solution. Moreover, the LEN model requires two more parameters per ion than the Fickian model, namely the activity coefficient and ionic diffusion coefficient, which are described in Section 2.3.

2.2.3. Geochemical reaction

In this chapter, equilibrium speciation is determined using the thermodynamic equilibrium solver of LeachXS/ORCHESTRA [63], but the constitutive equations are briefly summarized for the sake of clarity.

The reactions involving the i^{th} species that lead to the precipitation of solid phases are described by the term F_i in Eq. (2.1); however, in the current formulation an explicit form for F_i is not specified. Instead, a set of equilibrium equations correct the transport equation for the reaction terms. As is customary in equilibrium chemistry, it is convenient to partition the set of all

possible aqueous and solid species into subsets of primary and secondary species (see, for example [64]). In this work, all primary species have been chosen as aqueous species denoted p. After the initial transport step according to Eq. (2.2), the mass conservation of primary species p is written as

$$\widetilde{M}_p = V_w\left(\tilde{C}_p + \sum_{i\neq p} \nu_{pi}\tilde{C}_i\right) + \sum_{\ell} \nu_{p\ell} n_\ell^k \tag{2.11}$$

where V_w [L] is the volume of water in the system, $\tilde{C}_p$ is the uncorrected concentration of p, ν_{pi} [-] is the stoichiometric coefficient of p in the i^{th} secondary aqueous species with uncorrected concentration $\tilde{C}_i$, $\nu_{p\ell}$ [-] is the stoichiometric coefficient of p in the ℓ^{th} secondary solid species, and n_ℓ^k [mol] is the number of moles of solid species ℓ at time step k. Chemical equilibrium is solved a time step $k+1$ by prescribing a mass conservation equation for each p of the form

$$V_w\left(C_p^{k+1} + \sum_{i\neq p} \nu_{pi} C_i^{k+1}\right) + \sum_{\ell} \nu_{p\ell} n_\ell^{k+1} = \widetilde{M}_p. \tag{2.12}$$

The equilibrium chemistry is further specified by the laws of mass action for each secondary aqueous species which take the form

$$C_i^{k+1} = \frac{1}{\gamma_i K_i}\left(\prod_p \left(\gamma_p C_p^{k+1}\right)^{\nu_{pi}}\right), \tag{2.13}$$

where K_i and γ_i are the stability constant and activity coefficient for the i^{th} species, respectively. For stable solid phases,

$$\frac{1}{X_\ell K_\ell}\left(\prod_l \left(\gamma_p C_p^{k+1}\right)^{\nu_{p\ell}}\right) = 1 \tag{2.14}$$

where K_ℓ is the stability constant for the ℓ^{th} species. X_ℓ denotes the activity of the ℓ^{th} solid phase and is equal to unity for pure phases and taken as the mass fraction of the end-member for the ideal solid solutions considered herein.

2.2.4. Solution strategy

The strategy for solving the reactive transport equations that is adopted here is given by:

Step 1: At time $t = 0$, initialize M_p^0 at each node and solve for equilibrium C_i^0 and n_ℓ^0.

Step 2: At time step k+1,

(a) Compute uncorrected concentrations $\tilde{C}_i^{k+1}$ from Eq. (2.2) using the previous time step's corrected solution C_i^k.

(b) Update the masses $\widetilde{M}_p^{k+1}$ as defined in Eq. (2.14) and compute corrected concentrations C_i^{k+1} and n_ℓ^{k+1} by solving Eqs. (2.15) – (2.17).

Step 3: If $t^{k+1} < t_{\text{final}}$, set $k = k + 1$ and go to Step 2, else break.

2.2.5. Numerical method

Whereas a fully explicit finite difference (FD) scheme has elsewhere been employed for solving the LEN equations (for example [34-36]), very small timesteps are typically required to maintain stability and accuracy in explicit approximations of nonlinear equations. On the contrary, the fully implicit FD scheme employed herein allows for iterative improvement of the numerical solution and is, therefore, briefly described. All transport calculations have been implemented using the scientific computing code MATLAB (MATLAB 8.1.0.604, The MathWorks Inc., Natick, MA, 2013).

Numerical approximation of the reactive transport Eq. (2.1) is commonly employed due to the ease of incorporating arbitrary initial and boundary conditions for which analytical solutions are generally not available. The finite difference (FD) method is a ubiquitous numerical technique for solving a variety of problems including the parabolic PDEs given in Eqs. (2.3) and (2.7). In this work, the fully implicit forward-in-time, centered-in-space FD stencil has been adopted, due to both its unconditional stability with respect to the length of the time step, Δt, and its dissipation of numerical error with time when applied to the Fickian model [65]. The formula of the implicit scheme applied to Eq. (2.3) consists of a first order approximation of the time derivative and a second order approximation of the spatial derivative given by [53]

$$ {}^{m}\tilde{C}_i^{k+1} = {}^{m}C_i^{k} + \frac{\Delta t}{h} D_i \left(\tau_{+1/2} \left(\frac{\Delta_+ \left(\tilde{C}_i^{k+1} \right)}{\Delta_+ (x)} \right) - \tau_{-1/2} \left(\frac{\Delta_- \left(\tilde{C}_i^{k+1} \right)}{\Delta_- (x)} \right) \right) \tag{2.15} $$

where m and k are the indices corresponding to spatial and temporal discretization and the symbols Δ_+ and Δ_- indicate the forward and backward difference operators, respectively, from node m, such that

$$ \begin{aligned} \Delta_+ \left(\tilde{C}_i^{k+1} \right) &= {}^{m+1}\tilde{C}_i^{k+1} - {}^{m}\tilde{C}_i^{k+1} \\ \Delta_- \left(\tilde{C}_i^{k+1} \right) &= {}^{m}\tilde{C}_i^{k+1} - {}^{m-1}\tilde{C}_i^{k+1} \end{aligned} \tag{2.16} $$

Similarly, the differences of the spatial variables are given by

$$ \begin{aligned} \Delta_+ (x) &= {}^{m+1}x - {}^{m}x \\ \Delta_- (x) &= {}^{m}x - {}^{m-1}x \\ h &= ({}^{m+1}x - {}^{m-1}x)/2 \end{aligned} \tag{2.17} $$

which allows for non-uniform spatial grids. Tortuosity is evaluated at the midpoints between nodes, that is,

$$ \begin{aligned} \tau_{+1/2} &= ({}^{m+1}\tau + {}^{m}\tau\,)/2 \\ \tau_{-1/2} &= ({}^{m}\tau + {}^{m-1}\tau\,)/2, \end{aligned} \tag{2.18} $$

which accounts for possible variation of τ with x. For this work, the Fickian diffusion coefficient D_i is treated as a constant in both space and time.

The approximation of the Fickian model given in Eq. (2.18) may be written in matrix notation for a single species i as

$$ \mathbf{A}\mathbf{c}^{k+1} = \mathbf{c}^{k} \tag{2.19} $$

where $\mathbf{c}^{k+1}$ denotes the vector of unknown $\tilde{C}_i^{k+1}$ values at and $\mathbf{c}^{k}$. For a system of $N_\mathrm{N} + 1$ spatial nodes, with 0 and N_N denoting the left and right boundary nodes, respectively, the coefficient matrix **A** given as,

$$\mathbf{A} = \begin{bmatrix} q_0 & r_0 & 0 & 0 & 0 \\ s_1 & q_1 & r_1 & 0 & 0 \\ 0 & \ddots & \ddots & \ddots & 0 \\ 0 & 0 & s_{N-1} & q_{N-1} & r_{N-1} \\ 0 & 0 & 0 & s_N & q_N \end{bmatrix} \tag{2.20}$$

where

$$\begin{aligned} r_m &= -\left(\tau_{+1/2}\right) D_i \frac{\Delta t}{h \Delta_+(x)} \\ s_m &= -\left(\tau_{-1/2}\right) D_i \frac{\Delta t}{h \Delta_-(x)} \\ q_m &= 1 - (r_m + s_m). \end{aligned} \tag{2.21}$$

For the Dirichlet boundary conditions at $x = 0$, the coefficients q_0 and r_0 are 1 and 0, respectively, and similarly at $x = \ell$, q_N and s_N are 1 and 0, respectively. Thus, when D_i and τ are constant in time, the FD approximation of the Fickian model is a linear system.

Due to the Coulombic coupling and activity terms in Eq. (2.7), numerical approximation of the NP model is somewhat more complicated than the Fickian. The FD approximation of Eq. (2.7) can be written as,

$${}^m\tilde{C}_i^{k+1} = {}^m\tilde{C}_i^{k+1} + \frac{\Delta t}{h} \sum_j \left(\left(\tau \xi_j D_{ij}\right)_{+1/2}^{k+1} \left(\frac{\Delta_+\left(\tilde{C}_j^{k+1}\right)}{\Delta_+(x)} \right) - \left(\tau \xi_j D_{ij}\right)_{-1/2}^{k+1} \left(\frac{\Delta_-\left(\tilde{C}_j^{k+1}\right)}{\Delta_-(x)} \right) \right) \tag{2.22}$$

where $\xi_j \equiv \left((\partial \ln \gamma_j)/(\partial \ln C_j) + 1\right)$. The above equation differs from Eq. (2.18) in two fundamental ways. First, the flux is determined from the sum of contributions from the concentration gradients of all species; for a set of N_i species, these Coulombic coupling terms cause the system of equations to take the form of ${N_i}^2$ tridiagonal blocks as given by,

$$\mathbf{K}\boldsymbol{\varsigma}^{k+1} = \begin{bmatrix} \mathbf{A}_{11} & \cdots & \mathbf{A}_{1N_i} \\ \vdots & \ddots & \vdots \\ \mathbf{A}_{N_i 1} & \cdots & \mathbf{A}_{N_i N_i} \end{bmatrix} \begin{Bmatrix} \mathbf{c}_1^{k+1} \\ \vdots \\ \mathbf{c}_{N_i}^{k+1} \end{Bmatrix} = \boldsymbol{\varsigma}^k, \tag{2.23}$$

where $\boldsymbol{\varsigma}$ is the full set of $\mathbf{c}$ vectors for each species and $\mathbf{A}_{ij}$ denotes a tridiagonal matrix block of the form of Eq. (2.20). Second, the coefficient matrix $\mathbf{K}$ depends upon the concentrations at the $k+1$ time step and is, consequently, nonlinear in time. Whereas a fully explicit scheme has elsewhere been employed to model ionic transport in clays using the LEN form of the NP equations [34-36], very small timesteps are typically required to maintain stability and accuracy in explicit approximations of nonlinear equations. The fully implicit FD scheme, however, allows for iterative improvement of the numerical solution and is, therefore, employed herein for solving Eq. (2.26). Newton-Raphson iteration is implemented by defining the residual vector as

$$\mathbf{r} = \mathbf{K}\boldsymbol{\varsigma}^{k+1} - \boldsymbol{\varsigma}^{k} = 0 \tag{2.24}$$

Note that because $\mathbf{K}$ is a linear operator on $\boldsymbol{\varsigma}^{k+1}$, it is also the Jacobian matrix $\partial\mathbf{r}/\partial\boldsymbol{\varsigma}^{k+1}$ of the system [66]. The solution $\boldsymbol{\varsigma}^{k+1,s+1}$ is found by iteratively solving for the incremental solution at iteration $s+1$ via

$$\Delta\boldsymbol{\varsigma} = \mathbf{K}^{-1}\mathbf{r} \tag{2.25}$$

and $\boldsymbol{\varsigma}^{k+1,s+1} = \boldsymbol{\varsigma}^{k+1,s} + \Delta\boldsymbol{\varsigma}$, with calculation of the nonlinear coefficients ${}^{s}\xi_j^{k+1}$ and ${}^{s}D_{ij}^{k+1}$ also required at each iteration.

2.3. Model parameterization

2.3.1. Initial and boundary conditions

The material of interest is a hypothetical hydrated ordinary Portland cement (PC) with an assumed 85% degree of reaction of each cement component, which is considered a first-order approximation to a cement in which the C_3S has been consumed. The set of primary species used to impose mass balance in the thermodynamic equilibrium equations are chosen as the predominant aqueous forms of the major elements present in cements. Input masses M_p of the primary species are given in Table 2.1. The aliases presented in Table 2.1, without superscripts, are shorthand references to the primary species, p, and the dissolved concentration of a primary species refers to the quantity $C_p + \sum_{i \neq p} \nu_{pi} C_i$, that is, the portion of primary species present in the aqueous phase.

Table 2.1: Masses of primary species M_p^0 used as input to ORCHESTRA, expressed in units of moles per liter of pore solution, for an 85% hydrated Portland cement paste.

Primary Species	Alias	Concentration
OH^-	pH	
CO_3^{-2}	CO_3	$2.115(10^{-1})$
NH_4^+	NH_4	0
NO_3^-	NO_3	0
Na^+	Na	$4.287(10^{-2})$
Mg^{+2}	Mg	$1.601(10^{-1})$
$Al[OH]_4^-$	Al	$6.086(10^{-1})$
SO_4^{-2}	S	$2.429(10^{-1})$
Cl^-	Cl	$4.495(10^{-3})$
K^+	K	$7.222(10^{-2})$
Ca^{+2}	Ca	7.293
$Fe[OH]_4^-$	Fe	$3.445(10^{-1})$

Three reactive transport scenarios are herein considered (Table 2.2). In the first scenario, the external solution is deionized water (DI), in the second, a 1.5 M ammonium nitrate solution (AN), and in the third, a 3× diluted waste form simulant porewater (WF) as measured by porewater expression under triaxial compression [67]. These three simulated solutions have been chosen to serve as representative cases of three general classes of leaching problems that are determined by the composition of the external solution: very dilute solution (DI), concentrated solution of a single electrolyte (AN), and concentrated multi-ionic solution (WF). Each leaching scenario has practical significance as well; DI water leaching is prescribed in Method 1315 for assessing the release of constituents of potential concern [68], AN is commonly used as an accelerated degradation agent for the study of cement and concrete durability [69], and WF may provide an indication of the interactions between cement waste forms and concrete superstructures.

Table 2.2: Masses M_p^0 [mol per L solution] of the primary species of the three external solutions considered: deionized water (DI), ammonium nitrate (AN), and 3× diluted waste form porewater (WF). Masses are expressed in units of moles per liter of solution. Also shown are the calculated equilibrium pH and ionic strength values of each solution.

Primary Species	DI	AN	WF
OH	0		
CO_3	0	0	$3.849(10^{-02})$
NH_4	0	1.500	0
NO_3	0	1.500	1.192
Na	0	0	1.473
Mg	0	0	0
Al^-	0	0	0
Si	0	0	0
S	0	0	$2.000(10^{-02})$
Cl^-	0	0	$2.963(10^{-03})$
K	0	0	$3.978(10^{-02})$
Ca	0	0	$2.833(10^{-04})$
Fe^-	0	0	0
pH	7.00	4.62	12.48
Ionic Strength	0	1.083	1.140

2.3.2. Thermodynamic constants

Laws of mass action stability constants were computed from Gibbs free energies obtained primarily from Lothenbach et al. [70] and the Nagra/PSI thermodynamic database [71] when possible; however, additional values have also been obtained from Lothenbach and Winnefeld [72], Faure [73], and Shock et al. [74]. The free energies of all aqueous species considered are provided in Appendix A and notably include several cation-silicon complexes which have been found to persist in geologic media [75].

The solid species included in the thermodynamic model, given in Appendix B, reflect, primarily, those used for modeling the hydration of Portland cement, including two solid solution models of calcium silicate hydrate (C-S-H) [72] which attempt to capture the incongruent

precipitation/dissolution behavior of the primary hydration phase of Portland cements. Monosulfate (AFm), monocarbonate (AFm_c), hemicarbonate (AFm_{hc}), and ettringite (AFt) ideal solid solutions between Al- and Fe-bearing end-members have also been included. A number of phases that are unlikely to form in ordinary Portland cement, for instance halite and nitratine ($NaNO_3$ (cr)), have also been included in anticipation of their possible stability as a result of exposure to the various external solutions. Neither sorption nor exchange reactions have been included in the simulation, which renders Na, K, and Cl completely soluble in the native PC pore solution. Listed in Table 2.3 are the calculated equilibrium concentrations of primary species in the PC pore solution, using the input masses in Table 2.1 and the thermodynamic constants in Appendices A and B.

Table 2.3: Calculated equilibrium concentrations [mol/L] of primary species in the native PC pore solution.

Primary Species	PC pore solution
OH	
CO_3	$1.004(10^{-04})$
NH_4	0
NO_3	0
Na	$4.116(10^{-01})$
Mg	$8.001(10^{-11})$
Al	$1.080(10^{-03})$
Si	$9.505(10^{-03})$
S	$1.516(10^{-02})$
Cl^-	$4.315(10^{-02})$
K	$6.933(10^{-01})$
Ca	$2.926(10^{-04})$
Fe^-	$1.115(10^{-05})$
pH	13.89
Ionic Strength	0.910

To elucidate the effects of speciation on transport behavior, the pH-dependent solubility behavior was first simulated in the absence of ionic transport. The simulation mimicked the USEPA Method 1313 leaching protocol [76], wherein 40 grams of dry, granular hydrated Portland cement are added to 400 grams of deionized water and an aliquot of either NaOH or HNO_3 in order to raise or lower, respectively, the pH of the aqueous solution. The simulated pH-dependent release curves for the major primary entities of PC are presented in Fig. 2.1, and, in general, the solubility of primary species, excepting Na, K, and Cl, is predicted to be highly sensitive to pH in the relevant range of pH 9 to 14, with the increase in Na solubility in the high pH range due to the aliquot of NaOH added during Method 1313 to adjust pH. Thus, it is expected that small differences in pH evolution predicted by the Fickian and LEN transport models could lead to significantly different ionic fluxes in the reactive transport model. Further, the solubilities of Mg and Ca increase monotonically with decreasing pH, whereas the solubilities of Al, Si, and S reach a minimum solubility at pH of about 12.5. Also of significance is that the predominant anion above pH 12 is hydroxide.

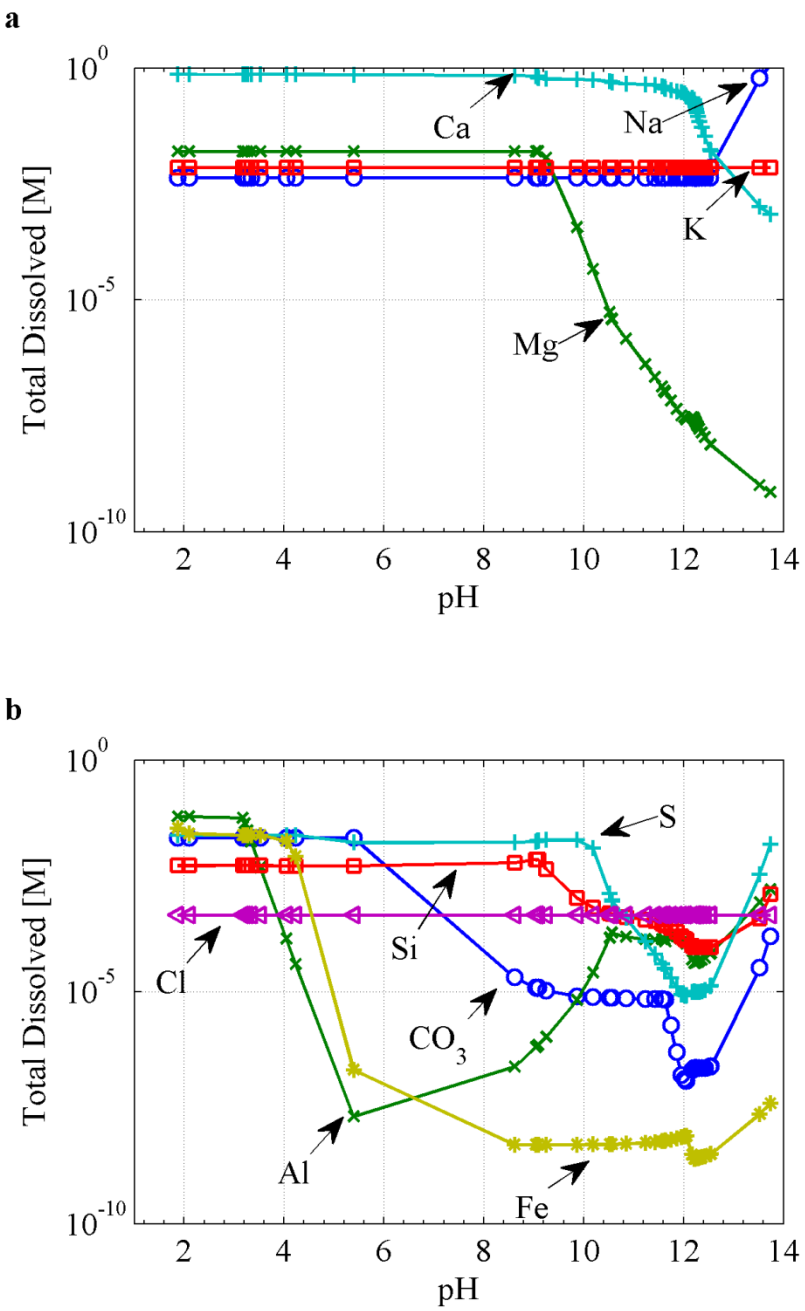

Figure 2.1: Modeled pH dependent solubility of primary species in a) typically cationic and b) typically anionic form in hydrated Portland cements. Note that the predominant anion above pH 12 is OH^- (not shown).

2.3.3. Activity coefficients

In this work, the modified Davies equation developed for cementitious materials [77] has been adopted for describing the activities of aqueous species. This model is advantageous in the fact that it does not require parameters for individual species but instead has been optimized for describing the ions in cement pore solutions up to and ionic strength of 1.5 M.

In the modified Davies model, the activity coefficients γ_i may be expressed as

$$\ln\gamma_i = -\frac{Az_i^2\sqrt{I}}{1+\beta B\sqrt{I}} + \frac{(\alpha I + 0.2)Az_i^2 I}{\sqrt{1000}}, \tag{2.26}$$

where $I = \frac{1}{2}\sum_i C_i z_i^2$ is the ionic strength, A and B are physical parameters given by

$$A = \frac{\sqrt{2}F^2 e}{8\pi(\epsilon_r \mathrm{R}T)^{3/2}}, B = \sqrt{\frac{2F^2}{\epsilon_r RT}}, \tag{2.27}$$

ϵ_r [C/V/m] is the relative permittivity of the solution, and e [C/particle] is the elementary particle charge. The coefficients α and β are fitting parameters which have been optimized in [77] for describing the activities of major cement primary species with values $\alpha = -4.17 \times 10^{-5}$ and $\beta = 3 \times 10^{-10}$, respectively.

A commonly employed form of the NP equation (Eq. 2.6) expands the partial derivative of logarithms as

$$\left(\frac{\partial \ln\gamma_i}{\partial \ln C_i}\right)\nabla C_i = C_i \nabla(\partial \ln \gamma_i). \tag{2.28}$$

However, in this work it is proposed to evaluate $(\partial \ln\gamma_i)/(\partial \ln C_i)$ analytically which eliminates the need to approximate $\nabla(\partial \ln \gamma_i)$ and the concomitant error associated with the approximation. Using Eq. (2.26), the partial derivative of logarithms in Eq. (2.8) may then be written explicitly as

$$\frac{\partial \ln\gamma_i}{\partial \ln\tilde{C}_i} = -\frac{A\left|z_i^3\right|\sqrt{2\tilde{C}_i}}{4\left(\beta B\frac{|z_i|}{\sqrt{2}}\sqrt{\tilde{C}_i}+1\right)^2} + \frac{Az_i^4\tilde{C}_i\left(\alpha z_i^2\tilde{C}_i + 0.2\right)}{2\sqrt{1000}}. \tag{2.29}$$

Thus, $\partial \ln \gamma_i / \partial \ln \tilde{C}_i$ is evaluated analytically, and, for neutral species, it is easy to verify that $\partial \ln \gamma_i / \partial \ln \tilde{C}_i$ is always zero and γ_i is always one, that is, the activity is equivalent to the molar concentration.

2.3.4. Ionic diffusion coefficient estimation

A significant hindrance to isolating the influence of the charge-coupling mechanism in the LEN model (Eq. 2.7) is that for many of the aqueous species present in alkaline geologic media (Appendix A) the ionic diffusion coefficient D_i^u has not been experimentally determined. Therefore, in the present study, the values of unknown D_i^u have been estimated empirically as a function of both the size and charge of the unhydrated ion. Such a functional relationship is similar to the relationship proposed by Oelkers and Helgeson [78] who correlated D_i^u to both the formal charge and the effective electrostatic radius of aqueous charged species. In their model, the diffusivity is directly proportional to the formal charge and inversely proportional to the effective electrostatic radius, as predicted by the Stokes-Einstein relation. Such a simplistic model belies the true complexity of ion transport; as suggested by [79] the ionic diffusivity fundamentally depends on the tendency of the ion to break the hydrogen bonds of the loosely structured water molecules in the vicinity of the hydrated of the ion [80]. Koneshan et al. [81] recently investigated the structure making and breaking tendencies within a molecular dynamics simulation of several monoatomic ions, but, to the authors' knowledge, such a study of many of the aqueous species studied herein, given in Appendix A, has not been undertaken. Extension of these simulations to the ions found in cementitious media may prove to be eminently useful, especially within the context of determining radionuclide mobilities, but at present, simple empirical relations serve to generate feasible, albeit inaccurate, values of D_i^u.

Table 2.4: Ionic species used for estimation of unknown ionic diffusion coefficients. Estimated van der Waals volumes V_i [Å^3] and published diffusion coefficients D_i^u [10^{-9} m^2/s] given in [82].

Species	V_i	D_i^u	Species	V_i	D_i^u	Species	V_i	D_i^u
Al^{+3}	33.51	1.623	HSO_4^-	61.95	1.385	OH^-	19.54	5.273
Ba^{+2}	33.51	1.694	I^-	32.52	2.045	$H_2PO_4^-$	61.80	0.959
Ca^{+2}	33.51	1.584	IO_3^-	65.67	1.078	HPO_4^{-2}	59.39	1.518
Cl^-	22.45	2.032	K^+	87.11	1.957	PO_4^{-3}	56.99	2.472
CO_3^{-2}	42.84	1.856	Li^+	25.25	1.029	Rb^+	33.51	2.072
Cs^+	33.51	2.056	Mg^{+2}	21.69	1.412	$S_2O_3^{-2}$	74.34	2.264
Fe^{+2}	33.51	1.438	Mn^{+2}	33.51	1.424	SeO_4^{-2}	69.54	2.016
Fe^{+3}	33.51	1.812	Na^+	49.00	1.334	SO_3^{-2}	55.88	1.898
H^+	0.00	9.310	NH_4^+	25.28	1.957	SO_4^{-2}	64.34	2.130
HCO_3^-	42.84	1.185	NO_2^-	34.16	1.912	Sr^{+2}	33.51	1.582
HS^-	27.04	1.731	NO_3^-	41.94	1.902	UO_2^{+2}	48.37	0.852

Whereas Oelkers and Helgeson [78] related D_i^u to the effective electrostatic radius, it was found in this work that D_i^u is more strongly correlated to the approximate van der Waals volume V_i [Å^3] which was calculated using the Calculator Plugins module of the chemical structure visualization tool Marvin 6.1.3, 2013, ChemAxon (http://www.chemaxon.com). Calculated van der Waals volumes and D_i^u values for ions experimentally-reported D_i^u values are provided in Table 2.4 Cations and anions are treated as separate populations because the diffusivity of anions appears to be far more sensitive to the ratio of charge to van der Waals volume, z_i/V_i, as demonstrated in Fig. 2.2. The form of D_i^u expressed as a function of z_i/V_i for both cations and anions was found using linear least squares regression. For anions, this relationship takes the form

$$D_i^u = 10^{-9} \times (-29.9 \times z_i/V_i + 0.885), \quad (1)$$

and for cations

$$D_i^u = 10^{-9} \times (-1.92 \times z_i/V_i + 1.689). \quad (2)$$

Given the paucity of data on the mobility of neutral species, the diffusivity ascribed to these species was chosen to be a linear function of the estimated van der Waals volume of that ion, that is

$$D_i^u = 10^{-9} \times (2.50 - 8.33^{-3} \times V_i). \quad (3)$$

All estimated values of D_i^u for unmeasured ions are listed in Appendix C.

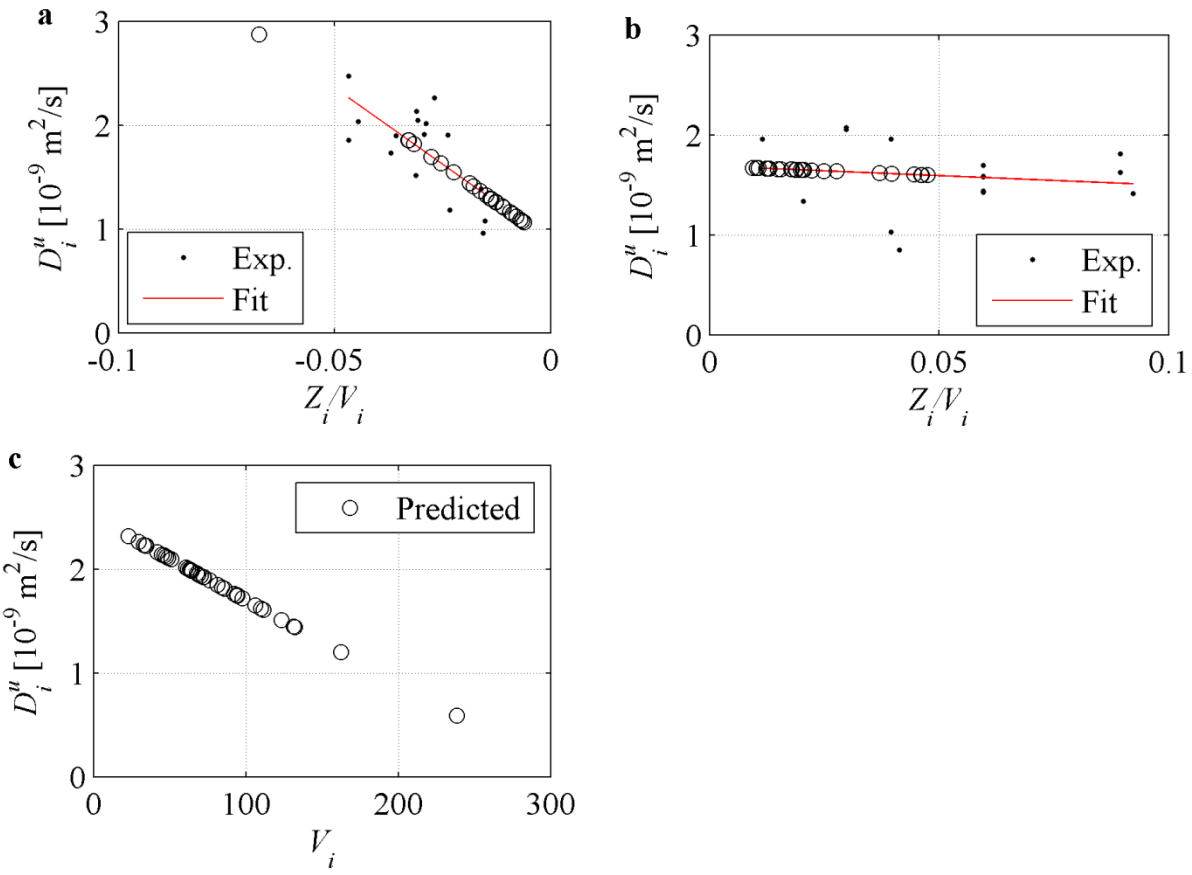

Figure 2.2: a) Fitted linear regressions of D_i^u values as a function of the ratio of ion charge Z_i to the estimated van der Waals volume V_i for anionic species. Black dots indicate the published D_i^u values [82] with which the red regression line was fitted. Open circles indicate the predicted values of D_i^u for the unmeasured species used in this study. b) Regression of D_i^u values for cations. (c) Values of D_i^u for neutral species, which are assumed herein to be linearly dependent on the van der Waals volume V_i, as implied by the Stokes-Einstein relation.

2.4. Results and discussion

2.4.1. Example 1: Comparison of Fickian and LEN transport in an inert porous medium

The pertinent question for long-term performance assessment is whether the transient concentration profiles computed from the two equations are substantially different. Previously, Snyder and Marchand [47] found that a simple Fickian model was inadequate to describe the migration of ions in a nonreactive porous frit subjected to various boundary conditions; however, the counterdiffusion of ions from the boundary into the medium in their experiments is atypical of most leaching test specifications wherein deionized water (DI) is used as leachant. Therefore, to address the magnitude of differences between Fickian and LEN transport, a model problem without chemical reaction is devised as follows. At $t = 0$ the region from $0 \leq x \leq \ell = 0.02$ m contains an aqueous solution of 50 M each of completely dissociated Na^+, Cl^-, K^+, OH^-, Ca^{+2}, and SO_4^{-2} ions in the pores, and the concentration at $x = 0$ is zero for $t > 0$. The fictitious tortuosity factor of the medium is assumed to be 50. In the LEN case, the values of D_i for Na^+, Cl^-, K^+, OH^-, Ca^{+2}, and SO_4^{-2} were taken from published values [82] whereas in the Fickian case the D_i was set to a uniform value for all species corresponding to the unweighted mean of the six individual diffusion coefficients, 2.649×10^{-9} m^2/s. The rationale for choosing such a problem is that, initially, the concentration gradients of all species are equal, and, therefore, any differences in release are entirely due to variation of D_i^u across species and to the Coulombic coupling and activity terms of Eq. (2.7).

The concentration depth profiles and the time-dependent fluxes out of the material (at $x = 0$) after 14 days of simulation are illustrated in Figs. 2.3a and 2.3b, respectively. The shape of the concentration curves in Fig. 2.3a varies greatly from species to species which implies that regression of effective diffusivities for each ion using the Fickian model will depend upon experimental conditions. It is apparent from Fig. 2.3b that in the NP model the flux of OH^- is approximately four times that of SO_4^{-2} initially, which portends a possibly significant effect on constituent release from the highly alkaline and largely pH-dependent PC system. Moreover, magnitudes of primary species fluxes are ordered as $OH^- > K^+ > Cl^- > Ca^{+2} > Na^+ > SO_4^{-2}$ whereas D_i are ordered as $OH^- > SO_4^{-2} > Cl^- > K^+ > Ca^{+2} > Na^+$ such that measuring D_i for a single species and extrapolating to the others based on their D_i^u values would be inconsistent with the NP model prediction. In both the concentration profiles (Fig. 2.3a) and time-dependent

fluxes (Fig. 2.3b), the mean value of D_i appears to be near-optimal in that the Fickian response lies near the average LEN response for all ions. Nonetheless, the conclusion of this exercise is that even in relatively simple systems, the LEN model may predict behaviors that are distinctly "non-Fickian".

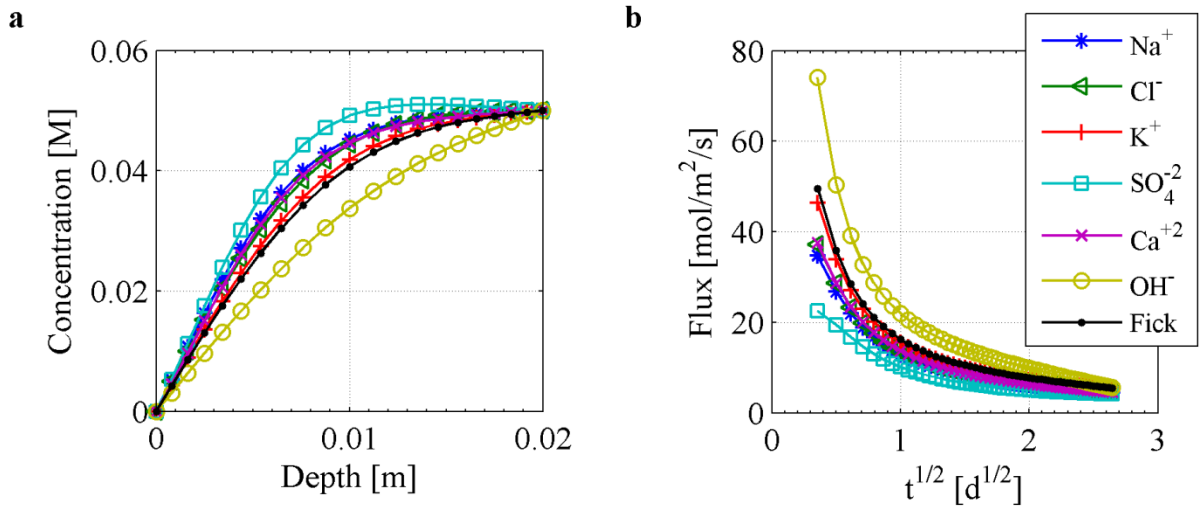

Figure 2.3: a) Comparisons of concentration depth profiles at 7 days of simulation time. Shown are ion concentrations predicted by the LEN model: Na^+ as blue asterisks, Cl^- as green triangles, K^+ as red "+", SO_4^{-2} as cyan squares, Ca^{+2} as purple "x", and OH^- as gold circles. The Fickian model predicts identical releases of all ions, only one of which is shown with black bullets and denoted "Fick". b) Estimated primary species fluxes out of the porous material (at $x = 0$) as a function of root time.

Given the highly reactive nature of cementitious materials, these results are insufficient *per se* to conclude that Coulombic coupling is an important factor for accurately modeling transport in cementitious materials. Therefore, to assess the differences in the Fickian and LEN in *reactive* transport modeling, the leaching of hydrated ordinary Portland cement has been investigated using the three distinct external leaching solutions defined in Table 2.2: DI, AN, and WF. In the Fickian transport case, the primary species diffuse at a single "mean" rate of 2.385×10^{-9} m^2/s, whereas in the LEN transport case, each aqueous species is transported with D_i^u given in Table 2.4 and Appendix C. In the following sections, the results of these comparisons are presented by evaluating the concentration-depth profiles of primary species, as the local concentrations of aqueous species reflect local physico-chemical phenomena that may lead to differences in, for instance, microstructural damage predictions.

2.4.2. Example 2: Dilute external leachant

Deionized water is often used to assess the leachability of constituents within solid matrices and is prescribed in standard leaching protocols. The Fickian and LEN model predictions of primary species concentration profiles for monolith leaching with DI are presented in Figs 2.4-2.7. In Fig. 2.4, it is apparent that the differences between models predicted for major species profiles are minute. After 10 months of simulated leaching, the concentration profile of total dissolved Ca exhibits a difference on the order of one percent at a depth of 1 mm, whereas pH, Al, and Si predictions differ between the two models by less than one percent.

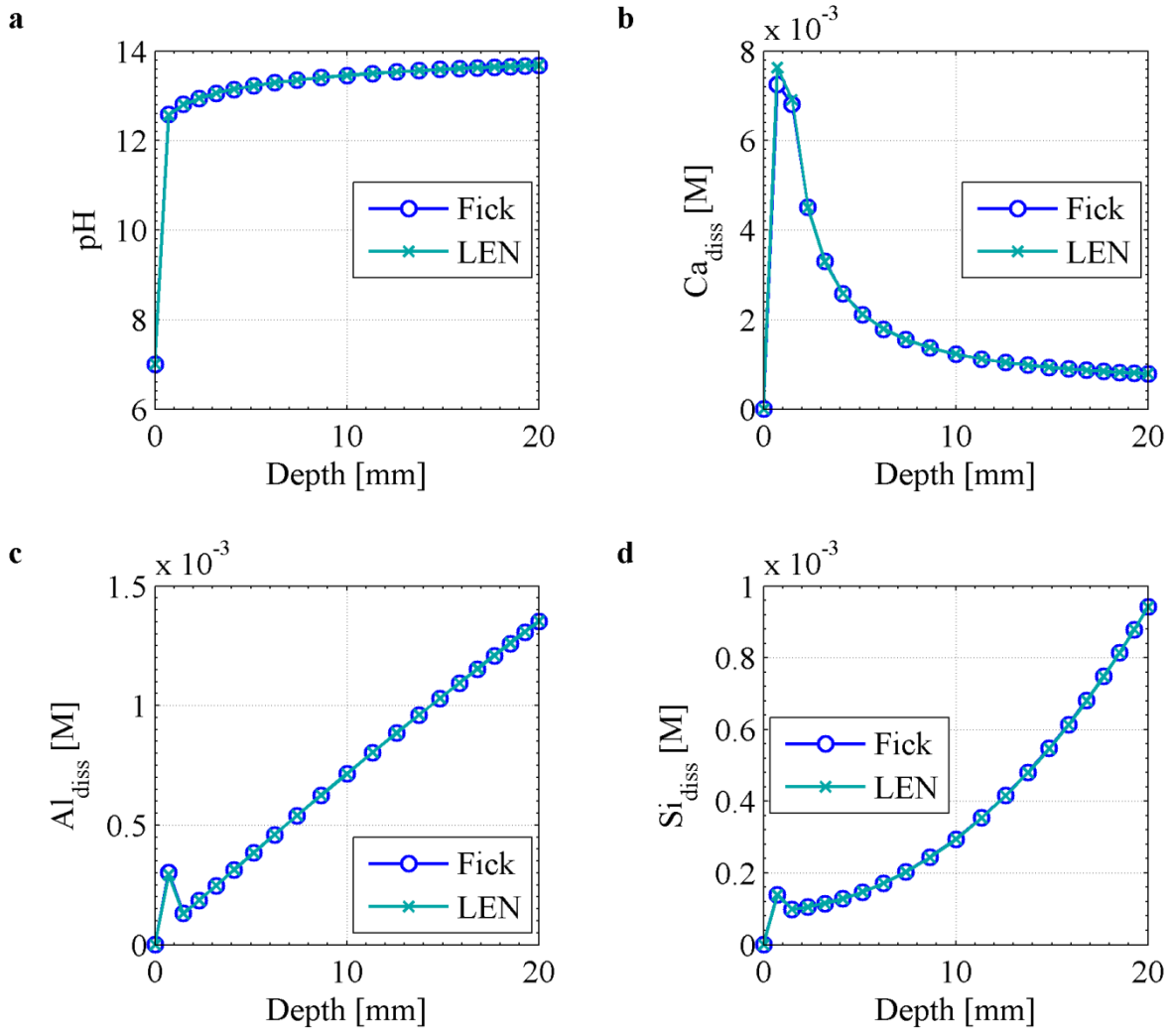

Figure 2.4: Comparison of a) pH, b) Ca, c) Al, and d) Si aqueous concentration profiles predicted by the Fickian and LEN transport models for the case of DI water leaching of PC after 280 days of simulated leaching.

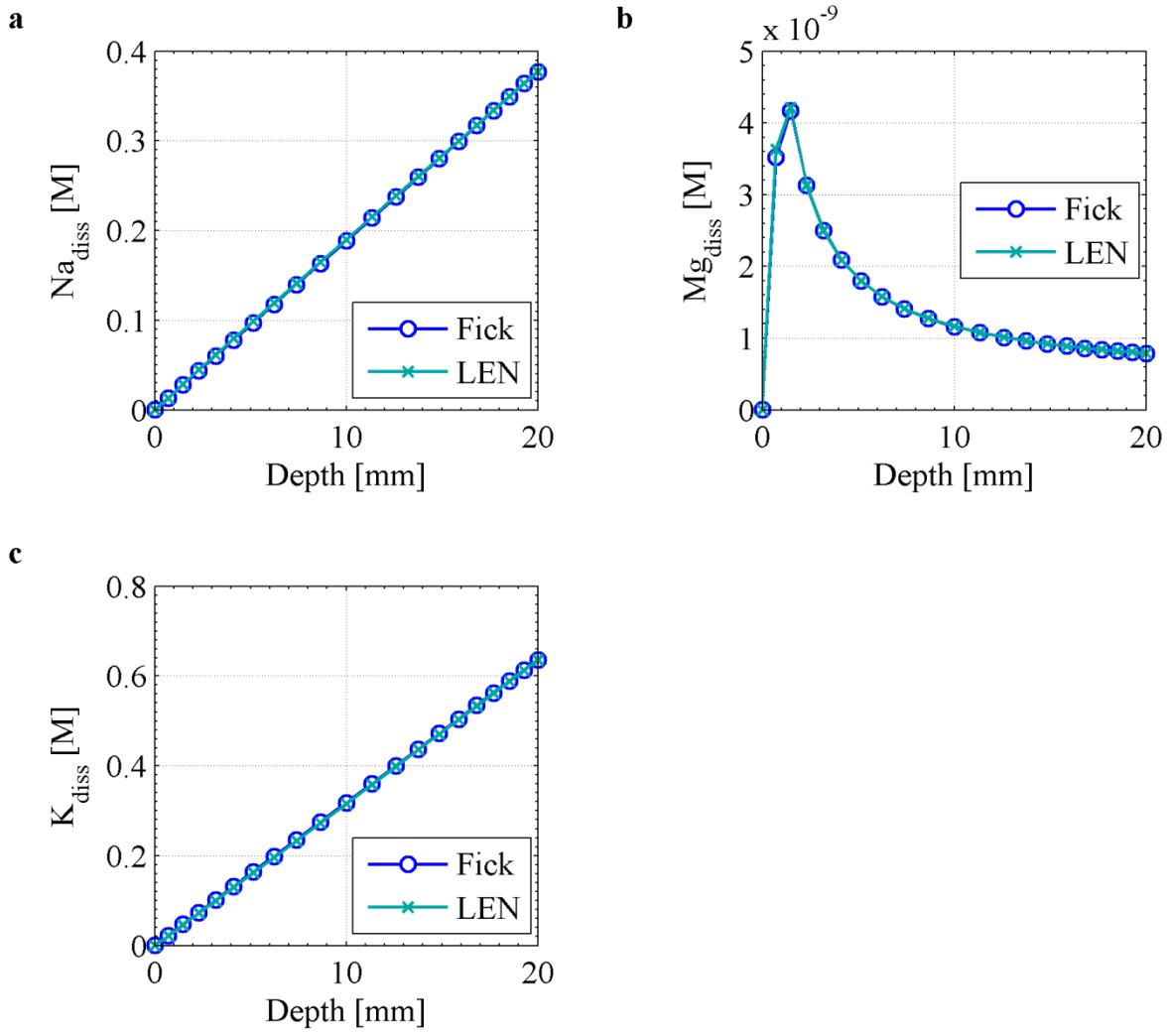

Figure 2.5: Comparison of typically cationic primary species profiles predicted by the Fick and LEN transport models for the case of DI water leaching of PC.

The concentration profiles of Na and K in Figs. 2.5a and 2.5b demonstrate that, in both the Fickian and LEN models, the transport of these primary species has reached steady state. Similar to Ca, the concentration profile of total dissolved Mg, in Fig. 2.5c varies slightly at a depth of 1mm. Otherwise, the variation between model predictions is quite small. The same is true for the primarily anionic primary species plotted in Fig. 2.6. Notably, the transport of Cl (Fig. 2.6c) has also reached steady state, as no Cl-bearing solid phases have formed.

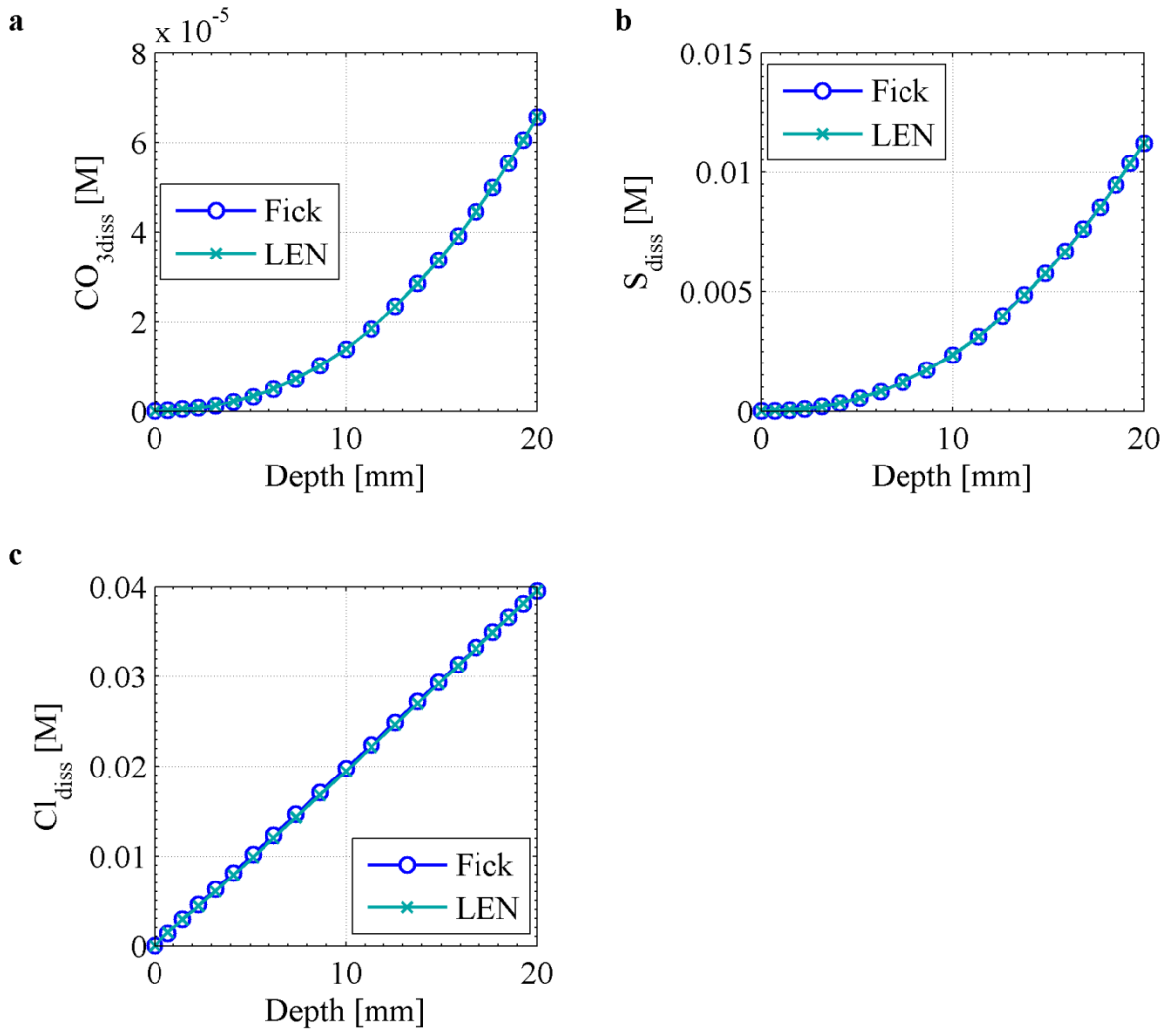

Figure 2.6: Comparison of typically anionic primary species profiles predicted by the Fick and LEN transport models for the case of DI water leaching of PC.

Illustrated in Fig. 2.7 are the predicted masses of hydrate phases per liter of control volume (L_{tot}), after 280 days of simulation, and, as expected based on the dissolved primary species profiles, only slight differences near the boundary are observed between the two models. The close agreement between models implies that any predicted physical and mechanical properties would likely be similar as well.

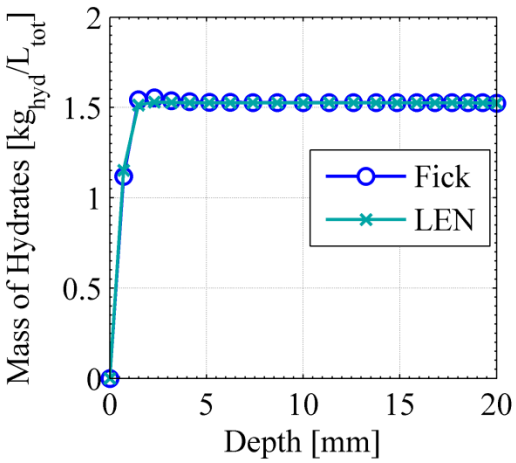

Figure 2.7: Mass of hydrated PC phases ([kg_{solid}/L_{tot}]) after 280 days of simulated DI water leaching. Note that the first node at depth = 0 corresponds to the external solution.

The main finding from this exercise is that, the LEN model is slower to approach steady state than the Fickian, but at 280 days the differences in transport models have greatly diminished. This result can be explained through examination of the magnitudes of primary species concentrations in Figs. 2.4-2.6; the primary ions in solution are the alkalis and OH^-, each on the order of 0.1 M. Thus, the charge coupling in the LEN model is achieved primarily through the balance of these three ions, resulting in a system that behaves similar to the binary electrolyte case since Na^+ and K^+ both possess a single positive charge.

2.4.3. Example 3: Concentrated single-salt leachant

Ammonium nitrate solution is commonly used to enhance the rate of decalcification of cementitious materials, but its single-salt electrolyte composition makes it an informative case to study from the perspective of charge-coupling phenomena. Results of simulated ammonium nitrate (AN) solution leaching are illustrated in Figs. 2.8-2.13. In contrast to the case of DI leaching, the profiles of pH, Ca, Si, and Al, profiles exhibit differences after 280 days of simulated leaching. Although the trends in these simulations are very much the same, the region of sharp pH depression (at ca. 5 mm depth) has progressed approximately 1-2 mm farther in the

Fickian model than in the LEN. Similarly, the peaks of Ca, Si, and Al concentrations are nearer to the specimen surface in the Fickian model.

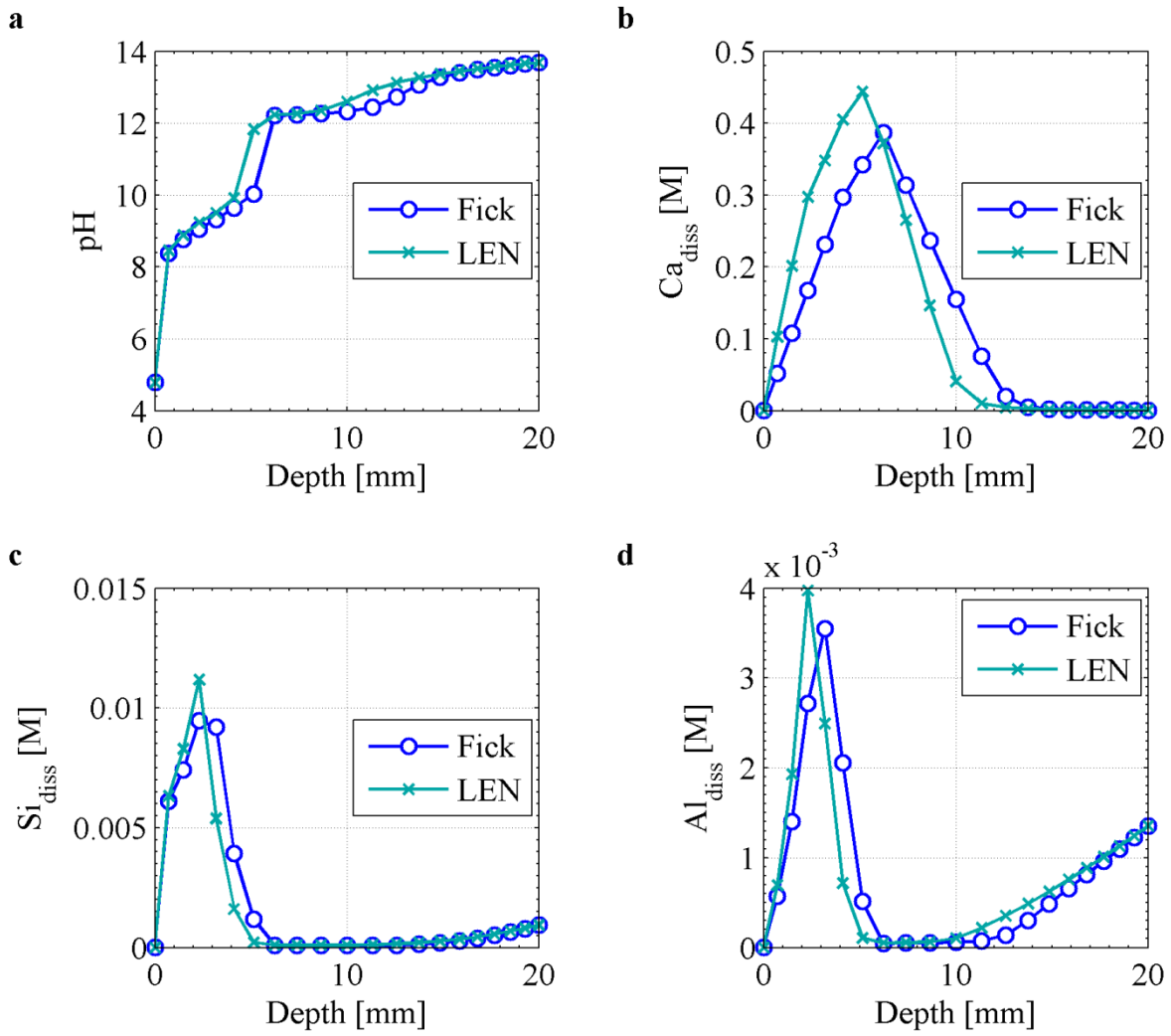

Figure 2.8: Comparison of a) pH, b) Ca, c) Al, and d) Si aqueous concentration profiles predicted by the Fickian and LEN transport models for the case of AN leaching of PC after 280 days of simulated leaching.

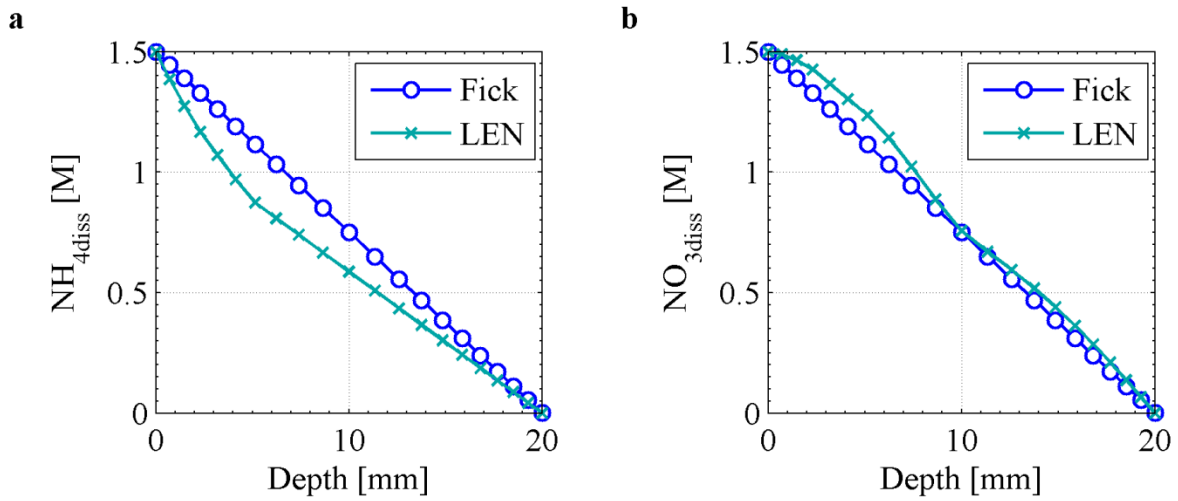

Figure 2.9: Comparison of a) ammonium and b) nitrate primary species concentration profiles predicted by the Fick and LEN transport models for the case of AN leaching of PC.

In Figs. 2.9a and 2.9b the total dissolved concentration profiles of the primary species NH_4 and NO_3 are plotted, respectively. In the 10 months of simulated time, the Fickian model predicts steady-state concentration profiles of both primary species, but in the LEN model, both NH_4 and NO_3 fail to reach steady state. Moreover, the NH_4 profile falls below the steady-state profile whereas the NO_3 profile falls above. To elucidate the reason for these differences, the distributions of NH_4 and NO_3 species within the depth of the material after seven days of simulation are plotted for the LEN model in Figs. 2.10a and 2.10b, respectively. Note that no solid phases bearing NH_4 or NO_3 were formed during simulation. The speciation of NH_4 at the left boundary consists of only NH_4^+ and the ion pair $NH_4NO_3^0$. Upon entering the alkaline PC porewater, appreciable amounts of NH_3^0 and $NH_4NO_3^0$ form, and because these two species are not present at the boundary, they diffuse outward. Thus, the ingress of total NH_4 into the external solution is hindered by "back diffusion" of these neutral species with the alkaline porewater acting as a source for NH_3^0 and $NH_4NO_3^0$. Incidentally, due to their neutrality, both species move according to their own concentration gradient and diffusion coefficient. NO_3 also forms ion pairs with both Ca^{+2} and K^+ within the PC porewater, but in general the distribution of NO_3 within PC porewater is more similar to its distribution at the boundary than is NH_4.

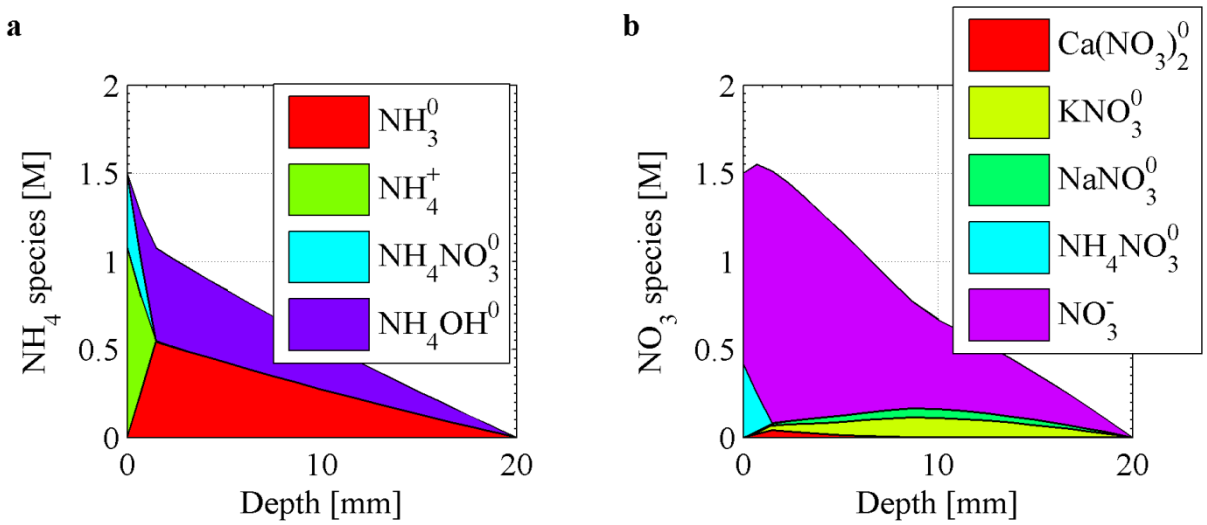

Figure 2.10: Distribution of predominant NH_4 species (a) and NO_3 species(b) within the pore solution after 28 days of simulated AN leaching using the LEN model.

As demonstrated in Fig. 2.11, the profiles of primarily cationic primary species also exhibit differences between the Fickian and LEN models. Similar to NH_4 and NO_3, the concentrations of both Na and K in Figs. 2.11a and 2.11b, respectively, have not reached steady state but are instead biased above the steady state profile. The LEN concentration profile of Mg, shown in Fig. 2.11c, exhibits a peak that is nearer to the left boundary and two times greater in magnitude than the Fickian model prediction.

As illustrated in Fig. 2.1, a number of primary species such as Mg and Ca exhibit solubilities that are highly sensitive to pH in the range of 12-13. Indeed, in the AN leaching case, the solubility of Mg has increased by six orders of magnitude due to the change in porewater pH (Fig. 2.11b). For these primary species, the choice of transport model can exert considerable influence on leaching behavior because the estimate of ion flux out of the material is determined by the concentration profile near the boundary. As such, the finite difference approximation of the gradient between the first and second nodes for Mg in Fig. 2.11b, is four times greater for the LEN model.

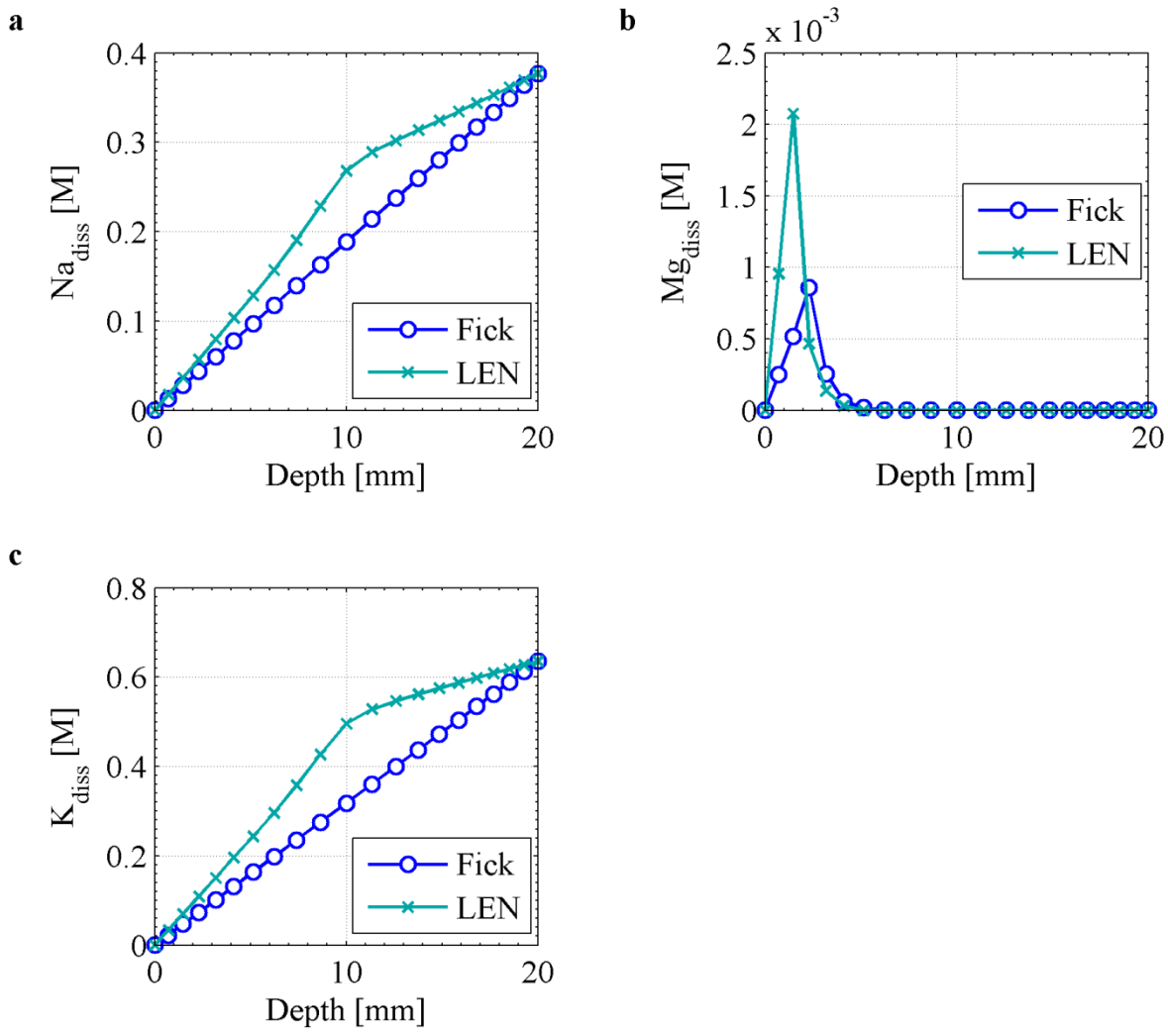

Figure 2.11: Comparison of typically cationic primary species profiles predicted by the Fick and LEN transport models for the case of AN leaching of PC.

The concentration profiles of both CO_3 and S, shown in Figs. 2.12a and 2.12b, suggest a fundamentally similar behavior in the release of these two ions. Interestingly, the CO_3 peak is lower in the Fickian case than in the LEN, whereas the peak in S concentration near the boundary is higher in the LEN case. Similar to the other non-precipitating species, Cl (Fig. 2.11c) has not reached steady state in the LEN model after 280 days of leaching.

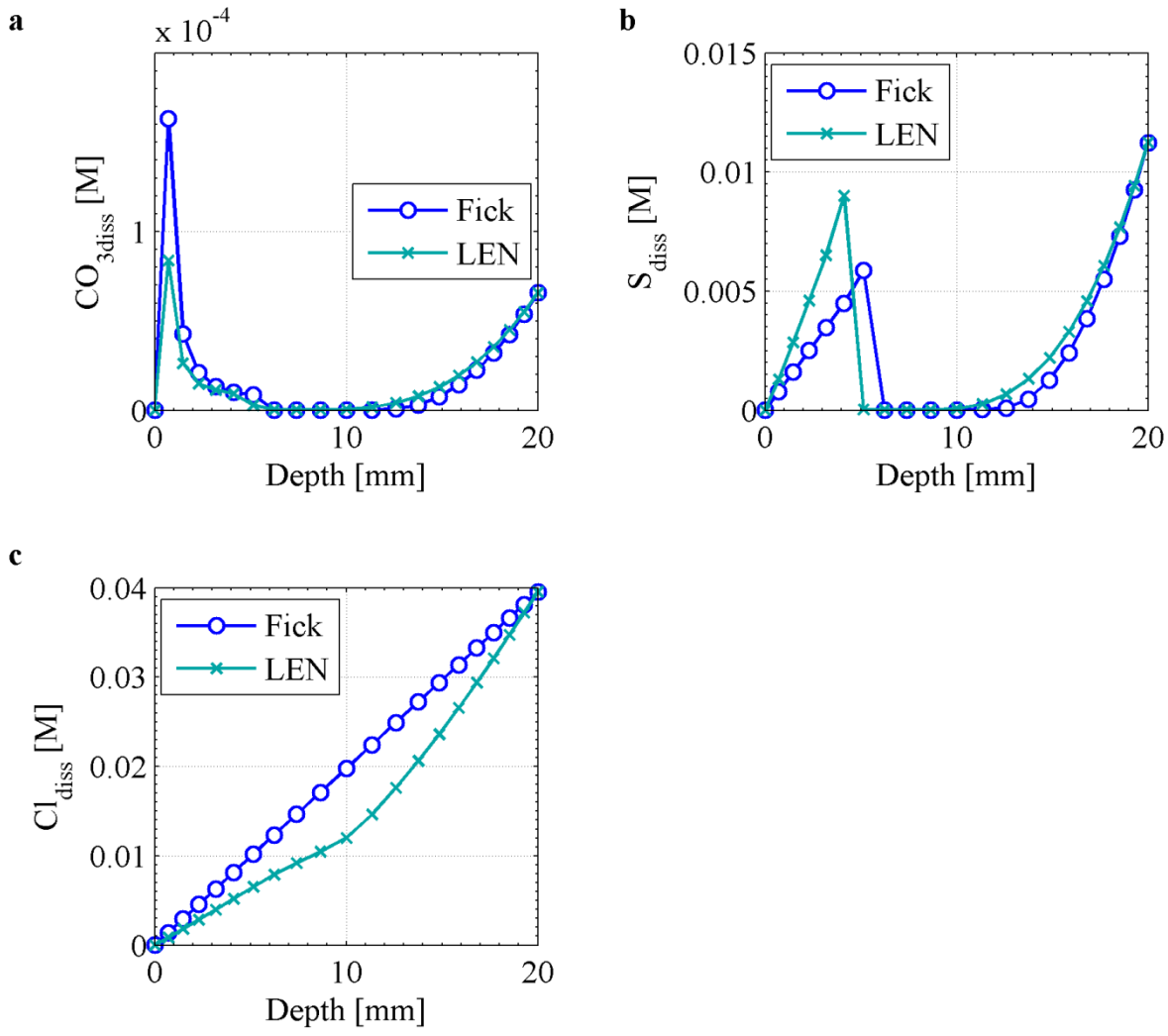

Figure 2.12: Comparison of typically anionic primary species profiles predicted by the Fick and LEN transport models for the case of AN leaching of PC.

Fig. 2.13 illustrates the predicted total masses of hydrates along the depth profile of the PC material, and, whereas the trends predicted by both models are quite similar, a distinct peak of reprecipitation at half the material depth occurs approximately 2 to 3 mm farther into the material in the Fickian model simulations at 280 of leaching. Such differences may not only prove to be significant for the prediction of mechanical properties of degraded materials but may also be exacerbated when the effect of porosity and tortuosity change on transport is considered.

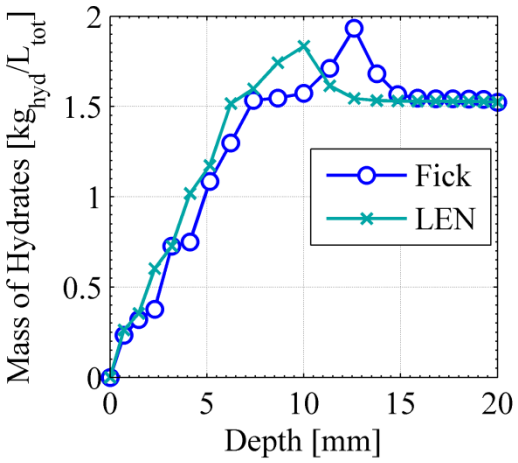

Figure 2.13: Profile of the predicted mass of hydrated PC phases [kg_{solid}/L_{tot}] after 280 days of AN leaching.

The major finding of this exercise is that charge-coupling phenomena exhibit greater departures from Fickian diffusion for the AN leaching case as opposed to the DI case, which is perhaps indicative of greater complexity within the most abundant dissolved ions in the AN case. In addition to the high concentrations of NH_4 and NO_3 primary species and of the alkalis in the native porewater, the aqueous concentrations of dissolved Ca species increases to the order of 0.1 M in the near surface region. Satisfying electroneutrality is thus "complicated" by the presence of the divalent Ca^{+2} ion as well as $Ca(OH)^{+}$ and other aqueous Ca complexes and ion pairs.

2.4.4. Example 4: Concentrated multi-ionic leachant

The LEN and Fickian predictions of pH, Ca, Si, and Al concentration profiles for the case of waste form (WF) leaching are plotted in Fig. 2.14. Despite very similar trends, the two models exhibit slight differences in pH profile after 280 days of simulated WF leaching. The LEN model predicts higher peak Ca and Al concentrations whereas the Fickian model predicts a Si peak four times greater in magnitude than the LEN model prediction. A similar discrepancy is encountered for Al except that it is the LEN model which predicts a higher Al peak concentration.

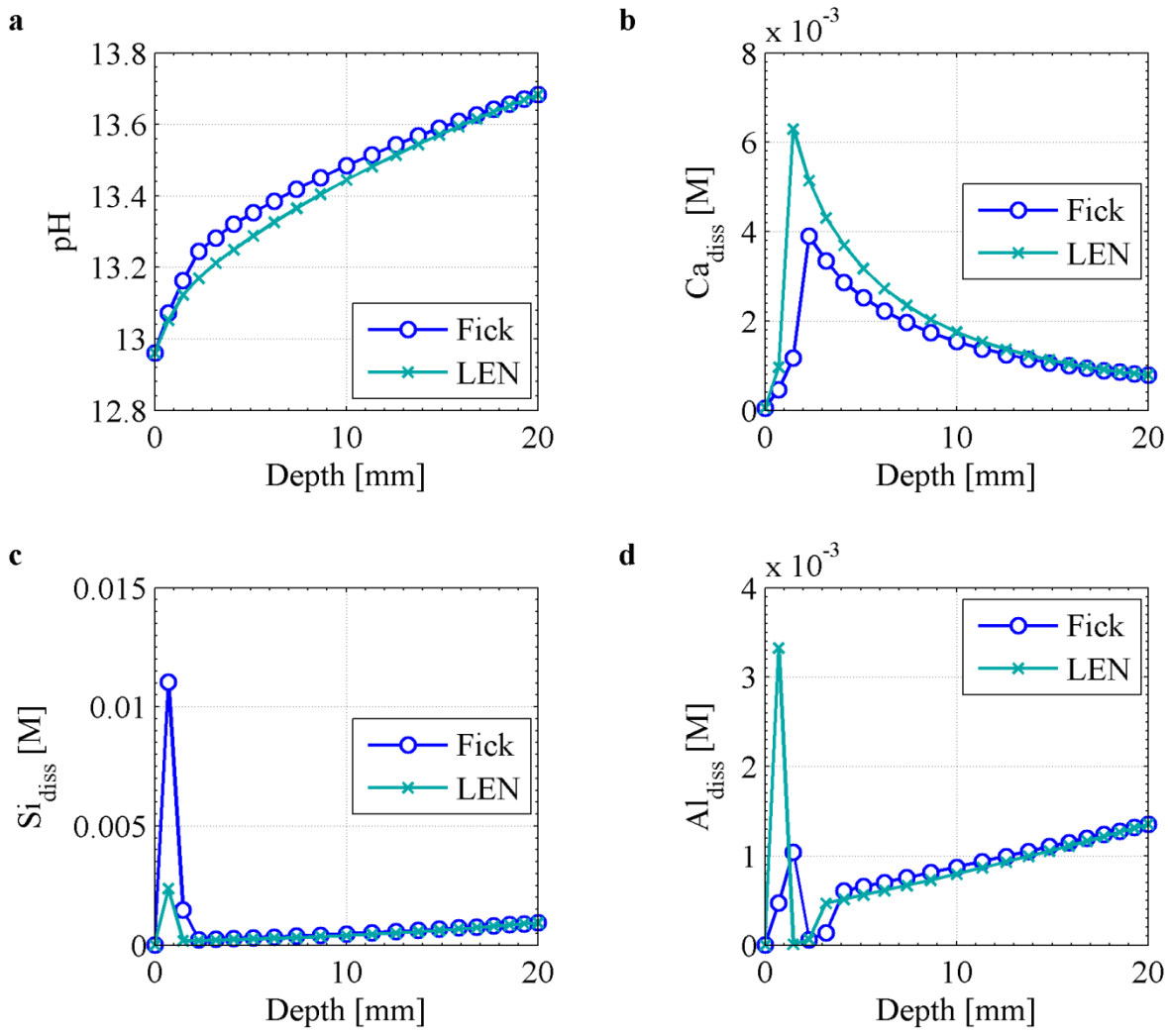

Figure 2.14: Comparison of concentration profiles of a) pH, b) Ca, c) Si, and d) Al predicted by the Fickian and LEN transport models for the case of WF leaching of PC.

As illustrated in Figs. 2.15a and 2.15b, the departures from steady state for Na and K predicted by the LEN model are relatively small after 280 days of leaching. Mg concentration, on the other hand, exhibits two distinct peaks near the specimen boundary in the Fickian model whereas the LEN model predicts only a single peak at approximately the same location. Inspection of the solid phases controlling Mg solubility in Figs. 2.16a and 2.16b reveals that the hydrotalcite-type M_4AH_{10} phase exhibits "complementary" peaks. In both transport models, M_4AH_{10} has reprecipitated near the boundary, but in the Fickian model, this reprecipitation peak has begun to dissolve. In this manner, the release behavior is linked not only to Al and OH, but as shown in

Figs. 2.16c and 2.16d, the formation of $Mg(OH)^{+}$ and $MgSiO_2(OH)_2^{0}$ further couples the transport of Mg to OH concentration and introduces a direct dependency on the concentration of aqueous Si.

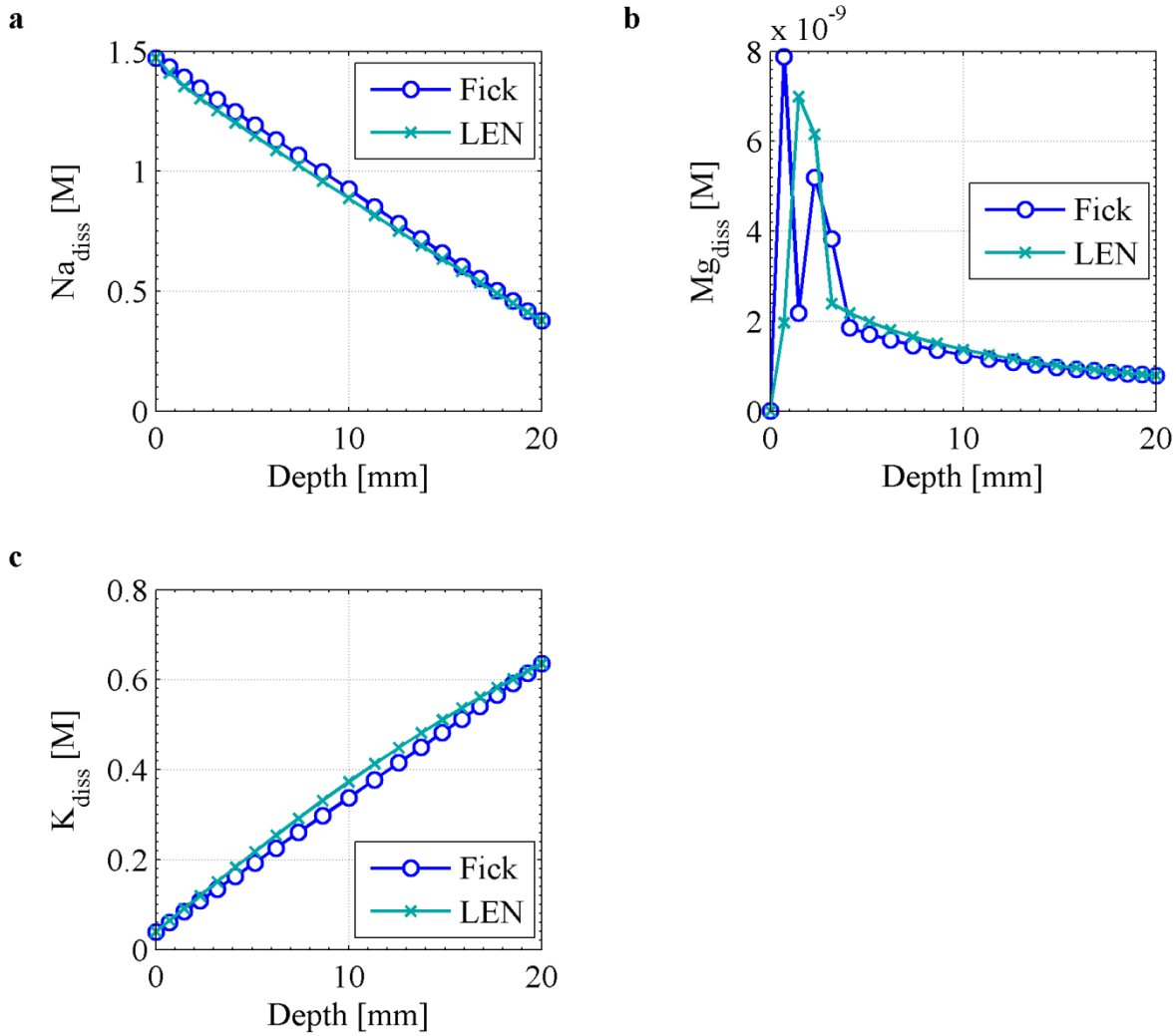

Figure 2.15: Comparison of typically cationic primary species profiles predicted by the Fick and LEN transport models for the case of WF leaching of PC.

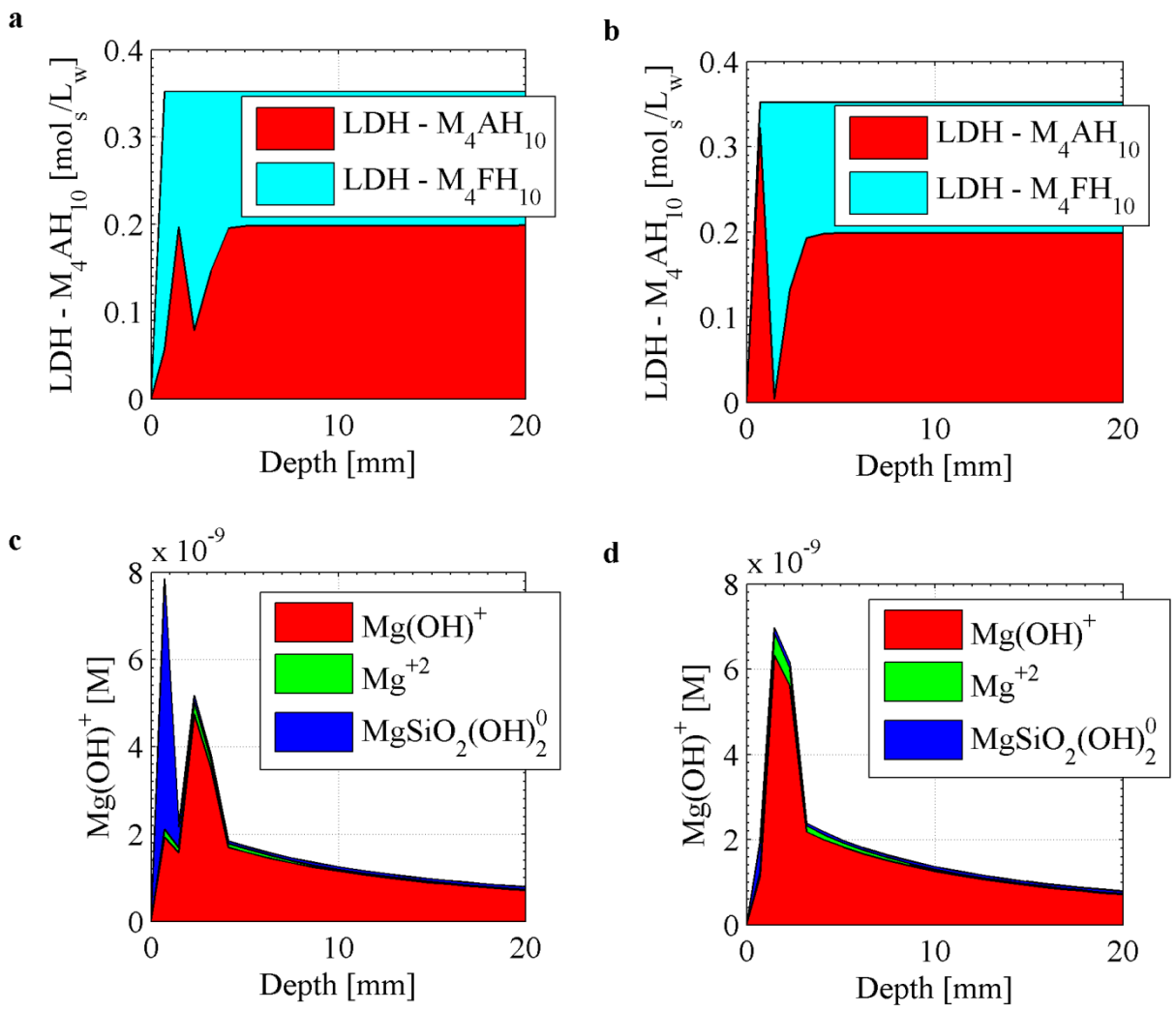

Figure 2.16: Comparison of the Mg-bearing solid phases predicted by the a) Fickian and b) LEN reactive transport models.

The predicted concentration profiles of typically anionic primary species differ very little between the LEN and Fickian models, as demonstrated in Fig. 2.17. The concentration profiles of the non-precipitating primary species Cl and NO_3 are nearer to their steady state distributions than in the AN leaching case but less so than in the DI leaching case. Similarly, the differences in predicted mass of hydrates at 280 days, as shown in Fig. 2.18, are trivial between the two transport models.

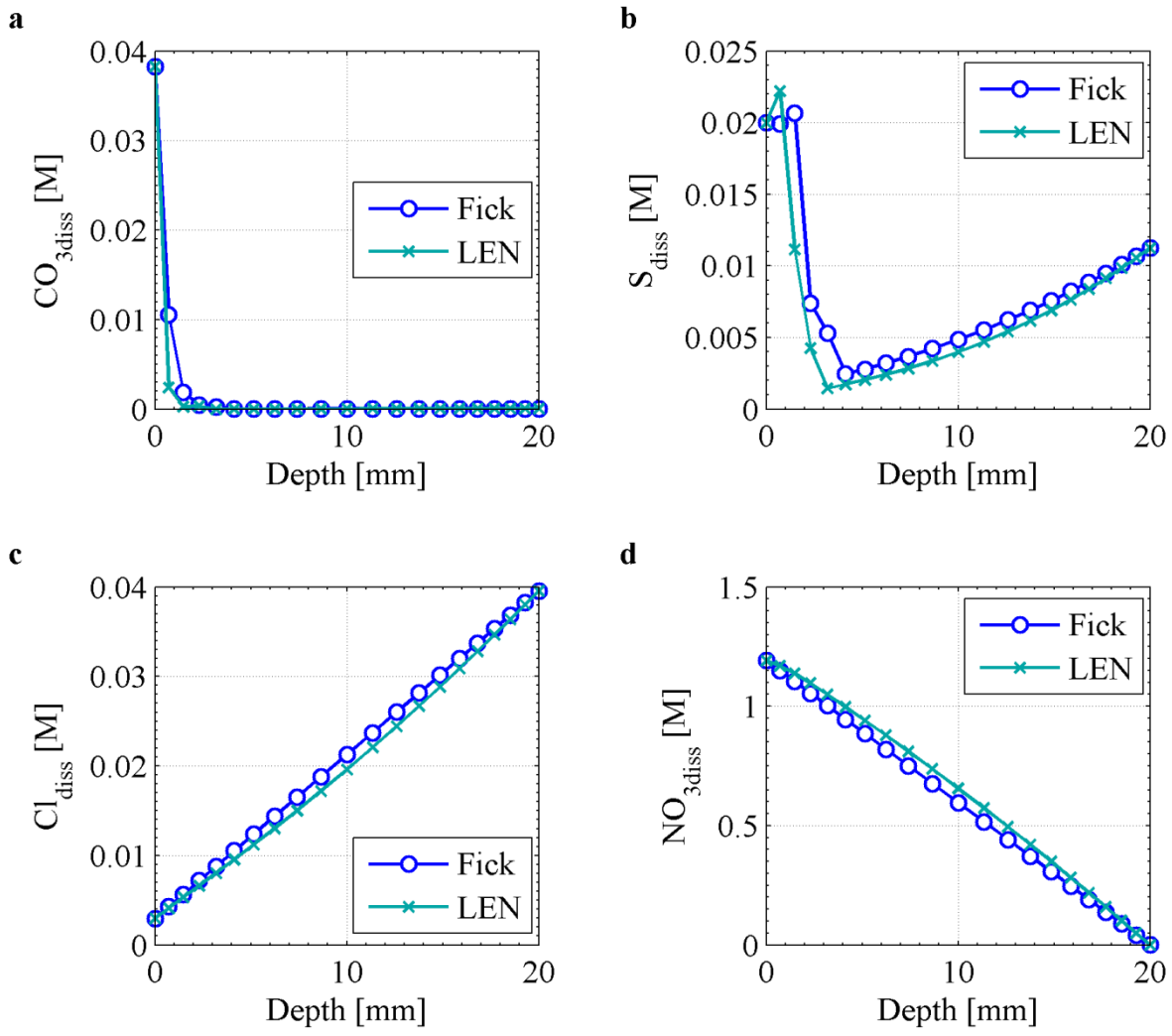

Figure 2.17: Comparison of typically anionic primary species profiles predicted by the Fick and LEN transport models for the case of WF leaching of PC.

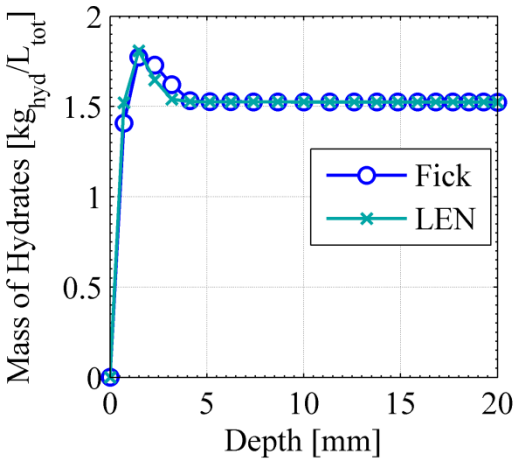

Figure 2.18: Profile of the predicted mass of hydrated PC phases [kgsolid/Ltot] after 280 days of WF leaching.

Given that a number of distinct ionic species are present in high concentrations in both the AN and WF leaching cases, it seems reasonable to conclude from this study that the complexity of the predominant ions in solution plays a key role in determining whether significant departures from Fickian transport occur in the NP model. This is likely not the only factor, however, since the WF solution must be regarded as more complex than that of the AN, yet the differences from Fickian are generally more pronounced in the AN case. Thus, it must also be acknowledged that any differences in the transport model predictions may be amplified in situations where the change in material pH is large. For the three leaching cases studied herein, AN represents the confluence of both sufficient major ion complexity and dramatic pH shift within the material, such that the observed model discrepancies are the greatest for this case.

2.5. Conclusions

By analogy to the Fickian diffusion finite difference approximation, the LEN form of the nonlinear NP system of equations for multicomponent transport has been solved using Newton-Raphson iteration. Both the Fickian and LEN solutions were demonstrated for the practical problem of leaching of a hydrated Portland cement. Comparisons of Fickian and LEN transport rates were made for transport in the absence of chemical reaction and for transport within a

reactive hydrated Portland cement. In the case of solute transport without chemical reaction, differences in primary species fluxes as large as a factor of two were found between the two transport models even though the concentration gradients of all ions were initially equivalent.

Comparisons of reactive transport reveal that the trends predicted by both models are quite similar in most cases. For deionized water leaching, no significant differences were observed between the two transport models. For the case of ammonium nitrate leaching, however, large departures from Fickian diffusion were observed for the LEN model due to the confluence of charge-coupling phenomena and highly pH-dependent primary species solubilities. In simulations of leaching with simulated waste form porewater, similar pH-dependent differences were observed for the LEN transport model; in particular, the LEN model predicted that after 280 days of simulated leaching, several non-precipitating species failed to obtain their steady state concentration profiles. Moreover, for the case of ammonium nitrate leaching, the uptake of both NH_4 and NO_3 was predicted to have important differences, with speciation proving to be a primary factor in determining these differences.

On the whole, comparison of the three leaching cases suggests that sufficiently complex major ion composition and dramatic changes in porewater pH are sufficient conditions for inducing departures from Fickian diffusion in the LEN model. These departures may have important implications for the release of trace constituents, which may be effectively governed by the chemistry and transport of major species in the LEN model. Furthermore, the differences between the Fickian and LEN models are not uniformly biased for the three leaching cases examined herein, which underscores the possibility that any regressed value of effective Fickian diffusion coefficient may be a strong function of the conditions under which it is obtained.

CHAPTER 3

3. SOLUTION OF THE NONLINEAR POISSON-BOLTZMANN EQUATION: APPLICATION TO CEMENTITIOUS MATERIALS[1]

Abstract

A robust numerical solution of the nonlinear Poisson-Boltzmann equation for asymmetric polyelectrolyte solutions in discrete pore geometries is presented. Comparisons to the linearized approximation of the Poisson-Boltzmann equation reveal that the assumptions leading to linearization may not be appropriate for the electrochemical regime in many cementitious materials. Implications of the electric double layer on both partitioning of species and on diffusive release are discussed. The influence of the electric double layer on anion diffusion relative to cation diffusion is examined.

3.1. Introduction

As the service life requirements of cementitious applications become more demanding, the need for mechanistically based, long-term prediction of material performance grows ever more pressing. More accurate estimation of constituent release is especially important for predicting performance of cementitious materials in waste management applications, wherein the cementitious matrix is relied upon to retain and/or impede migration of contaminants. Describing ionic transport in cementitious materials is complicated by the interplay of several factors including constituent retention via ion-exchange and adsorption, precipitation and dissolution of solid phases, the formation of expansive products which may lead to cracking, and the movement of ions through an often restrictive and tortuous pore space. Additional complications are apparent at the boundaries between cementitious materials and geologic media, where dramatic disparities in chemistry can induce large gradients in ionic composition (e.g., pH, ionic strength, etc.). Exacerbating this complexity is the fact that, even if relatively high ionic strength cement

[1] Published in Cement and Concrete Research, 44 (2013)

pore solution were considered in isolation, localized ion-ion and ion-solvent interactions might still play a significant role in determining the rate of ion transport [47, 83, 84].

A further confounding effect that seems to have been obscured by the aforementioned aspects of cement complexity is the much faster apparent diffusion of anions as compared to cations in steady-state through-diffusion experiments. In such experiments, two parallel faces of a cementitious specimen are exposed to two different solutions, an "upstream" solution with high tracer concentration and a "downstream" solution with little to no tracer present. One-dimensional diffusion subsequently occurs through the cementitious membrane due to the concentration difference ΔC_i of species i between the downstream and upstream compartments. Observed diffusivity D_i^{obs} of species i is calculated from

$$J_i = -D_i^{obs} \frac{\Delta C_i}{\Delta x} \tag{3.1}$$

where Δx is the width of the cementitious membrane, and the flux of species i, that is, J_i, is calculated from the change in concentration of i in the downstream compartment per time interval between measurements of i. Steady state is assumed when J_i is constant after successive measurements. Atkinson et al. found that D_i^{obs} for cations and anions measured in diffusion cell experiments may differ by up to an order of magnitude with decreasing water/cement ratio[85]. Others have reported observed anion diffusivities approximately five to twenty times greater than cation diffusivities, as demonstrated in Table 3.1 [85-88]. Such differences may become very important when predicting the rate of ingress of corrosive species, such as chloride or sulfate, and the rate of egress of constituents of potential concern (e.g., Tc-99 in nuclear waste management applications).

Table 3.1: Apparent diffusivities reported in the literature from diffusion cell experiments on cementitious materials. Free diffusivities of Na^+, K+, and Cl^- in water are 1.334, 1.957, and 2.032 [10^{-9} m^2/s], respectively [82].

				D_i^{obs} [10^{-12} m^2/s]		Diffusivity Ratio
Reference	Salt	Upstream Salt Conc. [M]	Water/Cement [-]	Cation	Anion	Anion/Cation
[87]	NaCl*	0.5	0.45	0.83	4.2	5.1
	NaCl*	0.5	0.45	0.85	10.8	12.7
	NaCl#	0.5	0.40	1.35	826	612
	NaCl#	0.5	0.40	1.6	7.0	4.4
	NaCl	0.5	0.35	1.32	6.8	5.2
[88]	NaCl	1.0	0.4	0.19	3.2	16.8
	NaCl	3.0	0.4	0.33	1.8	5.5
	KCl	0.5	0.4	0.2	3.7	18.5
	KCl	1.0	0.4	0.35	2.9	8.3
	KCl	2.0	0.4	0.46	1.9	4.1

*duplicate experiments.
#duplicate experiments (first case apparently in error in context of other reported data)

Observations of disparate cation/anion diffusivities coupled with measurement of significantly high membrane potentials and zeta potentials [86, 89-91] in cementitious materials and their constituent phases led Chatterji and Kawamura [88, 92] to suggest the electric double layer (EDL) as the underlying cause of disparate ionic diffusivities and to propose a qualitative description of the process. The quantitative descriptions of EDL theory are rooted in the early 20th century [93-95], and since that time, numerous investigations have aimed at illuminating manifestations of the double layer in various materials. Of particular interest are studies of the EDL in clays wherein anions are repelled by Coulombic forces from the negatively charged clay surface [96-98]; the effect of this repulsion is an exclusion of ions from a fraction of the pore space which serves to limit the area available for anion diffusion and, hence, slow anion diffusion with respect to cation diffusion [36, 99-103]. Slower anion diffusion is precisely opposite the observation of ionic diffusion in cement diffusion-cell through-diffusion

experiments despite the expectation that the surface charge of calcium-silicate-hydrate (C-S-H), the primary solid phase of cementitious materials, is expected to be negative also at the pH of the pore water (typically about 12.5 for ordinary Portland cements). As the surface charge of C-S-H is determined by the amphoteric silanol site, depression of the pore solution pH could lead to a reversal of the surface charge and *cation* exclusion, but this situation is unlikely given the buffering capacity of Portland cement systems.

Due to the complexity of cementitious materials in both composition and in pore space morphology, a number of factors in addition to EDL effects may be fully or partially responsible for enhanced anion diffusion in cementitious materials. Unfortunately, a full mechanistic description of disparate ionic diffusivities originating from EDL phenomena in cementitious materials has yet to be developed; a first step toward such a description is the modeling of the EDL. Typically, the effects of the EDL are addressed through a simplified version of the Poisson-Boltzmann equation (PBE), the Gouy-Chapman formulation, which is valid for low ionic strength symmetric systems with symmetric electrolyte composition, that is, every cation of the bulk solution with valence $+z$ is accompanied by an anion of valence of $-z$. Recently, Friedmann et al. [104] have demonstrated the effects of the EDL on transport in simple pore geometries using the analytical solution of the PBE and assuming a symmetric electrolyte composition of the pore solution, a condition that need not hold in real systems.

The objective of the research presented here is to develop and use a numerical solution of the *full nonlinear* PBE for the purposes of modeling the electric double layer for asymmetric non-dilute pore water compositions of cements. For the sake of conceptual and computational simplicity, pore boundaries in this work are envisaged as uniformly charged cylinders or parallel plates; however, a primary advantage of the finite difference solution is that it is extensible to arbitrary pore geometries provided that the pore boundary is sufficiently smooth. The pore water composition and pore size distribution of a blended cementitious mortar were measured in order to demonstrate the possible effects of the EDL on diffusion in a model cementitious material. Solutions of the PBE are used, then, to ascertain 1) the degree of divergence of the linear and nonlinear solutions for expected conditions in cementitious materials and 2) whether the effect of the EDL on diffusion may be significant for the relevant range of pore sizes encountered in cementitious materials.

3.2. Experimental Methods

3.2.1. Sample preparation

Structural vault concrete (SVC) samples were prepared by mixing ordinary Portland cement, blast furnace slag, coal fly ash, water, and quartz sand in the proportions listed in Table 3.2, resulting in a water-to-binder (w/b) ratio of 0.45. The formulation of SVC is within the family of compositions used as vault concretes in nuclear waste management applications [1]. SVC specimens were cast into cylindrical molds with 10.2 cm diameter and 20.4 cm height. Specimens were unmolded after 24 hours, and allowed to cure at 98 ± 2% relative humidity and 20 ± 2°C for 60 days.

Table 3.2: Proportion of mix components, in mass percent.

Component	Mass %
BFS	8.0
FAF	16.9
OPC	5.40
QS	55.0
Water	14.6

3.2.2. Pore water expression

Expression of pore liquid from saturated SVC cylindrical specimens was performed by SIMCO Technologies, Inc. (Québec City, Québec, Canada) according to the triaxial compression method set forth by Barneyback and Diamond [105]. Pore solution was collected and analyzed for chemical composition of Cl^- and OH^- using potentiometric titration, and for Ca^{+2}, Na^+, K^+ and SO_4^{-2} using inductively coupled plasma optical emission spectroscopy [106].

3.2.3. Porosimetry

Two porosimetry techniques were performed on crushed and vacuum-dried mortar samples. Mercury intrusion porosimetry (MIP) was conducted by Micrometerics (Norcross, GA, USA) using a 15 second pressure equilibration time and an assumed mercury contact angle of 130º, resulting in an "intrusion diameter" distribution of pores ranging from approximately 400 µm to 4 nm in diameter. Two intrusion cycles were executed sequentially in order to determine the volume of "ink-bottle" pores (pores connected to the mercury accessible porosity only via a smaller pore), within the specimen [107]. Nitrogen adsorption/desorption experiments were performed on vacuum-desiccated specimens using a Micromeritics ASAP (Accelerated Surface Area and Porosimetry System) 2010. Pore size distribution and pore volume of pore diameters between 2 to 600 nm were calculated using the BJH (Barret, Joyner, and Halenda) model applied to both adsorption and desorption isotherms. An estimate of specific surface area was also made using Brunauer-Emmett-Teller theory applied to the nitrogen adsorption isotherm [108].

Additionally, ASTM procedure C 642 [109] was performed to quantify water-accessible, or "total", porosity and bulk density.

3.3. EDL modeling

Adsorption of ions onto solid surfaces induces a gradient in electrical potential ψ [V] near the solid-pore liquid interface of charged porous media. The excess surface charge due to adsorbed species must be balanced by the presence of counter-ions in a "diffuse swarm" in the near-surface region, and these two regions are collectively referred to as the electric double layer (EDL). The interdependence of the diffuse layer charge density ρ_D [C/m^3] and ψ gives rise to the elliptic partial differential equation termed the Poisson-Boltzmann equation:

$$\nabla^2\psi = -\frac{\rho_D}{\epsilon_0\epsilon} \tag{3.2}$$

where ϵ_0 is the permittivity of free space [8.854 x 10^{-12} C/V/m], ϵ is the dielectric constant of the solution [-], and ∇^2 is the Laplace operator. Concentration of a particular species at a distance x [m] normal to a solid surface depends upon the energy state of that species and is therefore given

by the Boltzmann distribution. Thus, ρ_D is simply the difference in positive and negative charge distributions for all species i, such that

$$\rho_D = e\mathrm{N_A}\sum_i z_i C_{b,i}\exp\left(\frac{-z_i e\psi}{\mathrm{k_B}T}\right), \tag{3.3}$$

where $C_{b,i}$ is the concentration in the bulk pore solution [mol/m^3], e is the elementary electrostatic charge [C/particle], $\mathrm{N_A}$ is Avogadro's number [particles/mol], and $\mathrm{k_B}$ is the Boltmann constant [J/K] [110]. For small distances from a charged surface and for very large values of ψ, the Boltzmann distribution runs into difficulties because it may predict impossibly high values of concentration of ions given their finite sizes , however, this problem is alleviated by limiting the number of near surface charges to a maximum determined by the number of available "adsorption" sites within the near-surface region of finite thickness termed the "Stern layer" [111]. For the purposes of this work, the effects of the Stern layer are not taken into account explicitly; rather, it is assumed that the thickness of the Stern layer is negligible as compared to the width of the pores in question and that balancing of the structural charge by the Stern layer is negligible such that the effective potential boundary condition to be solved, ψ_{bc}, is equivalent to the potential of the outer Helmholtz plane ψ_δ [112]. Moreover, the systems considered are assumed to be open such that the bulk concentrations $C_{b,i}$ are constant values which implies that masses of ions in the EDL are negligible compared to the bulk concentrations.

Combining Eqs. (3.2) and (3.3) yields the general form of the *full nonlinear* PBE:

$$\nabla^2\psi = \frac{-e\mathrm{N_A}}{\epsilon_0\epsilon}\sum_i z_i C_{b,i}\exp\left(\frac{-z_i e\psi}{\mathrm{k_B}T}\right). \tag{3.4}$$

Eq. (3.4) may be linearized if $z_i e\psi \ll \mathrm{k_B}T$, that is, where the electrical potential energy of an ion ($z_i e\psi$) is small compared to its thermal energy ($\mathrm{k_B}T$), such that

$$\nabla^2\psi = \kappa^2\psi \tag{3.5}$$

where $\kappa^2$is the Debye parameter, given as [94]

$$\kappa^2 = \frac{e^2\mathrm{N_A}}{\epsilon_0\epsilon\mathrm{k_B}T}\sum_i C_{b,i}{z_i}^2. \tag{3.6}$$

Eq. (3.4) is by far the most commonly employed version of the PBE; however, electrophoretic measurements of hydrated cement and its constituent solid phases indicate that the magnitude of the electrokinetic (zeta) potential (which we assume approximates the potential of the Helmholtz plane, ψ_δ) for cement is typically on the order of tens of millivolts, in which case the exponential terms may not be neglected [89, 92]. In systems for which linearization of the PBE is not appropriate, simplification of Eq. (3.4) is still possible with the assumption that the system is comprised of a single symmetric electrolyte, that is, for every cation of valence $+\zeta$ there exists an anion of valence $-\zeta$. Assuming symmetry, the exponentials of Eq. (3.4) may be combined to yield

$$\nabla^2\psi = \frac{-2e\mathrm{N_A}}{\epsilon_0\epsilon}\zeta C_i \sinh\left(\frac{\zeta e\psi}{\mathrm{k_B}T}\right) \tag{3.7}$$

for which analytical solutions are possible; however, experimental evidence indicates that constituents of real cementitious pore solutions are unlikely to be symmetric or of a single valence [113].

The full nonlinear PBE only assumes that the configuration of charges in proximity to a charge surface follows a Boltzmann distribution and may be solved numerically as follows. The left hand side of Eq. (3.4) is replaced by a second order central finite difference, and the exponential on the right hand side is expanded as the infinite Taylor series:

$$\exp(\xi) = \sum_{n=0}^{\infty}\frac{\xi^n}{n!} = 1 + \xi + \sum_{n=2}^{\infty}\frac{\xi^n}{n!} \tag{3.8}$$

with $\xi = -z_i e\psi/\mathrm{k_B}T$. Thus, the exponential function may be subdivided into a linear part, ξ, and a nonlinear part, $1 + \sum_{n=2}^{\infty}\frac{\xi^n}{n!}$. Solution of Eq. (3.4) then follows closely the method proposed by Nicholls and Honig [114] excepting that electrolyte symmetry was not assumed. The value of potential at given node, ψ_0, is expressed as a function of the values of ψ at the nearest neighboring nodes, the constant term, and the power series of ξ

$$\psi_0 = \left[\sum_{all\ k}\psi_k + \left(\frac{e\mathrm{N_A}}{\epsilon_0\epsilon}\sum_{all\ i} z_i C_{b,i}\left(1 + \sum_{n=2}^{\infty}\frac{\xi^n}{n!}\right)\right)h^2\right] \Bigg/ \left(\sum_{all\ k} 1 + \kappa^2 h^2\right), \tag{3.9}$$

where k represent the indices of the six nearest neighbors $[(x-1,y,z),(x+1,y,z),\dots]$ and h is the grid spacing [m]. For a discretization of L^3 nodes, Eq. (3.9) may be written in vector notation as

$$\boldsymbol{\Psi}^{t+1} = \mathrm{T}\boldsymbol{\Psi}^{t} + \mathbf{Q} \tag{3.10}$$

where $\boldsymbol{\Psi}^{t+1}$ is the $L \times 1$ vector of ψ values computed at the next iteration $t+1$, $\boldsymbol{\Psi}^{\tau}$ are the ψ values at the current iteration t, T is an $L \times L$ matrix of coefficient values, and $\mathbf{Q}$ is the vector of nonlinear terms. Successive "under relaxation" is applied to Eq. (3.10), and the nonlinearity $\mathbf{Q}$ is treated as a perturbation of the solution [114]. To maintain stability, $\mathbf{Q}$ is scaled by a factor $\omega_{\boldsymbol{Q}}$ that grows with each iteration; for example:

$$\omega_{\boldsymbol{Q}} = \begin{cases} 0.5t \text{ for } t \leq 20 \\ 1 \text{ for } t > 20 \end{cases}. \tag{3.11}$$

The final iteration algorithm is written as

$$\boldsymbol{\Psi}^{t+1} = \omega_{\Psi}\mathrm{T}\boldsymbol{\Psi}^{t} + (1-\omega_{\Psi})\boldsymbol{\Psi}^{t} + \omega_{\boldsymbol{Q}}\mathbf{Q} \tag{3.12}$$

where ω_{Ψ} is the relaxation parameter. Dirichlet boundary conditions ($\psi_{bc} = \text{constant}$) are imposed at the pore wall corresponding to the potential just beyond the Stern layer, assumed herein to be approximated by the zeta potential. Periodic boundary conditions are imposed at the "ends" of a pore, and values of ψ are then computed from Eq. (3.12) until the maximum change in ψ is less than a specified tolerance, here 10^{-4} mV. Once satisfactory convergence of the solution has been obtained, the concentration of any particular ion may be computed from the Boltzmann distribution

$$C_i = C_{b,i} \exp\left(\frac{-z_i e \psi}{\mathrm{k_B} T}\right). \tag{3.13}$$

The solution scheme was implemented in the commercial computational software package MATLAB (MATLAB 7.10.0, The MathWorks Inc., Natick, MA, 2000).

3.4. Results and Discussion

3.4.1. Porewater concentrations

The resulting composition of expressed pore water is shown in Table 3.3. The calculated ionic strength of this system is 110 mM, but measurements indicate a net excess charge of -6.8 mM. As the net excess charge is within the uncertainty bounds of the pH measurement, 12.0, hydroxide concentration was adjusted for charge balance of the solution, as listed in Table 3.3.

Table 3.3: Expressed pore water concentrations, in mM.

Ion	Ca^{+2}	SO_4^{-2}	K^+	OH^-	Na^+	Cl^-
Measured	1.35	1.25	38.37	103.31	62.25	4.34
Corrected	1.35	1.25	38.37	96.81	62.25	4.34

3.4.2. Porosimetry

The resulting cumulative and differential intrusion curves for both MIP and N_2 adsorption/desorption are plotted in Fig. 3.1. The first MIP intrusion indicates an intrusion threshold of approximately 100 nm and a steep increase in cumulative pore volume below this pore diameter, resulting in a cumulative pore volume of 0.209 [m^3 void/m^3 total] which agrees closely with the water accessible porosity of 0.23 measured by ASTM C 642 as shown in Table 3.4. The second MIP intrusion yielded an almost identical cumulative volume as the first intrusion; however, as illustrated in Fig. 3.1b, more than half of the intruded mercury from the first intrusion was not recovered during the first extrusion, suggesting that the steep increase of the first intrusion was due largely to the backfilling of ink-bottle pores. When corrected for this trapped mercury volume, the second cumulative intrusion measured a “non-ink-bottle” porosity of 0.092 [m^3/m^3] which is in very close agreement with the porosity value of 0.099 [m^3/m^3] measured by N_2 adsorption (which is only capable of probing pores less than approximately 100 nm in diameter), also shown in Table 3.4. Furthermore, the incremental intrusion curves of the second MIP intrusion and the N_2 intrusion demonstrate similar trends.

Table 3.4: Results of ASTM C 642 density and water accessible porosity determination, mercury intrusion porosimetry (MIP), and N_2 adsorption (N_2 Ads.).

ASTM C 642			MIP		N_2 Ads.	
Bulk density, dry [g/cm^3]	Bulk density, saturated [g/cm^3]	Porosity [m^3/m^3]	Porosity, 1st Intrusion [m^3/m^3]	Porosity, 2nd Intrusion [m^3/m^3]	Porosity [m^3/m^3]	BET specific surface area [m^2/g]
1.96	2.19	0.23	0.209	0.092	0.099	8.63

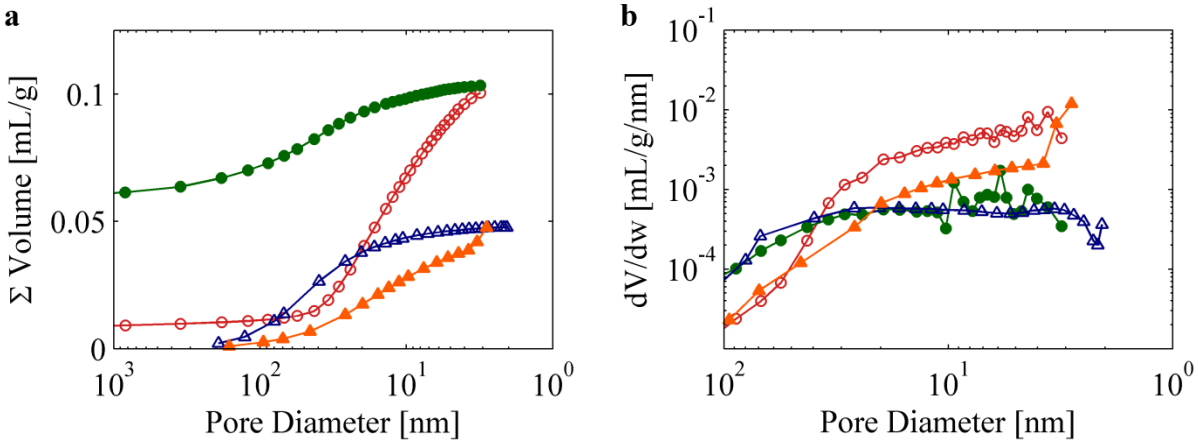

Figure 3.1: Cumulative intrusion volume (a), and differential intrusion volume (b) for MIP intrusion cycles 1 (open circles) and 2 (filled circles), and for N_2 adsorption (open triangles) and N_2 desorption (filled triangles).

Both porosimetry techniques suggest a finer pore structure than typically encountered for ordinary Portland cement (OPC). Whereas the median pore diameter of OPC generally lies on the order of 100 nm, the median diameter of the mortar as measured by N_2 adsorption is on the order of 50 nm. Of the four porosimetry curves, N_2 adsorption yields the smallest amount of fine pore volume and was therefore chosen as a bounding estimate of the smallest likely fraction of fine pores. A beta distribution was fit to the probability density function derived from the incremental N_2 adsorption, as shown in Fig. 3.2, and summary statistics from this fit are listed in Table 3.4.

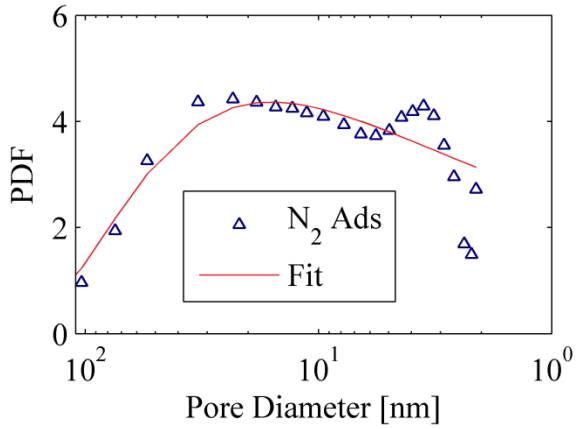

Figure 3.2: Experimentally determined N_2 adsorption incremental volume curve (N_2 Ads) and a beta distribution fit (Fit) to the curve.

Table 3.5: Statistics computed from the beta distribution fit to the N_2 adsorption incremental volume curve. Percentiles (pct.) indicate the percentage of the volume comprised of pores less than or equal to the given diameter [nm].

mean	std. dev	25^{th} pct.	50^{th} pct.	75^{th} pct.
58.6	7.8	23.4	47.5	83.0

3.4.3. EDL Modeling

For solution of the PBE, it is assumed that in a given pore, the surface potential is isotropic and the populations of species within the pore are constant. Aqueous ionic species are assumed to remain fully ionized, and chemical reactions including surface adsorption/desorption are not allowed to occur. Although the solution to the PBE is given for a single pore, the solution may be regarded as an average over all pores of a given size.

It is assumed that cylindrical pore boundaries may be reasonably approximated with a fine rectangular grid spacing, in this case 10^6 nodes. In order to avoid the trivial solution of constant ψ at all nodes for symmetric electrolytes, the initial values of ψ were set to zero at all nodes, save the boundary conditions; thus, the incremental solution of Eq. (3.9) was guaranteed to pass through the nontrivial solution.

3.4.3.1. Academic examples

The behavior of the nonlinear PBE can be illustrated with a hypothetical cylindrical pore measuring 10 nm in diameter with a uniform and constant surface potential. A zeta (boundary) potential value of -25 mV was chosen as a reasonable estimate for cementitious materials based on reported measured values [115]. The pore is filled with an electrolyte solution comprised of an arbitrary cation M^{+m} and anion A^{-n}. Three illustrative cases are presented herein. In Case 1, the pore is saturated with a 100 mM solution of symmetric monovalent or 1:1 electrolyte solution (e.g., MA). In Case 2, the pore is filled by a 100 mM asymmetric 1:2 electrolyte solution (e.g., MA_2) with a resultant ionic strength of 300 mM. For the last case (Case 3), the pore is filled with an asymmetric 1:2 electrolyte solution at 33 mM. Thus, Cases 1 and 2 both possess a cation concentration of 100 mM while Cases 1 and 3 both have an ionic strength of 100 mM. The potential profiles and cation/anion concentration profiles extending radially from the pore for all three cases are presented in Fig. 3.3 (a-c). Shown in the plots are the potential distribution (a) and ion distribution (b and c) for all three cases. Plot d) shows the deviations between the linear and nonlinear mean pore potentials (expressed as percent difference between the linear and nonlinear solution, that is $100\% * (|\psi_{linear} - \psi_{nonlinear}|)/\psi_{nonlinear}$) as a result of varying surface potential for the porewater concentrations of all three cases.

Fig. 3.3d reflects the difference in the linear and the nonlinear solutions, which is proportional to $\sum \exp(-z_i e\psi/k_B T)$. Accordingly, the difference reaches a minimum for vanishing ψ, and increases for increasing ψ, tending toward a maximum when z_i and ψ are opposite in sign. Assuming an asymmetric solution may be approximated by a symmetric monovalent solution leads to deviations which are apparent in the comparison of Case 1 (symmetric) and Case 2 (asymmetric) in Fig. 3.3d; the difference in mean potential for the symmetric and asymmetric cases is as much as 15% for a large surface potential.

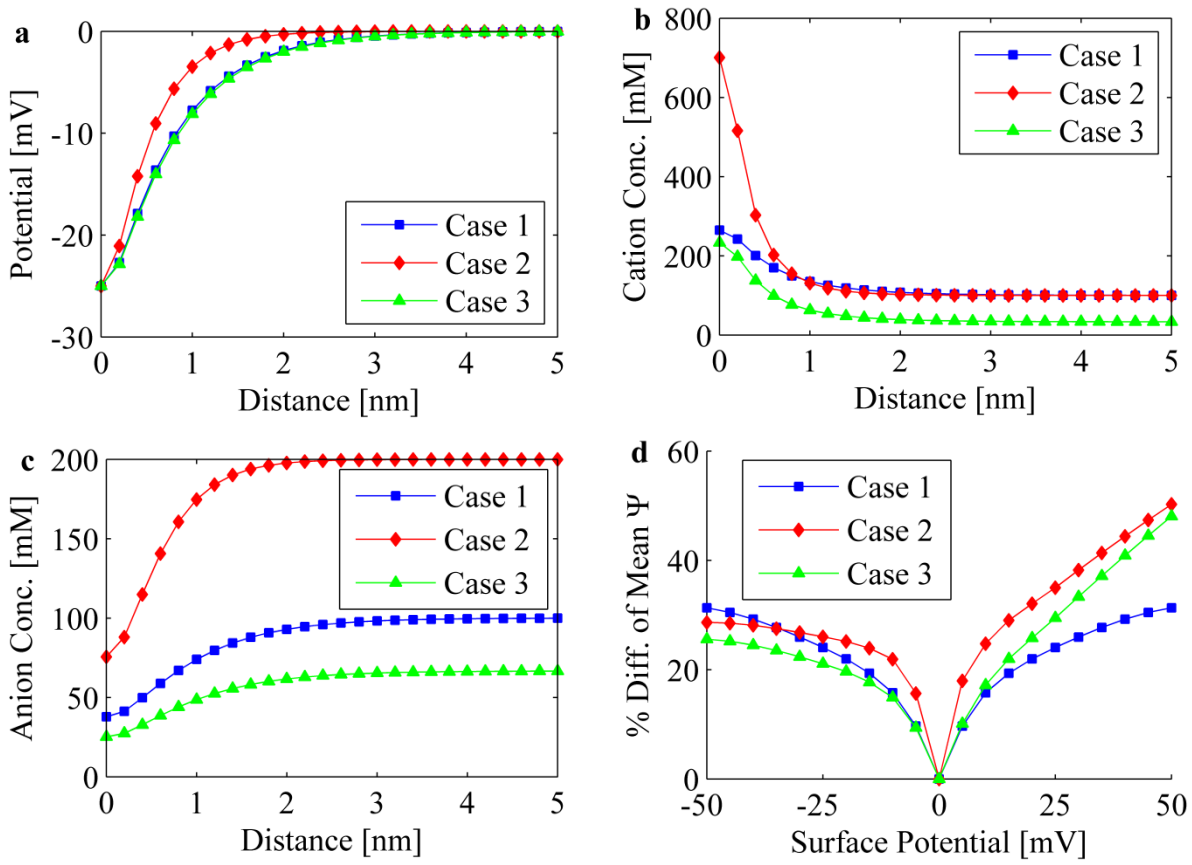

Figure 3.3: Simulated potential profiles for a 10 nm wide pore with constant surface potential of -25 mV and pore solutions of 100 mM MA (Case 1),100 mM MA2 (Case 2), and 33mM MA2 (Case 3), where M and A denote cations and anions, respectively. Shown are plots of potential distribution (a) and ion distribution (b,c) as a function of distance from the pore wall for all three cases. Shown in d) are deviations between the linear and nonlinear mean pore potentials (expressed as percent difference between the linear and nonlinear solutions) as a result of varying surface potential for the porewater concentrations of all three cases.

A number of observations are apparent from the comparison of the solution of the full nonlinear PBE for all three cases, shown in Fig. 3.3a - 3.3c The spatial extent of the diffuse layer is greater for Case 1 than Case 2, as the divalent M^{+2} ion can more efficiently neutralize the surface charge than the monovalent A^- ion. This neutralization occurs in spite of the molar concentration of A^- being twice the value of Case 1 and, as indicated in Eq. (3.3), is due to the linear dependence of local concentration on bulk concentration and an exponential dependence on the square of the valence state. The potential profiles for Cases 1 and 3 are nearly identical, yet the relative increase in M^{+2} concentration as compared to the bulk in Case 3 is significantly higher than the M^+ increase in Case 1. In all three cases, anion concentrations decrease markedly in the vicinity

of the surface charge. Therefore, with decreasing pore diameter, mean anion concentrations within a pore diminish while mean cation concentrations increase. Considering diffusion through one such pore and assuming the Boltzmann distribution holds in the presence of a concentration gradient, a few deductions may be made:

The net flux of cations through the pore will be determined by the combined effects of electrical retardation through interaction with the anionic surface layer (decreasing local intrinsic cation diffusivity) and of increased local concentrations of cations that serve to increase the diffusion gradient. The cross-sectional area available for anion diffusion will be reduced due to electrical repulsion from the anionic surface layer, thereby reducing the anion flux as compared to flux through a pore with an uncharged surface layer. In well-connected pore networks, the reduced area for anion flux should serve to reduce the observed diffusivities of anionic species.

If the pore diameter is small enough relative to the thickness of the EDL, anions will be *excluded* from the pore. Thus, small pores may serve to limit the accessibility of not only pores but pore pathways to anions. In well-connected pore networks, this phenomenon should also be expected to reduce observed diffusivity of anions; however, in poorly-connected networks, that is those containing many dead-end pores, the anion-specific tortuosity could be significantly reduced if the pore pathways from which anions are excluded are highly tortuous.

3.4.3.2. Application to blended cement mortar

The trends observed from rudimentary examples are, nonetheless, persistent in simulations of the more complex pore solution specified in Table 3.3. A surface potential of -25 mV was chosen as a plausible value for a hydrated cement system based upon electrokinetic measurements found in the literature [92, 104, 116, 117]. A useful metric for comparing the impact of the EDL on a particular species is the mean pore concentration, $C_{i,avg}$ [mM], which for a cylindrical pore with radius r_p [nm] is computed as the integral over the cross-sectional area of the pore

$$C_{i,avg} = \frac{2}{r_p^2}\int_0^{r_p} rC_i(r)dr. \tag{3.14}$$

The ratio of total positive dissolved charges to total negative charges $\sum z_i^+ C_{i,avg}^+ / \left|\sum z_i^- C_{i,avg}^-\right|$ (neglecting charges of the adsorbed ions), also gives an indication of the relative influence of the

EDL. Fig. 3.4 depicts mean pore solution concentrations $C_{i,avg}$ required to maintain electroneutrality within a pore normalized by the bulk concentration $C_{b,i}$ for a range of pore diameters relevant for cementitious materials. Also, plotted in Fig. 3.4d is the charge ratio for diffusing ions in solution. As expected, the concentration-altering, anion-excluding effect is exacerbated by both decreasing pore diameter and decreasing ionic strength, resulting in significant departures from bulk concentrations. At the ionic strength of the pore solution for the unleached mortar, approximately 5% of the connected pores possess at least twice as many positive charges as negative charges, whereas at a 10x dilution of the pore water (analogous to reductions by leaching), approximately 15% of the pores have a charge ratio of at least 2; at 100x dilution, this percentage increases to approximately 50% of the pores. The implications of these findings are discussed next.

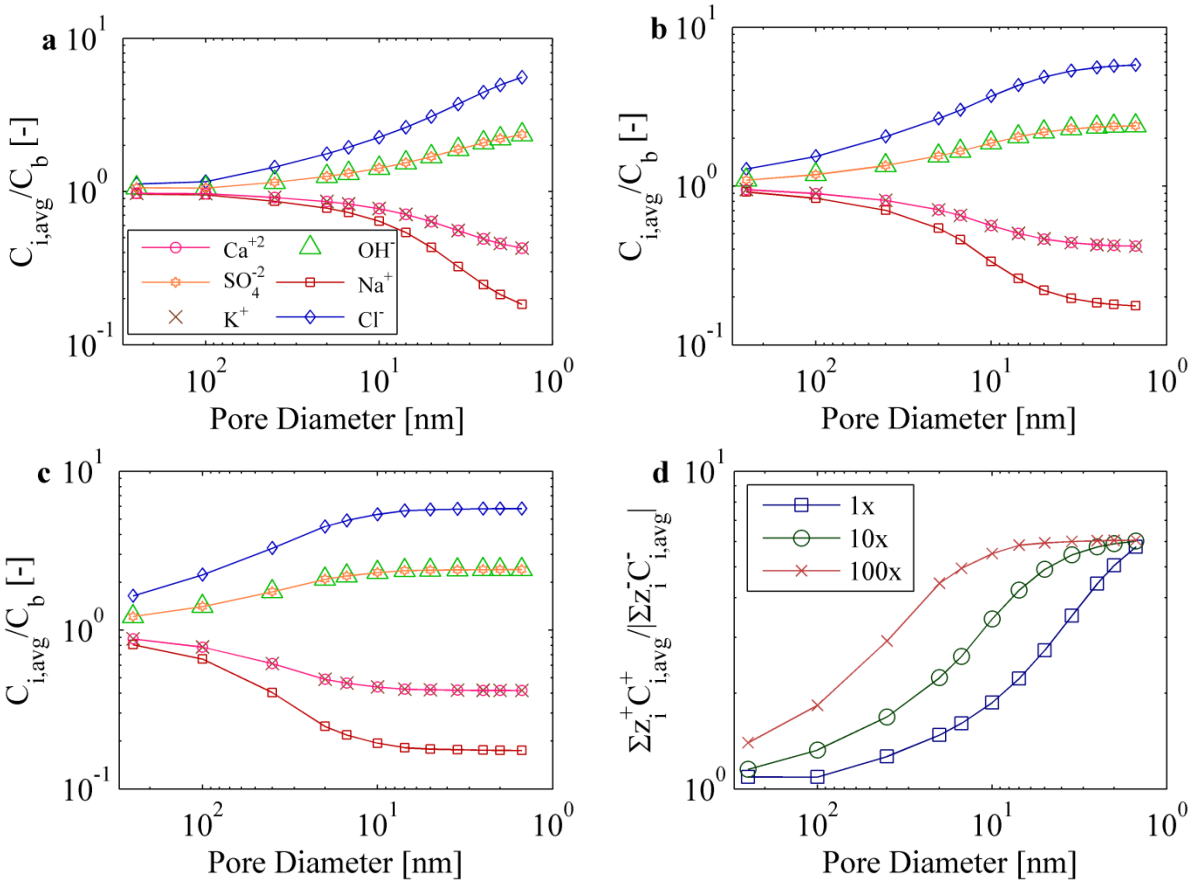

Figure 3.4: Normalized ion concentrations for variable pore diameters for a) the expressed pore solution, b) a 10x diluted pore solution, and c) a 100x diluted pore solution. d) The ratio of total

positive charge to total negative charge is calculated as $\sum z_i^+ C_{i,avg}^+ / \left|\sum z_i^- C_{i,avg}^-\right|$, where $+$ and $-$ denote cation and anion species, respectively.

3.4.3.3. Interpretation of diffusion cell experiments

The Fick's law formulation of Eq. (3.1) belies the complexity of multicomponent ionic diffusion in a porous medium, wherein the flux is more rigorously characterized by the Nernst-Planck equation applied to porous materials [40]

$$J_i = \tau\phi\left(-D_i^u \nabla(C_i) - \frac{D_i^u z_i \mathrm{F}}{\mathrm{R}T} C_i \nabla(\psi) - D_i^u C_i \nabla(\ln \gamma_i)\right) \tag{3.15}$$

where ϕ is the connected porosity available for diffusion [m^3/m^3], the tortuosity τ (≤ 1) [m/m] characterizes the distance that an ion traverses within the pore space, D_i^u [m^2/s] is the free liquid diffusivity of species i at infinite dilution, z_i is the valence state of species i, R is the ideal gas constant [J/mol/K], and γ_i is the chemical activity coefficient of species i [84]. In the bulk pore solution, intermolecular forces exerted between freely moving ions ensure an equilibrium orientation of ions such that electrical potential ψ remains zero throughout; however, as demonstrated previously, the potential near charged surfaces need not be zero. Because Eq. (3.15) is computationally taxing for realistic pore geometries on meaningful length scales, it is rarely solved in its full form. Instead, diffusion is most often simplified to a Fick's law formulation with various correction terms included; to compare these different formulations, it is convenient to cast Eq. (3.15) in terms of correction factors:

$$J_i = \frac{f^{C_i}(f^\tau \tau)(f^\phi \phi)}{f_i^R}\left(-D_i^u \nabla(C_i) - \frac{D_i^u z_i F}{\mathrm{R}T} C_i \nabla(\psi) - D_i^u C_i \nabla(\ln \gamma_i)\right) \tag{3.16}$$

where f^ϕ, f^τ, and f^{C_i} are corrections to the values of ϕ, τ, and C_i, respectively, and the factor f_i^R represents corrections to the flux due to chemical reactions (most often assumed to be adsorption reactions) of the diffusing species. The observed diffusivity may then be written as

$$D_i^{obs} = \frac{f^{C_i} f^s f^\tau f^\phi}{f_i^R} D_i^u \tau\phi. \tag{3.17}$$

where f^s represents the transform of the concentration-, potential-, and activity-gradient terms of the modified Nernst-Planck equation to single scalar value. Thus, Eq. (3.17) presents a

framework for evaluating possible mechanisms of disparate cation/anion diffusivities and will be used to assess whether any one correction factor can account for the half an order of magnitude disparity between observed cation and anion diffusivity.

The possibility that the chemical reaction factor for diffusing ions, f_i^R, gives rise to disparate cation/anion diffusivities cannot be completely dismissed without intimate knowledge of the chemical properties of the cementitious system, although such an effect should be negligible at steady state. The plausibility of whether a particular type of reaction could result in $f_{cation}^R / f_{anion}^R \geq 5$, however, is considered. Precipitation of the diffusing species is unlikely given the generally high solubility of the species used in the diffusion cell experiments (K^+, Na^+, Cl^-), but adsorption-type reactions of these ions have been widely reported. Uptake of alkalis is generally considered to occur as an adsorption onto the silanol sites of C-S-H [118] or as an interlayer occupation of the calcium-alumino-silicate-hydrates (C-A-S-H) [119]. The fraction of alkali incorporated during initial mixing is quite high and increases for low-calcium cements , but the partitioning of alkalis occurring into hydrated C-S-H is within a factor of two of the reported adsorption partitioning of chloride [120, 121]. Therefore, it is doubtful that f_i^R differs by a factor of five or more between species.

The phenomenon of anion exclusion is well documented for charged clay soils [97, 98, 122], and has been interpreted using the concept of an effective porosity , that is $f^\phi \phi^m$, wherein anions are confined to a fraction of the total porosity due to repulsion from the negatively charged pore wall. Thus, anionic concentrations are higher in the central region of the pore resulting in a higher diffusion gradient than would be indicated by macroscopic measurements of concentration. An estimate of the anion-excluded pore volume, which ignores overlapping diffuse layers, may be calculated by multiplying the Debye length (~ 1 nm for the solution given in Table 3.3) by the pore surface area (~10 m^2/g, Table 3.4), yielding an anion-excluded volume on the order of 10% of the total porosity and an f^ϕ equal to 0.90 and which decreases D_i^{obs} by 10%. This crowding of anions into the central regions of pores is necessarily accompanied by a rise in anion concentration (although the simulations presented herein give no indication that the resulting anion concentration should be higher than in the bulk solution due to the form of the PBE). Therefore, f^{C_i} for anions in this system would be calculated as 1.11 such that the factors f^{C_i} and f^ϕ would cancel one another, ruling out anion crowding as the primary origin of

disparate diffusivities in this particular cement mortar. Not only are the magnitudes of these factors too small to account for a factor of five difference in diffusivities, ascribing a macroscopic correction factor derived from microscale arguments neglects the inherent variability of the pore space. Moreover, the utility of such a formulation has been questioned, inasmuch as the excluded volume will depend strongly on the ionic strength of the pore solution which may also exhibit quite significant local variation.

Because of the variation of ionic diffusion coefficients for dissolved ionic species, the electrical coupling among species in the bulk solution, through the term $(D_i^u z_i C_i \, \mathrm{F})/(\mathrm{R}T)\nabla\psi$, serves to accelerate the movement of slower ions and retard the movement of faster ions, such that the ratio of $f_{Cl}^s / f_{(Na,K)}^s$ between species should be *at a maximum* equal to the ratio of their free liquid diffusivities, which for the species considered is approximately a factor of 2 [43, 82]. Snyder and Marchand [47] demonstrated that D_i^{obs} in nonreactive porous frit is only weakly dependent on concentration gradient in systems of ionic strength comparable to cement pore solutions. It is, therefore, unlikely that electrical coupling between ions could give rise to disproportionate rates of ion transport in the bulk solution. Within the EDL, however, the electric potential may have a strong effect on the transport of ions, and in solutions of low ionic strength, Coulombic interactions may indeed be the dominant factor in determining transport rate. Chatterji and Kawamura [92] argued that a high cation flux in the EDL could be the driving factor for disparate diffusivities if the cation flux were accompanied by an accelerated anion flux (in order to maintain charge balance) in the central region of the pore. No such mechanism is apparent from the analytical solution of the Nernst-Planck for an idealized pore given by Friedmann et al. [104]; rather, the ratio of cation to anion flux was found to be equivalent to the ratio of cation charge to anion charge within a pore [104]. This formulation of the Nernst-Planck, however, neglects the concomitant change in potential gradient in the presence of a concentration gradient. What is apparent from the simulations of the EDL presented herein is the relatively large fraction of porosity impacted by EDL effects. Considering that pores less than 23.4 nm constitute approximately 25% of the total pore volume measured by N_2 adsorption (Table 3.5), the probability that any percolating pathway traverses a pore with a mean charge ratio altered by a factor of approximately five (Fig. 3.4d) is necessarily quite high, resulting in pore "bottle-necking" as depicted in Fig. 3.5b. Thus, a fraction of the pore space may act as a filter,

facilitating passage of cations and deterring the passage of anions. Consistent with observations in clays, this assertion seems to suggest a faster diffusivity of *cations* (contrary to experimental observation in cements) in that the area available for anion diffusion is less than that for cations, that is $f_{-}^{\phi} < f_{+}^{\phi}$. The resolution to this paradox may lie in the different percolation paths to which cations and anions have access. Given any collection of connected pores, anion exclusion renders more paths accessible to cations than anions, but a number of these paths are necessarily "dead-end" or highly constricted paths in that they are only connected to the capillary porosity network via a highly constricted opening that can selectively exclude specific ions (e.g., Cl^-). In the transient case, the loss of cations to dead-end pores may lead to an apparent retardation of cations until the transport through the highly tortuous pathways also reaches steady state. It is possible that the one and two week durations of the through-diffusion tests of [88] and [87], respectively, were not long enough to capture the steady-state transport of cations through the highly-restricted diffusion regimes. In addition, a fraction of the cations in larger pores may be selectively diverted to more constricted pores prior to release to the downstream compartment of the diffusion cell, resulting in an apparent reduction in the net diffusion rate of cations relative to anions.

Another consequence of filtering effect of small connecting pores is that a fraction of pore water anions may be trapped within ink-bottle pores (Fig. 3.5b) as a consequence of initial cement hardening initially present in the material within ink-bottle pores may be only slowly leachable (more slowly than cations) due to the filtering effect of small connecting pores, that is, the macroscopic anion-specific tortuosity may be increased (i.e., a trapping effect occurring as a consequence of initial material formation, Fig. 3.5b). In such a situation, the degree to which anion transport from external sources appears more rapid relative to cations would depend largely on the proportion of ink-bottle pores within the system. For clays this proportion may be greatly influenced by the level of compaction [123] and therefore makes more difficult the interpretation of diffusion data in the absence of pore size distribution measurements. However, considering that, for the mortar presented, more than half of the pore volume measured by mercury intrusion can be attributed to ink-bottle pores, the effect of such filtering pores on overall diffusivity may be significant in this and analogous cementitious systems.

Furthermore, as shown in Figs. 3.4 and 3.6, the anion exclusion effect is magnified for pore solutions diluted by factors of 10 and 100, respectively.

Although the interpretation of the continuum-representation PBE should be interpreted with extreme caution in very dilute and transient systems, the trends from the solution of the PBE compare favorably with molecular dynamics simulations and density-functional theory simulations with decreasing ionic strength [124]. Thus, the PBE solution may give insight into expected behaviors of an "average" pore. One such insight is the enhancement of anion exclusion in dilute pores which is a very important result with respect to constituent leaching. As pores near the leaching boundary become more dilute, the coulombic forces resulting from the charged surface are exerted over a greater distance within those pores. Hence, a greater number of pores exhibit significantly altered charge ratios, and the likelihood that any percolating path contains one or more pores with significantly altered charge ratio necessarily increases. Thus, it is possible and indeed likely that these near-surface, depleted pores have a disproportionately large effect on the rate of constituent release.

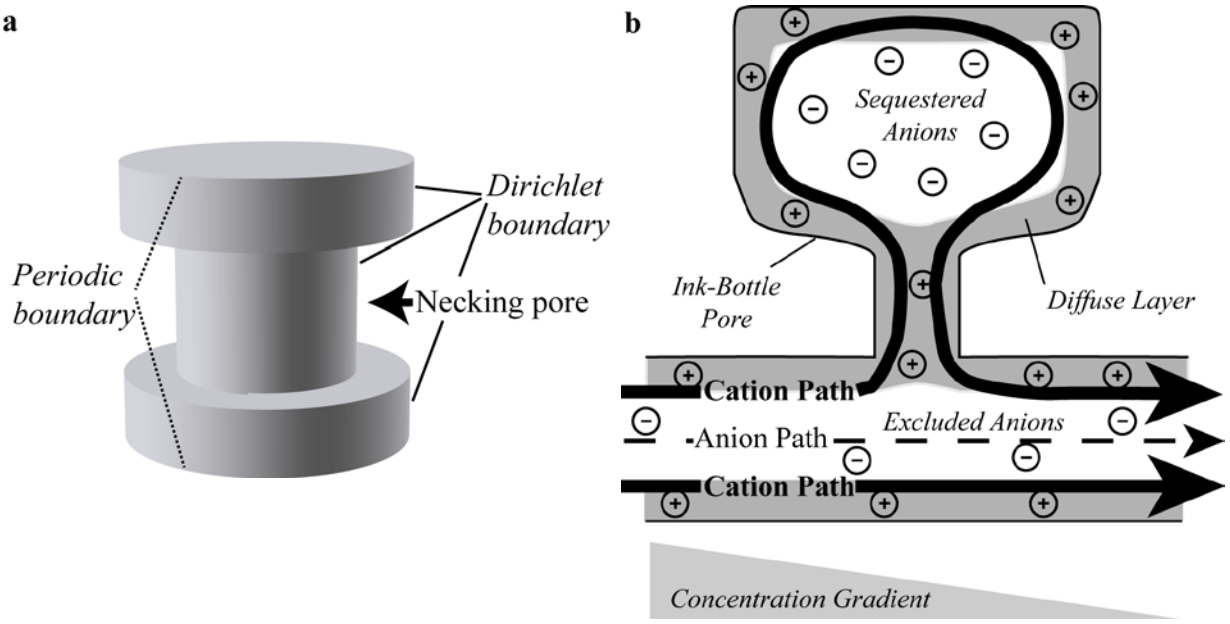

Figure 3.5: a) Depiction of the 3-d bottle-necking pore and delineation of the boundary conditions, and b) schematic indicating the more tortuous cation path and the local distribution of anions when considering ink-bottle pores.

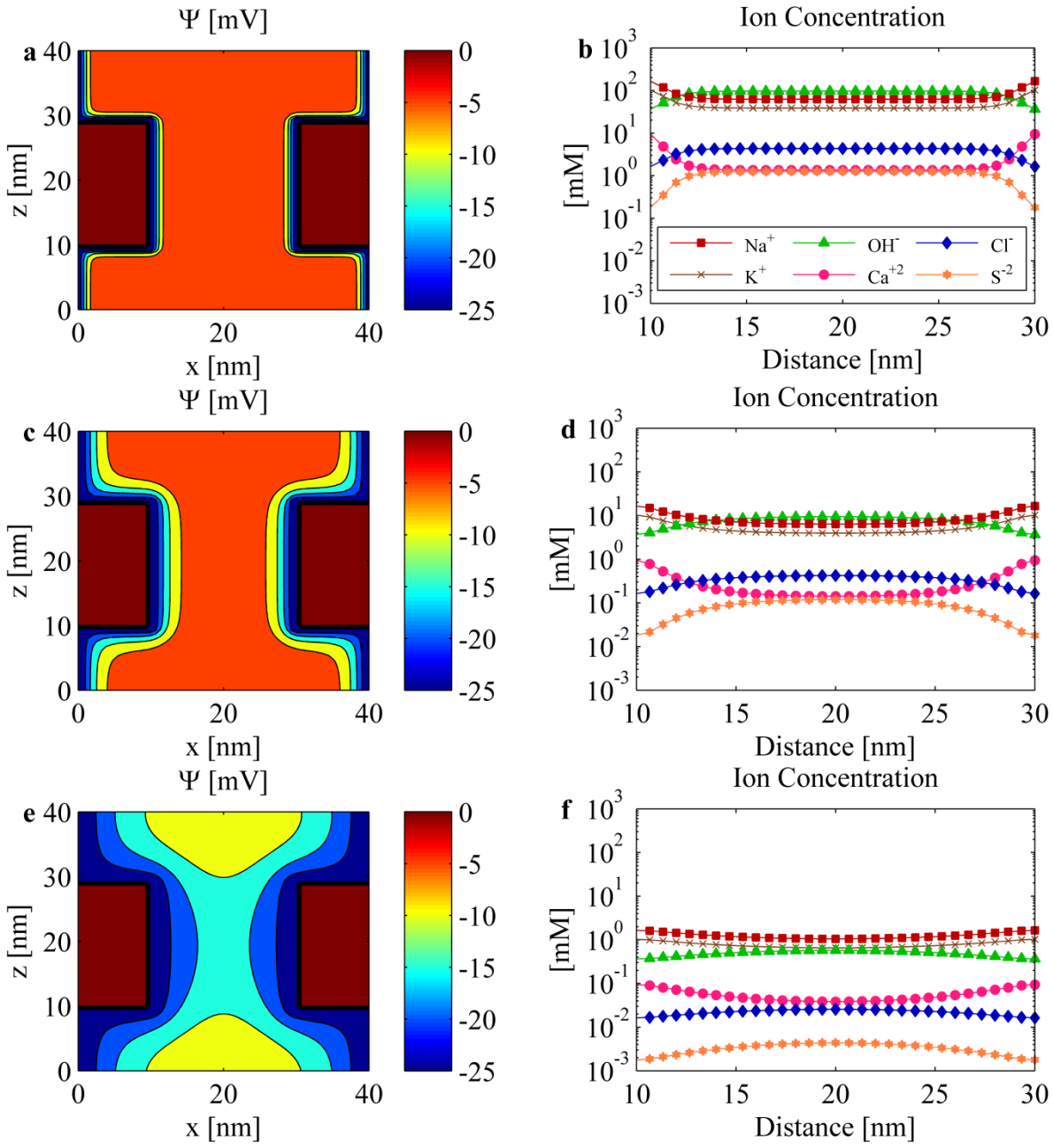

Figure 3.6: Electrostatic potential contour plots and concentration profiles for two cylindrical pores (40 nm diameter) connected by a bottle-neck pore (20 nm diameter). Potential profiles (left) and concentrations at z = 20 nm (right) are shown for the pore solution (a, b), a 10x diluted pore solution (c, d), and a 100x diluted pore solution (e, f).

3.5. Conclusions

A solution of the full nonlinear Poisson-Boltzmann equation for non-ideal aqueous solutions and highly charged surfaces was introduced. Discrepancies between the simplified linear solution and full nonlinear solution of as much as 50% were illustrated. Errors encountered from using the symmetric solution of the PBE were less pronounced, ranging up to 15% for the scenarios presented. The full nonlinear PBE solution was demonstrated for a real cementitious mortar with known pore water composition and pore size distribution. For the relevant pore sizes of the material, the effects of the EDL were found to alter mean ionic concentrations by at least 10% for approximately 10% of the total connected pore volume and by as much as 500% for pores less than 1.5 nm in diameter, resulting in a mean charge ratio for the interconnected porosity of approximately 1.10 [|+ charge / - charge|]. Assessment of the possible mechanisms of disparate cation and anion diffusivities suggest that anion-exclusion from poorly connected pore pathways could lead to an apparent lower diffusivity of cations. Due to the high volume of dead-end porosity within cementitious specimens, significant differences in anion diffusivity are anticipated depending on whether the anion source is initially present within the material or is introduced from an external source. Implicit in this assertion is the assumption that capillary pores determine the rate of transport through the material; however, the importance of the small (~1.5 nm) interlayer gel porosity and surficial phenomena cannot be immediately discounted *a priori*. In addition to Coulombic forces, the effects of ion-pore, ion-solvent, and ion-ion interactions become increasingly important with decreasing pore size. Therefore, further work invoking solution of the coupled Nernst-Planck Poisson-Boltzmann equation, molecular dynamics simulations, and more refined microstructural characterization of the pore space is necessary both to substantiate these claims and ultimately to develop mechanistic-based predictions of ionic diffusivity at the macroscale.

CHAPTER 4

4. BACKSCATTERED ELECTRON MICROSCOPY AND ENERGY DISPERSIVE X-RAY ANALYSIS FOR QUANTIFICATION OF THE REACTED FRACTIONS OF ANHYDROUS PARTICLES IN A BLENDED CEMENT MORTAR

Abstract

A novel technique is presented for the identification of unreacted binder particles in a blended cement mortar using backscattered scanning electron microscopy (BSEM) coupled with energy dispersive X-ray (EDX) analysis. Segmentation of unreacted particles from hydrate phases is achieved through nonparametric global thresholding of the backscattered electron (BSE) micrograph grayscale histogram coupled with fuzzy inference rules incorporating both textural and EDX information. Linear discriminant analysis (LDA) is then used to differentiate between particles according to elemental composition. Reacted fractions of anhydrous binder phases, used for the parameterization of chemical and physical properties of cement systems, are deduced from the difference between original and remaining area fractions of binder materials. After 30 months of curing, the Portland cement is found to be completely reacted, whereas approximately 83% of the slag and 36% of coal fly ash are reacted over that duration; these fractions are within the range of reacted fractions for similar materials reported in the literature.

4.1. Introduction

Supplementary cementitious materials (SCMs) have been employed extensively due to their ability to enhance mechanical performance and reduce permeability of grouts and concretes, while providing a beneficial use for industrial byproducts and lowering the carbon footprint of cement-based construction. A key parameter for describing the physical and chemical behaviors of cementitious materials is the rate at which binder materials are consumed as the cement evolves due to continued hydration and environmental aging [13]. For neat ordinary Portland cement (OPC) pastes, consumption of the majority of clinker mass occurs within the first month of hydration; however, the rate of reaction of SCMs may be orders of magnitude slower than that

of OPC. Thus, the physical and chemical behaviors of blended cement systems may at long times be governed by the continued rate of SCM reaction.

To this end, significant progress has been made toward quantifying the reacted fraction of SCMs in cementitious materials via segmentation of backscattered scanning electron (BSE) micrographs [125-128]. Because the frequency with which materials elastically scatter electrons depends upon the product of mean atomic number and density of the material, $Z_{ave}\rho$, these methods are able to distinguish between typically low- and high-density hydrous and anhydrous phases, respectively, using BSE micrograph grayscale intensity. Such quantification methods perform well for systems in which compositional differences between hydrous and anhydrous phases are sufficiently large; however, in systems containing two or more SCMs and/or aggregate materials [128], distinctions on the basis of BSE intensity become difficult if these anhydrous particles possess similar values of $Z_{ave}\rho$. This difficulty is realized for the material pertinent to the present study, a multi-component blended cement mortar containing ordinary Portland cement, coal combustion fly ash, ground granulated blast furnace slag, and fine aggregate, which is similar to the vault concretes used for radioactive high-level waste tanks [1, 129].

The objective of this work is the development of a method for identifying anhydrous particles on the basis of elemental composition obtained through energy dispersive X-ray spectroscopy (EDX) in conjunction with BSE microscopy. Previous methods for integrating BSE-EDX analysis into particle identification have incorporated a decision tree analysis technique, which entails defining heuristics for classifying particles based on major element concentrations [130, 131]. In highly heterogeneous materials, constructing such a decision tree may be impossible when distinct materials exhibit sufficiently similar compositions. The method used in the present study differs significantly from previous approaches. First, rather than considering EDX information pixel by pixel, pixels are grouped into particle regions in a novel segmentation step that integrates BSE intensity, textural measures, and EDX spectra using fuzzy inference rules. Creating particle regions in this manner ensures both spatial and compositional correlation among the pixels in a given region. All pixels within the region are therefore assumed to be samples of a single underlying mean composition, which effectively increases the total number of X-ray counts, ergo precision, associated with a single composition measurement. Grouping

pixels in this manner also decreases the total number of computations required to classify all particles as compared to pixel-by-pixel classification.

The second major difference between the current approach to particle identification and its predecessors is that herein linear discriminant analysis (LDA) [132] is employed to classify individual regions, or particles, by comparing measured EDX compositions to a database of possible anhydrous phases. The anhydrous particle database is constructed from phases of well-known composition, for instance the alite, belite, aluminate, and ferrite phases in Portland cement. The slag and ash particles used in this study present a challenge, however, as no archetypes for these particles' compositions presently exist. Therefore, preparations of these unreacted particles have been measured using quantitative BSE-EDX analysis, and, to determine whether subtypes of each particle exist (analogous to the subtypes of Portland cement), a model-based clustering (MBC) algorithm [133] has been used to determine the optimal number of clusters, or subtypes, for separately describing the populations of ash and slag particles.

4.2. Materials and experimental methods

The blended cement mortar studied is composed of Type I/II Portland cement (OPC) [134], grade 100 ground granulated blast furnace slag (BFS) [135], Type F coal combustion fly ash (FAF) [136], and quartz sand (QS) [137]. Total elemental compositions for the major constituents of all four materials, as determined by X-ray fluorescence (XRF) spectroscopy (Arcadis, USA) are given in Table 4.1.

Table 4.1: Major element composition of the component materials as determined by XRF, in mass percent. Carbon (C) is reported as total carbon.

Binder	C	O	Na	Mg	Al	Si	S	K	Ca	Ti	Fe
BFS	---	38.17	0.13	6.88	3.46	17.06	0.82	0.35	23.75	.03	0.21
FAF	1.50	45.49	0.25	0.62	15.08	24.42	0.04	2.14	0.86	1.67	4.98
OPC	2.50	31.34	0.13	0.58	2.15	7.67	1.55	0.38	41.30	.03	2.70
QS	0.93	52.35	0.02	0.00	2.45	43.82	0.00	0.18	0.01	0.02	0.21

4.2.1. Sample preparation

Samples of both the component SCM materials, BFS and FAF, and of the blended mortar were prepared for BSE-EDX analysis. Approximately 20g of BFS and FAF powders were first oven dried at 65°C for 48 hours to remove any residual moisture, then immersed in low-viscosity methacrylate resin. The powder-resin mixtures were held under vacuum for one hour in order to displace any air pockets with the samples.

Blended mortar samples (denoted SVC) were prepared by mixing OPC, BFS, FAF, and QS in the proportions listed in Table 4.2; this formulation is within the family of compositions used as structural concretes in nuclear waste management applications, with the exception that no coarse aggregate is present in SVC [1]. SVC samples were cast as slabs measuring approximately 15 cm width × 30 cm length × 5 cm height. Slabs were unmolded 24 hours after casting and were cured at 98% relative humidity and 298K for 30 months in a nitrogen atmosphere. Following curing, cylinders were cored from the slabs using a low-speed, diamond-embedded drill bit. Disks were then sawn at low speed from the interior portion of the specimen to avoid sampling from molded surfaces.

Table 4.2: Mix design of the blended cement mortar studied herein. Particle sizes were determined from information provided by [138].

Component	Specific Gravity	Mean Particle Diameter [μm]	Median Particle Diameter [μm]	Mass %	Vol. %
BFS	2.89	3.87	8.12	8.0	5.8
FAF	2.33	6.02	14.90	16.9	15.1
OPC	3.01	4.16	11.30	5.40	6.0
QS	2.54	590.6	596.45	55.0	45.0
Water	1.00	-	-	14.6	30.4

After coring and sawing, reaction was arrested by immersing the SVC disks in 99.5% reagent grade ethanol for two weeks to allow for complete exchange of accessible pore water with ethanol. Alcohol-exchanged samples were then immersed in a low-viscosity methacrylate resin for an additional two weeks to allow for displacement of the ethanol by resin.

Resin-immersed samples of FAF, BFS, and SVC were hardened with a 24-hour cure at 65° C under anoxic conditions. Samples infused with hardened resin were mechanically ground using a sequence of 240 and 600 grit silicon carbide papers, cleaning the sample surface with ethanol after each grinding sequence to remove any loosened debris. The samples were then mechanically polished using two separate alcohol-based suspensions of diamond particles possessing both 6 μm and 1 μm nominal diameters. After the final polishing step, samples were sonicated in acetone for 20 seconds to remove any remaining debris. Samples were then evaporatively coated with approximately 15 nm of graphitic carbon.

4.2.2. Scanning and processing

All scans were performed using a Phillips/FEI Quanta 650 field emission electron microscope under high vacuum at 10 keV accelerating voltage and a nominal 3.5 spot size, the parameter governing the diameter of the electron beam. BSE micrographs were obtained using the 4 quadrant solid-state BSED backscatter detector, and EDX spectra were collected using the Oxford X-Max 50 mm^2 Si(Li) X-ray detector. All BSE and EDX analyses were performed at a working distance of 10 mm with the horizontal field of view width (HFW) set to 256 μm (Polaroid magnification of 496x). EDX composition maps across the entire field of view were collected with a pixel resolution of 256 x 224 such that the pixel edge length equaled 1 μm. For each EDX map acquisition, 2000 raster frames were collected, each with a pixel dwell time set to 100 μs. The HFW was chosen as a compromise between the ability to resolve small features and the time demand of collecting a representative number of samples. Furthermore, as will be discussed in the next section, the resolution of the electron beam itself is on the order of 1 μm. The sampling strategy itself was also impacted by the presence of sand particles because picking a random sampling point on the specimen surface frequently resulted in a sand particle covering the entire field of view. Executing a full EDX analysis for a sand particle does not provide any information as to the hydration of the cement, slag, and ash particles; therefore, sampling points were chosen using a Latin hypercube sampling of the unit disk [139] and then shifted to the nearest non-sand area to maximize sampling efficiency. In total, 12 preparations each of BFS and FAF particles and 12 preparations of SVC monoliths were analyzed.

4.2.3. Sources of experimental uncertainty

In addition to the usual uncertainties associated with experimental measurements, such as accuracy of calibration and variation of experimental conditions, a few sources of uncertainty specific to BSE-EDX analysis warrant further discussion here. The extent to which useful compositional information may be gleaned from a BSE micrograph is limited by the topographic variation of the specimen surface, which may give rise to darker and lighter regions that obscure the underlying compositionally-dependent backscattering efficiency of the material. Such variations are observable in the BSE micrographs of the mechanically polished SVC because of the variation in hardness among the sand, hydrates, and anhydrous particles. Small (2002) demonstrated the magnitudes of topographic errors across a range of accelerating voltages using spherical analytical glass standards; measurements on resin-mounted and polished glass shards reveal a relative error in mass fraction measurement on the order of 10% with an excitation voltage of 10 keV to values between 25 and 60% with an excitation voltage of 25 keV. Therefore, given the 10 keV excitation voltage used in this study, the errors associated with topographic variation are expected to be small.

An essential component of the quantitative analysis of heterogeneous materials is delineating the region from which the signal originates. Although electron microscopes are capable of producing an electron beam on the order of nanometers in width, the volume in which electron collisions occur, that is, the *interaction volume*, is considerably larger in most materials. For high-vacuum SEM, Kanaya and Okayama [140] derived a semi-empirical expression for the depth of interaction volume in pure materials, d_{KO} [μm], that is directly proportional to the excitation voltage of the electron beam E_0 [keV] and inversely proportional to atomic number, Z, and to the mole density, ρ/A:

$$d_{KO} = \frac{0.0276 A E_0^{5/3}}{Z^{8/9}\rho}, \tag{4.1}$$

where A is atomic mass [g/mol] and ρ is the density of the medium [g/cm^3]. The exponential dependence of d_{KO} on accelerating voltage suggests that E_0 should be minimized; however, the optimal value of E_0 is constrained by the requirement for sufficient BSE compositional contrast and sufficient X-ray generation rates. For the carbon-coated samples used in this study, an excitation voltage of 10 keV was found to yield good peak separation in the BSE grayscale

histogram and near the recommended X-ray collection rate (approximately 3000 counts per second for the Oxford X-Max 50 detector). Whereas Eq. (4.1) provides an indication of size of interaction volume for pure elements, a more rigorous characterization can be achieved by simulating the flight paths of incident electrons, wherein the probabilities of elastic and inelastic scattering are governed by effective atomic cross-sectional areas [141]. Using Monte Carlo simulations of electron trajectories in cementitious targets, Wong and Buenfeld [142] estimated the interaction volume in ettringite to be on the order of 1-100 μm^3 for E_0 ranging from 10-20 keV. Considering that the densities of the anhydrous particles in this study are greater than that of ettringite, a 1 μm diameter of the interaction volume may be treated as a conservatively large estimate for all anhydrous particles of interest herein.

The importance of estimating the interaction volume is due to the effect of partial volume averaging (PVA). PVA occurs when the observable interaction volume, herein referred to as the "probe" volume, is greater than the volume of the feature of interest, and in the case of particles embedded in a resin medium, the sum of elemental mass fractions probed by the electron beam, neglecting the contribution from the resin, is necessarily less than unity. In such situations, renormalization of the mass fractions may be appropriate, but in scenarios in which a particle is interspersed within a medium of comparable composition, for instance anhydrous particles within C-S-H, PVA may lead to a locally measured composition that is characteristic of neither the particle nor the medium. Moreover, the extent of the interaction volume will be greater in the direction of the phase with lower mean Z due to the lower occurrence of electron scattering events. Consequently, the fraction of pixels near a feature boundary will determine whether a feature's composition can be accurately measured; features smaller than the interaction volume cannot be probed in isolation; whereas, the mean composition of very large features is relatively insensitive to PVA of the boundary pixels. Therefore, the likelihood of misclassifying particles smaller than the interaction volume may be high, and it is necessary to estimate the proportion of these particles relative to the entire population.

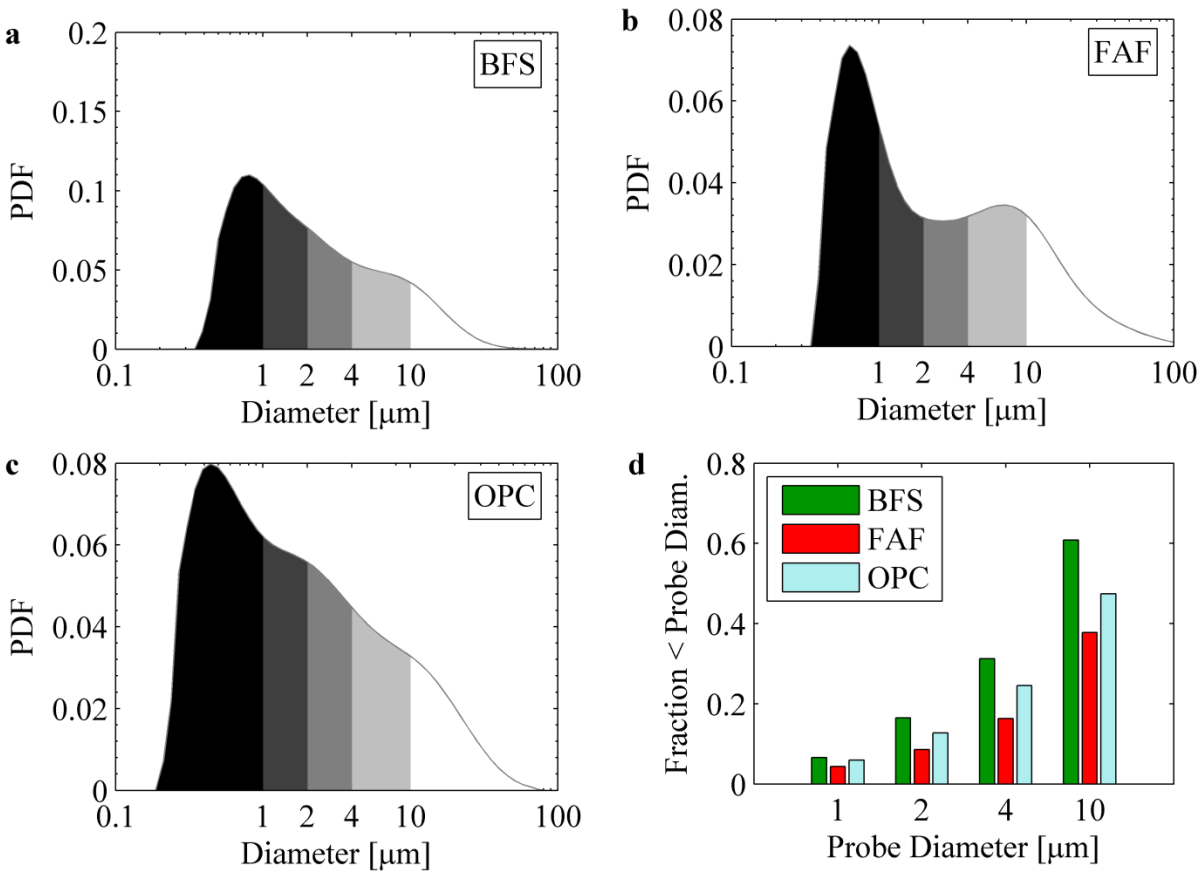

Figure 4.1: a, b, and c) Probability density function representation of particle size (diameter) distributions for BFS, FAF, and OPC particles, respectively, as measured by laser diffraction of particles suspended in propan-2-ol [138]. Darker regions of each histogram to the left of the diameter on the x-axis indicate the fraction of particles smaller than the nominal probe diameter at the corresponding value. Note that the abscissa is presented on the logarithmic scale. d) Summary of the probability that a particle is smaller than the nominal probe diameter.

With an estimate of the approximate diameter of the interaction volume, the fractions of anhydrous particles smaller than the probe volume (and necessarily partial-volume averaged) may be calculated from particle size distributions of the isolated, unreacted binder particles measured via laser diffraction [138]. For the BFS, FAF, and OPC particles used this study, Figs. 4.1a - 4.1c illustrate the measured distribution of particle diameters, with shaded areas representing the fraction of particles with diameters less than or equal to the nominal probe diameters of 1, 2, 4, and 10 μm (marked on the abscissas). As noted in Table 4.2, the mean values of particle diameter are substantially lower than the medians for all three particles, and for all three particle types, the maximum of the probability density function lies below the 1 μm

threshold. Ostensibly, the large proportion of small BFS, FAF, and OPC particles would suggest that SEM-EDX analysis is ill-suited to characterizing these particles; however, as shown in Fig. 2.1d, particles less than 1 μm in diameter only comprise about 5 % of each unreacted material's population, and would be expected to comprise a much smaller fraction of the material's population after reaction. Thus, PVA is not deemed to be a significant source of error in estimating the area fractions of remaining unreacted particles within the SVC mortar.

4.3. Particle identification method

Image analysis and data processing were performed using the Matlab computing environment (MATLAB 8.1.0.604, The MathWorks, Natick, MA). Section 3.1 outlines the process of particle identification which consists of two parts, beginning with the isolation of "anhydrous" particle regions in a segmentation step. A binary image consisting of anhydrous and non-anhydrous parts is constructed from the segmented image, and individual anhydrous particles are then defined as contiguous pixels within the binary region. Defining particles in this manner ensures *a priori* correlation in both spatial proximity and in compositional contrast; however, the reason for pixel grouping is twofold: considering groups of pixels not only increases the number of X-ray counts associated with a particle, thereby lowering the variance for a given measurement, but also reduces the number of computations required in the classification step. The second step of the process entails the identification of each region by comparing each particle's composition to a reference particle composition database. Unfortunately, no such database currently exists for the anhydrous particles of interest, so in Section 3.2, a database is created from measurements of the elemental compositions of isolated, unreacted BFS and FAF particles using BSE-EDX analysis. Section 3.3 gives the details of how particles are compared to the database using the discriminant analysis classification technique. Fig. 4.2 provides an overview of the data flow through the overall classification strategy.

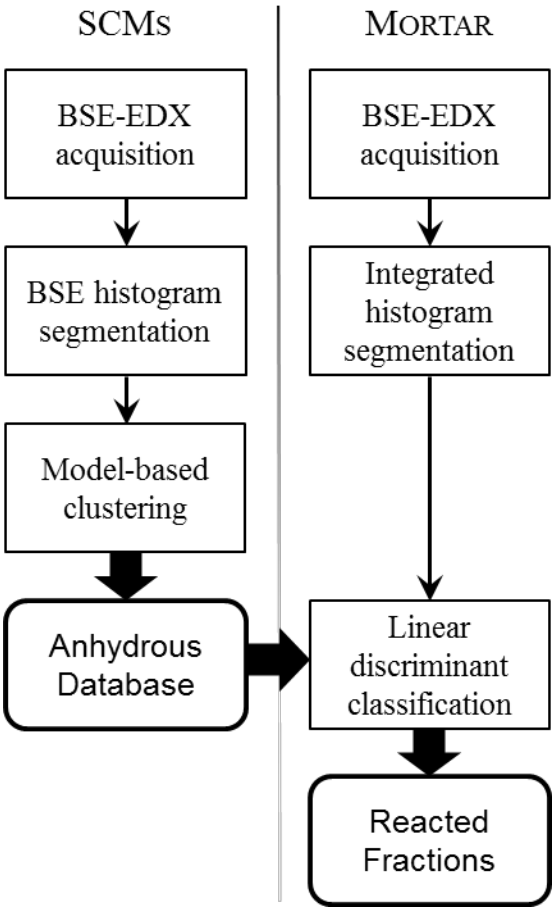

Figure 4.2: Data flow diagram of particle identification algorithm implemented in this work. The path designated “SCMs” describes the process for building the anhydrous particle database for subtypes of the binder materials. The path designated “Mortar” describes the process for comparing anhydrous regions identified in the hydrated SVC material to the anhydrous particle database in order to classify the anhydrous regions.

4.3.1. Segmentation

As indicated in Fig. 4.2, the segmentation procedure of SCM BSE monographs is distinct from that of the mortar segmentation procedure, but both methods make use of the nonparametric histogram segmentation procedure of Delon et al. [143], which shall hereafter be referred to as DDLP (Delon, Desolneuw, Lisani, Petro). Since DDLP is used extensively in this work and has apparently not been applied to cementitious BSE monographs previously, it is briefly outlined next.

Generalized nonparametric histogram segmentation: DDLP does not require an assumption of the number, relative fraction, or distribution type of each underlying class. Rather, each class need only be unimodal, that is, increasing then decreasing over an interval. For any given discrete histogram with frequency h defined on the discretized domain $[0, L]$, the set of image thresholds $S \in [0, L]$ with indices $n \in [1, N_S]$ is initially defined as all the local minima of h, including $h(0)$ and $h(L)$. According to DDLP a candidate threshold $S(n)$ is chosen at random; in this work, however, $S(n)$ is chosen as the threshold for which the variance of the interval $h([S(n-1), S(n+1)])$ is a minimum for all possible values of n, so as to render the method reproducible. The interval is said to be unimodal if there exists a trial threshold bin $t \in \big(S(n-1), S(n+1)\big)$ for which no significant rejection of the unimodal hypothesis exists, and the unimodal hypothesis is essentially that the values in $h(a, t)$ are increasing and the values in $h(t+1, b)$ are decreasing. For each trial t, the Grenander estimator is constructed using the "pool adjacent violators" algorithm (PAVA) for which the algorithm is provided in Appendix A [144]. The PAVA constructs a monotonically nondecreasing estimator of the histogram interval $h(a, t)$, or, conversely, the monotonically nonincreasing estimator of $h(t+1, b)$. An example of the Grenander estimator for a typical histogram segment is illustrated in Fig. 4.3a. If the subinterval $h(a, b)$ is deemed to be unimodal, the threshold $S(n)$ is removed from the set of S and the process is repeated until no more thresholds can be removed, or equivalently, until no two adjacent segments of h can be joined. The entire process is then repeated by testing for unimodality of 3, 4 … N_S adjacent segments. The output of the DDLP algorithm is the set T of all thresholds identified for h.

SCM segmentation procedure: The efficiency with which electrons are elastically scattered by a given element is described by the backscatter coefficient η for that element and the backscattering efficiency ε_{BS} [-] which varies with both electron beam energy and atomic number Z [145]. Thus, composition-dependent information is manifest within the BSE grayscale intensity histogram and provides a semi-quantitative basis for discriminating between resin and particle in the case of BFS, FAF, and OPC, and between resin, "hydrous", and "anhydrous" segments in the case of the SVC mortar [125, 146]. The terms "hydrous" and "anhydrous" here denote only a general distinction which relies on the fact that cement hydration products

typically possess lower densities and more low-Z water molecules than their corresponding clinker/binder materials. Thus, hydration products often, though not necessarily, have lower composite η as compared to the clinker/binder anhydrous particles.

If BSE contrast is sufficiently distinct, then subpopulations, or classes, of similar $Z_{ave}\rho$ may be ascertained through inspection of the frequency histogram h of all pixel BSE intensity values within a monograph. As illustrated in Figs. 4.3b, the anhydrous FAF are easily distinguished from the much darker methacrylate resin background. When applied to the BSE grayscale histogram of Fig. 4b, the DDLP algorithm yields intuitively satisfactory thresholds, as shown in Fig. 4.3c. Note that the very bright regions in Fig. 4.3b have been identified as a segment distinct from the bulk of the FAF particles, despite the fact that the area fraction of these bright pixels is quite small; histogram techniques that rely on measures of inter- and intra-class variance, such as the well-known Otsu's method [147], are generally insensitive to such small sub-populations. Shown in Fig. 4.3d is the monograph from Fig. 4.3b with the original grayscale intensities mapped to the segments established in Fig. 4.3c. For the purposes of building the anhydrous particle database, only the primary threshold, that is, the separator of resin and particles, was retained such that the resulting segmented image was binary.

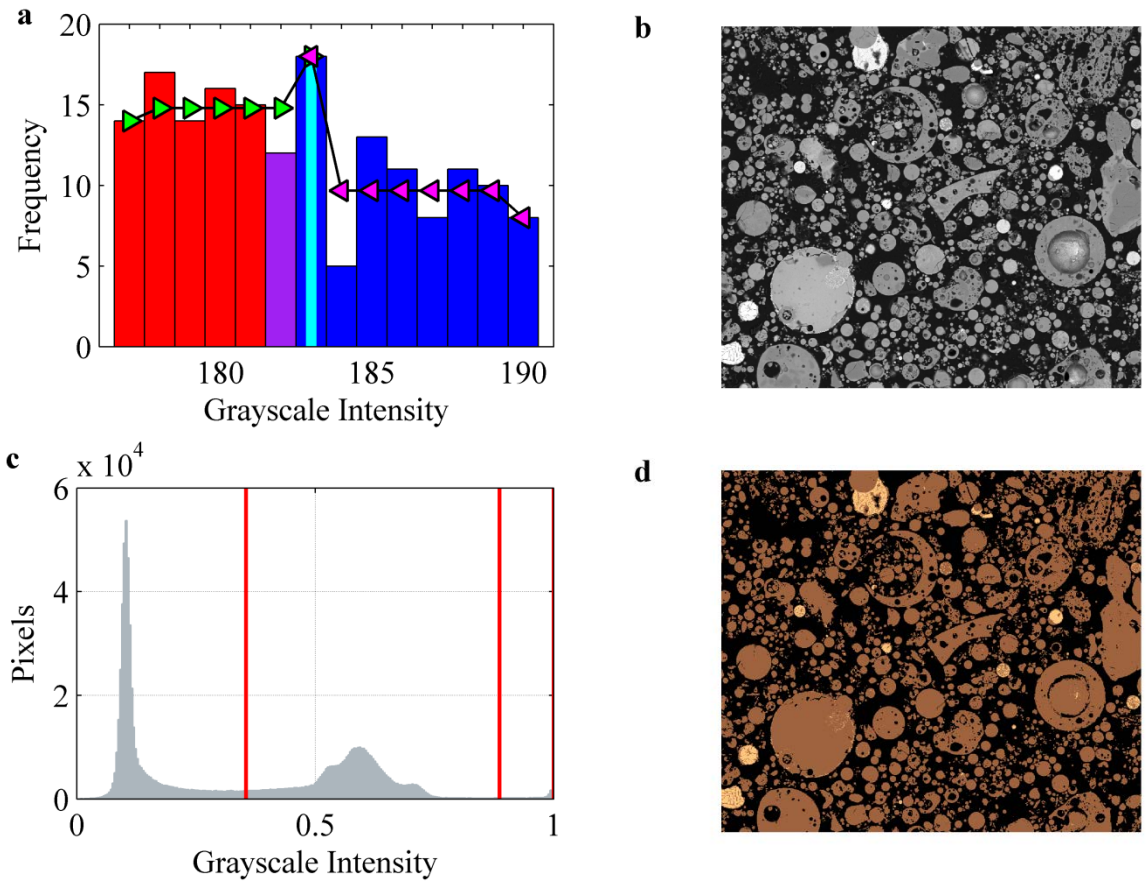

Figure 4.3: a) An example of the Grenander estimator constructed for a union of two histogram segments (red and blue bars, purple indicates the overlapping segment). The increasing estimator is designated with the right-pointing green triangles, and the decreasing estimator with left-pointing magenta triangles. The test interval is marked with a vertical stripe (cyan). b) A backscattered electron image of FAF particles mounted in acrylic resin. c) Histogram of BSE intensity values of the image in b) with red lines indicated the thresholds determined by DDLP. d) The segmented BSE monograph from b) using the thresholds defined in c).

Mortar segmentation procedure: For the SVC material, differences in grayscale intensity alone proved insufficient to segment the hydrous and anhydrous phases; quite commonly, the fine aggregate particles used in this study exhibit lower backscatter intensities than the gel phase. For such a highly heterogeneous material in both scale and composition, most general strategies, such as global histogram segmentation, fail to yield meaningful results. Therefore, the goal of the segmentation algorithm developed in this work is to “divide and conquer”. Using both BSE intensity and textural information and EDX spectral information, the most easily segmented

regions are first identified and then removed from subsequent analysis so that the quantities being analyzed at each step belong only to the remaining unclassified pixels.

The segmentation algorithm begins by enhancing features in the BSE intensity image I using a smoothing filter based on the 2D diffusion equation, first proposed in [148]. Denoting the grayscale intensity at the point (i, j) as $I_{i,j}$, the smoothed image at iteration step $k + 1$ is given by the forward Euler finite difference approximation of the 2D diffusion equation

$$I_{i,j}^{k+1} = I_{i,j}^{k} + \beta \sum_{D} \left(c_D \nabla_D I_{i,j}^{k} \right) \tag{4.2}$$

where β is a parameter equal to $1/7$ for numerical stability of the explicit finite difference scheme and D denotes the direction of the finite difference gradient approximation, that is $D \in [North - South, East - West, NorthEast - SouthWest, SouthEast - NorthWest]$. The authors of the original algorithm referred to the filtering scheme as "anisotropic" diffusion because the diffusion coefficients c_D depend directly upon the magnitude of the gradient in image intensity at the previous timestep. For this work, c_D have a Gaussian-type functional form proposed in [148] given by

$$c_{D_{i,j}}^{k} = g\left(\left| \nabla_D I_{i,j}^{k} \right| \right) = \exp\left(- \left(\frac{\left\| \nabla_D I_{i,j}^{k} \right\|}{W} \right)^2 \right). \tag{4.3}$$

Thus, the effect of this scheme is to smooth most in the direction of the gradient where gradients are strongest and to smooth very little along contours such as edges. The total number of time levels and the parameter W are adjustable scaling parameters in time and space, respectively, which have been set to 50 and 0.05 at the authors' discretion. Using Eqs. (4.2) and (4.3), the intensity image I is smoothed and normalized to the interval $[0,1]$ to yield the matrix I^* that generally exhibits a histogram with more pronounced separations of peaks. The DDLP algorithm is applied to the histogram of I^* to yield a set of N preliminary threshold values S_I which are used to create a segmented map, I_L^*, of $N - 1$ levels L.

The difficulty with treating I_L^* as the final segmented map is that in the 30 month cured mortar studied herein, areas of the gel phase exhibit a very high BSE intensity. In order to distinguish between these areas and anhydrous particles, the disordered nature of the gel phase is exploited; the gel's lack of ordered structure on the micrometer scale leads to a high variation in local

values of I. Thus, the Gaussian smoothed gradients G_x and G_y of I^* are computed in the x and y dimensions, and the classical texture metric G is defined as

$$G = \left\| G_x + G_y \right\|. \tag{4.4}$$

With textural information in hand, the next step in the segmentation procedure is to march through the levels of I_S^* and examine whether the pixels belonging to each level are high gradient or low gradient areas. For this purpose, the DDLP algorithm is employed once again, but because G is a measure of the change in approximately Gaussian variables, it is necessary to perform DDLP on the histogram of the natural logarithm $\Gamma = \ln(G)$. The histograms of Γ computed are used to compute the set $S_\Gamma(\ell)$ of thresholds for each level ℓ:

$$S_\Gamma(\ell) = \mathrm{DDLP}\big(\Gamma \otimes H(I_L^* = \ell)\big), \qquad \ell \in L \tag{4.5}$$

where $H(\cdot)$ denotes the element-wise Heaviside function, that is

$$H(x) = \begin{cases} 0, x < 0 \\ 1, x \geq 0 \end{cases} \tag{4.6}$$

and $\otimes$ denotes element-wise multiplication. Almost invariably, the histograms of Γ for each level are strongly bimodal, such that $S_\Gamma(\ell)$ contains three members per level, and the primary threshold $t_\Gamma(\ell)$ is simply the median value of the set $S_\Gamma(\ell)$. Proceeding from the brightest level in I_L^*, a binary map of anhydrous particles with low gradient values, B_{map}, is constructed recursively as

$$B_{map} = B_{map} \cup H\big(\Gamma < t_\Gamma(\ell)\big) \otimes H(I_L^* = \ell), \tag{4.7}$$

and the recursion is ceased at the level ℓ for which the mean of $\big(I_L^* \otimes H(I_L^* = \ell)\big)$ is closest to the global mean of I_L^*.

The segmentation procedure given above uses only BSE intensity information and knowledge of basic cementitious material properties, and is, therefore, expected to be generally applicable to a number of cementitious materials. For the SVC mortar, however, two particles present in the fine aggregate fraction are particularly problematic for the above algorithm; quartz sand particles and kaolinite particles exhibit backscattering properties similar to those of the gel phase and are prone to being omitted from the segmentation. Fortunately quartz contains a much higher percentage of Si, 47% by mass, than any other anhydrous particle considered herein. In practice,

the lower bound that encompassed the variability about the Si measurement in quartz proved to be approximately 40% by mass. Therefore, the segmentation of the quartz particles is effectively achieved through a simple heuristic relationship

$$QS_{map} \equiv H(Si_X - 40.0\ mass\ \%) \tag{4.8}$$

Si_X is the matrix of measured Si EDX mass percentages, and QS_{map} is the resultant binary map of pixels deemed to be quartz.

Kaolinite ($Al_2Si_2O_5(OH)_4$) is a phyllosilicate which is a common secondary mineral in soil environments and is found in the fine aggregate fraction of SVC. More commonly, illite is observed in the fine aggregate fraction, but the inclusion of higher atomic weight potassium in illite generally leads to a strong BSE response which facilitates its segmentation by BSE intensity alone. Kaolinite, like quartz, is poor at backscattering electrons such that the observed intensity for kaolinite is roughly on par with that of the gel phase. To address this problem, a mapping function K_{fuzz} is constructed, which may be regarded as representing a fuzzy inference [149]. K_{fuzz} is defined as the product of two generalized Cauchy or bell membership distributions centered about the theoretical composition of kaolinite, that is

$$K_{fuzz} = \left(1 + \left|\frac{(Al_X - 20.90)}{a_1}\right|^{2b_1}\right)^{-1} \left(1 + \left|\frac{(Si_X - 21.76)}{a_2}\right|^{2b_2}\right)^{-1} \tag{4.9}$$

where Al_X and Si_X denote the matrix of measured Al and Si EDX mass percent values, respectively. In this context, K_{fuzz} may be interpreted as the fuzzy inference "the region is kaolinite". The factors a and b in Eq. (4.4) control the spread and steepness of the "bell" of K_{fuzz}, respectively, and values of $a_1 = a_2 = 8$ and $b_1 = b_2 = 10$ yielded a reasonable estimate of possible measured kaolinite compositions. The resulting histogram of K_{fuzz} is typically highly bimodal for fields of view that contain kaolinite; thus, a binary map of potential kaolinite locations is constructed as

$$K_{map} \equiv H\left(K_{fuzz} - \max\left(0.5, \text{median}\left(K_{fuzz}\right)\right)\right). \tag{4.10}$$

An important point is that, in this step, the accurate identification of kaolinite is not critical; rather, the aim is to label any large kaolinite-like regions as particles to be classified in subsequent steps.

The final binary phase segmentation map of anhydrous particles, is defined as the union of the three binary maps, that is,

$$AP_{map} \equiv B_{map} \cup QS_{map} \cup K_{map}. \tag{4.11}$$

4.3.2. Anhydrous particle database – cluster analysis

The inherent variability of both the source material and the formation conditions of slags and fly ashes necessitates a definition of "representative" compositions for the specific types of both materials used in the cementitious material studied. Whereas the mean compositions listed in Table 4.1 are descriptive of the entire population of BFS and FAF particles, the population may very well be comprised of individual subpopulations, none of which possess compositions that are well-described by the mean composition. Cluster analysis provides a method of defining natural compositional divisions within a population, but classical clustering algorithms such as k-means or fuzzy c-means algorithms are limited by the requirement of an *a priori* definition of the number of clusters. Fraley and Raftery [133] addressed this problem using a technique they termed "model-based" clustering (MBC), which has been employed extensively, and a summary of their work will only be briefly discussed here.

The Gaussian mixture model gives the probability density φ_k of observing composition y_i given the multivariate mean μ_k and covariance Σ_k of class k:

$$\varphi_k(y_i|\mu_k, \Sigma_k) = \frac{1}{(2\pi|\Sigma_k|)^{1/2}} \exp\left(-\frac{1}{2}(x-\mu_k)^T {\Sigma_k}^{-1}(x-\mu_k)\right). \tag{4.12}$$

The core concept of the MBC methodology is that different characteristics of the distribution φ_k in d-dimensional parameter space may be described through the eigenvalue decomposition of the covariance matrix [150, 151]

$$\Sigma_k = \lambda_k V_k A_k V_k^T, \tag{4.13}$$

where A_k is a diagonal matrix governing the shape, V_k is the matrix of eigenvectors which determine orientation, and $\lambda_k$is a scalar governing the volume of ϕ_k. The MBC algorithm starts by choosing a maximum number of clusters and the models of the covariance structure to consider; different models are achieved by limiting the degrees of freedom in Eq. (4.14) [152].

The next step is to perform hierarchical agglomerative clustering (HAC) [153] of observations $x = (x_i, \ldots, x_n)$ under the assumption that Σ_k is unconstrained; that is, all degrees of freedom in Eq. (4.14) are considered, in order to maximize the likelihood function. At each point in the HAC step, clusters are merged according to the likelihood criterion, which results in a partitioning of the data, the so-called "classification tree". From this partition, the entropy maximization algorithm [154] (EM) is performed, where, in the first step, the distribution parameters (in this case, the mean and variance) of each class k are estimated from the current partition, and in the second, a new class membership is computed using updated parameter estimates. The EM steps are performed iteratively until convergence is reached. EM is performed for each model independently, and the Bayesian information criterion [155] is then used to judge the best choice of covariance model and number of clusters. The MBC algorithm is available as a toolbox in the statistical computing environment R [152, 156] and as part of the EDA Matlab toolbox available from [157].

In practice, the MBC algorithm may yield clusters which represent noise in the data. These noise clusters are typically characterized by a total mass percent over all elements that is significantly less than 100%, whereas the EDX method is typically capable of resolving total mass percents to within a 2% tolerance [145]. Thus, any cluster for which the total mass was less than 90% was excluded from the database. Furthermore, a number of clusters exhibit similar compositions that are nearly indistinguishable in EDX analysis. Therefore, any two clusters which differed by less than 5% in any one element were merged into a single, averaged cluster.

4.3.3. Particle classification - discriminant analysis

The process of particle classification is in essence a comparison of the particle's composition to the anhydrous phase database and then classifying the region based on this comparison. Numerous methods exist for executing the classification step [158], which range in complexity from nearest neighbor classification to the construction of supervised learning algorithms such as neural networks. Linear discriminant analysis (LDA) [132] was chosen as the classification method for the present study due to its straightforward treatment of class membership. LDA begins with the assumption that the underlying distribution of observation x_i belonging to class k

is a multivariate Gaussian (Eq. 4.14). To implement LDA, a training data set is used to calculate the posterior probability $\hat{P}$ that x_i belongs to class k:

$$\hat{P}(k|x_i) = \frac{P(x_i|k)P(k)}{P(x_i)}, \tag{4.14}$$

P's are constructed from the training data by maximizing the between-class variance with respect to the in-class variance, which for LDA is achieved through solution of the generalized eigenvalue problem. Although suitable training data may be generated through the meticulous measurement of particles in isolation, this procedure is not only time-consuming but also limits possible classes to those particles which have been measured. Therefore, for each unknown particle to be identified, the class definitions are taken as the mean values for each class, and the class covariances are defined uniformly for every class as the measured covariance of the particle in question. Once the classification discriminants are known, the class $\hat{y}$ of a new observation is one which minimizes the expected classification cost $C(y|k)$, formally

$$\hat{y} = \underset{y = 1, \ldots, K}{\operatorname{argmin}} \sum_{k=1}^{K} \hat{P}(k|x)C(y|k). \tag{4.15}$$

Prior probabilities $P(k)$ were chosen to be uniform, that is, $P(k) = 1/K$, and the true misclassification cost was set to 0 if $y = k$ and 1 otherwise. LDA analysis is available as part of the statistics toolbox in Matlab.

4.3.4. Calculation of reacted fraction

Due to the sampling strategy used in collecting BSE-EDX data, the pixel areas of anhydrous BFS, FAF, and OPC computed by the segmentation-classification algorithm is normalized to the fraction of the field of view which was not identified as QS (quartz and phyllosilicates). Reacted fraction of a binder is then computed as the difference in the unreacted particle area fraction and the volume of the binder relative to the volume of QS specified in the mix design (Table 4.2). "QS" refers both to the quartz sand particles in the fine aggregate as well as concomitant illite and, to a lesser extent, kaolinite. Illite is, in reality, a class of non-expandable phyllosilicate minerals which may be envisaged as interstratified kaolinite and mica layers. Interstratification of mica may occur at the local scale such that illite may be considered a true mineral, but mica

layers may also be interspersed at coarser length scales such that the assemblage should be regarded instead as illite+mica [159]. The XRF analyses in Table 4.1 indicate a significant amount of aluminum present in the QS fraction, and assuming all aluminum in QS is borne in illitic forms, the volume and mass proportions of illite present are estimated to be approximately 12 % of the QS fraction, since the densities of illite, kaolinite, and quartz are all approximately 2600 kg/m^3.

4.4. Results and Discussion

4.4.1. Anhydrous particle database

Cluster analysis was performed for both BFS and FAF resin-imbedded particles using approximately 600 particles for each material. Only those elements present in quantities greater than one mass percent for at least one anhydrous material were considered in the clustering analysis: Mg, Al, Si, S, K, Ca and Fe. Before clustering, the mass percent measurements were normalized to the predominant element mass percent, which for BFS and FAF were Ca and Si, respectively.

Results of the MBC algorithm applied to BFS and FAF particle measurements are presented in Figs. 4.4 and 4.5, respectively; elemental mass fractions are plotted to scale as circles for ease of visual comparison; the distance between horizontal lines corresponds to a mass fraction of one. Note that oxygen was not used in the clustering analysis, but was computed from oxide stoichiometry after the clusters had been identified. As demonstrated in Fig. 4.4, a single class, denoted BFS_a, was found to be the best descriptor for the BFS particles using the MBC method, indicating that the composition of BFS particles can be considered essentially homogeneous. That the composition of slag particles appears to be homogeneous is plausible give the rapid quenching of the molten material after smelting. Also, plotted in Fig. 4.4 is the composition of BFS particles as measured by XRF (presented in Table 4.1). Very good agreement was found between the XRF and EDX measurement techniques for BFS particles.

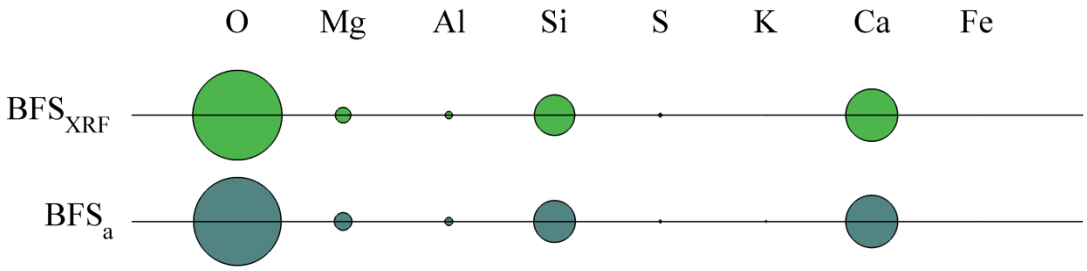

Figure 4.4: Diagram of mass fractions of BFS composition measured via XRF (BFS, presented in Table 4.1), and the centroid composition (BFS_a) as calculated by the MBC method applied to measured EDX compositions. The radius of each circle is scaled according to the mass fraction of each element, and the distance between horizontal lines corresponds to a mass fraction of one.

The class representation of FAF particles derived from the MBC algorithm are presented in Fig. 4.5. The FAF material is characterized by three basic types, distinguishable primarily by their content of Fe, with FAF_c most closely matching the the mean FAF composition.

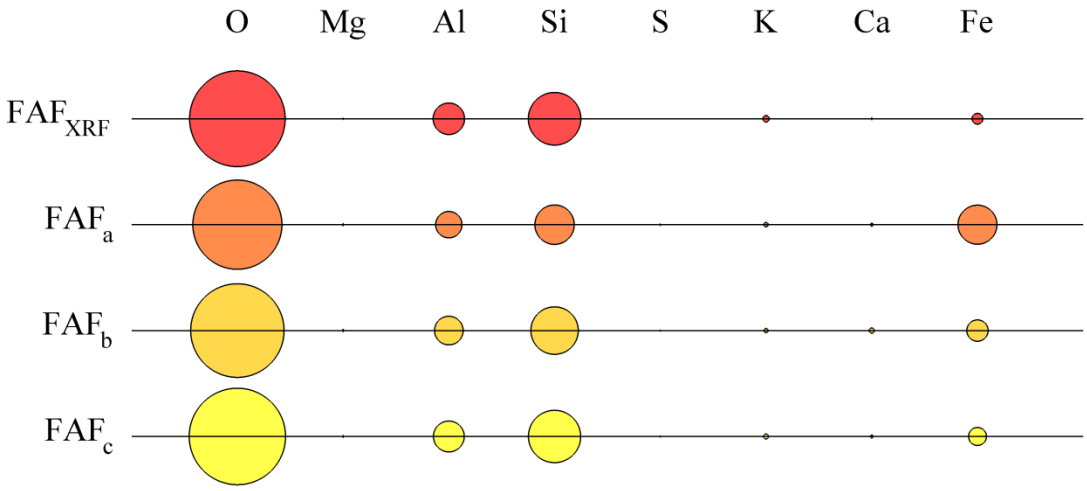

Figure 4.5: Diagram of the mass fractions of the bulk FAF composition (FAF), and the FAF subtypes ($FAF_{a,b,c}$) identified using the MBC method. The radius of each circle is scaled according to the mass fraction of each element, and the distance between horizontal lines corresponds to a mass fraction of one.

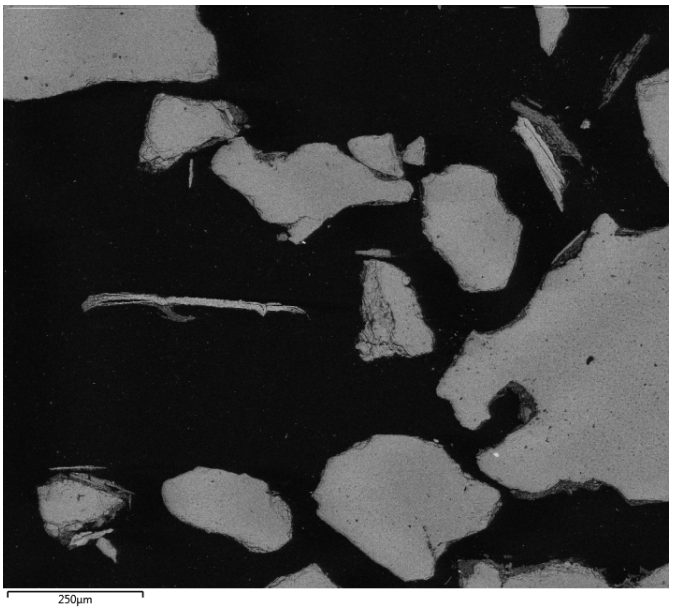

Figure 4.6: BSE micrograph of QS quartz sand aggregate with lath-shaped phyllosilicates.

Fig. 4.6 shows a BSE micrograph of the QS used in this study mounted in resin. The large particles in Fig. 4.6 are quartz particles, whereas the lath-shaped particles are thought to be illite and kaolinite. Based upon the illite unit cell [159], the empirical stoichiometry of the illite in this study observed from EDX analysis was estimated to be $(K_{0.67}Na_{0.21})(Mg_{0.10}Al_{2.44}Fe_{0.05})(Si_{3.40}Al_{0.60})O_{10}(OH)_2$. This illite composition is quite similar to the FAF_b class of particles, which is not a surprising result given that kaolinite and illite are two of the eight most abundant minerals found in U.S. coals [160]. These particles, however, are quite distinct from fly ash in their geometric eccentricity. The histogram of measured eccentricities of 75 phyllosilicate particles is plotted in Fig. 4.7.

The final phase included in the anhydrous particle database is mullite, an orthorhombic and relatively insoluble aluminosilicate found within fly ashes [161].

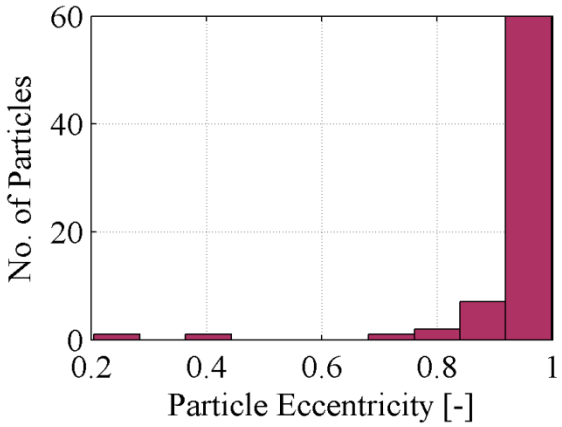

Figure 4.7: Measured distributions of particle eccentricities of the kaolinite and illite particles measured in the QS material.

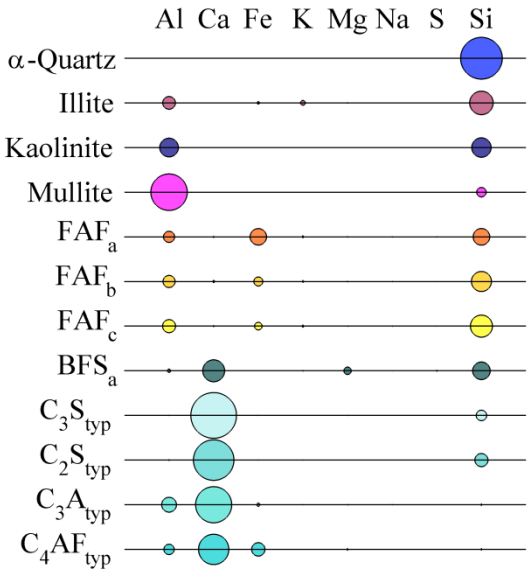

Figure 4.8: Diagram of the mass fractions of the anhydrous particle database used for particle classification. The radius of each circle is scaled to the mass fraction of the constituent in that column, and the distance between horizontal lines corresponds to a mass fraction of 1. The values of the cement clinker materials (C_3S_{typ}, C_2S_{typ}, C_3A_{typ}, C_4AF_{typ}) were not measured herein but instead correspond to typical values [162].

The entire anhydrous particle database is illustrated in Fig. 4.8 and numerical values are provided in Appendix E. The elements shown in Fig. 4.8 are a subset of the entire elemental composition; due to the curse of dimensionality, including those elements that only vary slightly across all

compositions renders classification more difficult. Oxygen was also not considered in particle classification due to the low accuracy of quantifying light elements.

4.4.2. Database cross-validation

To test the efficacy of the algorithm, LDA particle classification of was performed on both the unreacted BFS and FAF particles mounted in resin. Results of this classification for BFS are presented in Figs. 4.9 and 4.10, respectively. As shown in Fig. 4.9, LDA classification correctly identified approximately 97% of the BFS particles. Fig. 4.10 illustrates that the correct identification of BFS particles depends greatly on the particle size. This result is logical given that the estimation of a particle's mean composition improves with more samples of that composition. As shown in Fig. 4.9, a number of small particles are simply classified as none, which implies that these particles were, in fact, only one pixel in area so that a covariance matrix of their composition could not be constructed, and thus, the LDA algorithms was not applied to them. These particles account for the large number of misclassified particles with small area in Fig. 4.10.

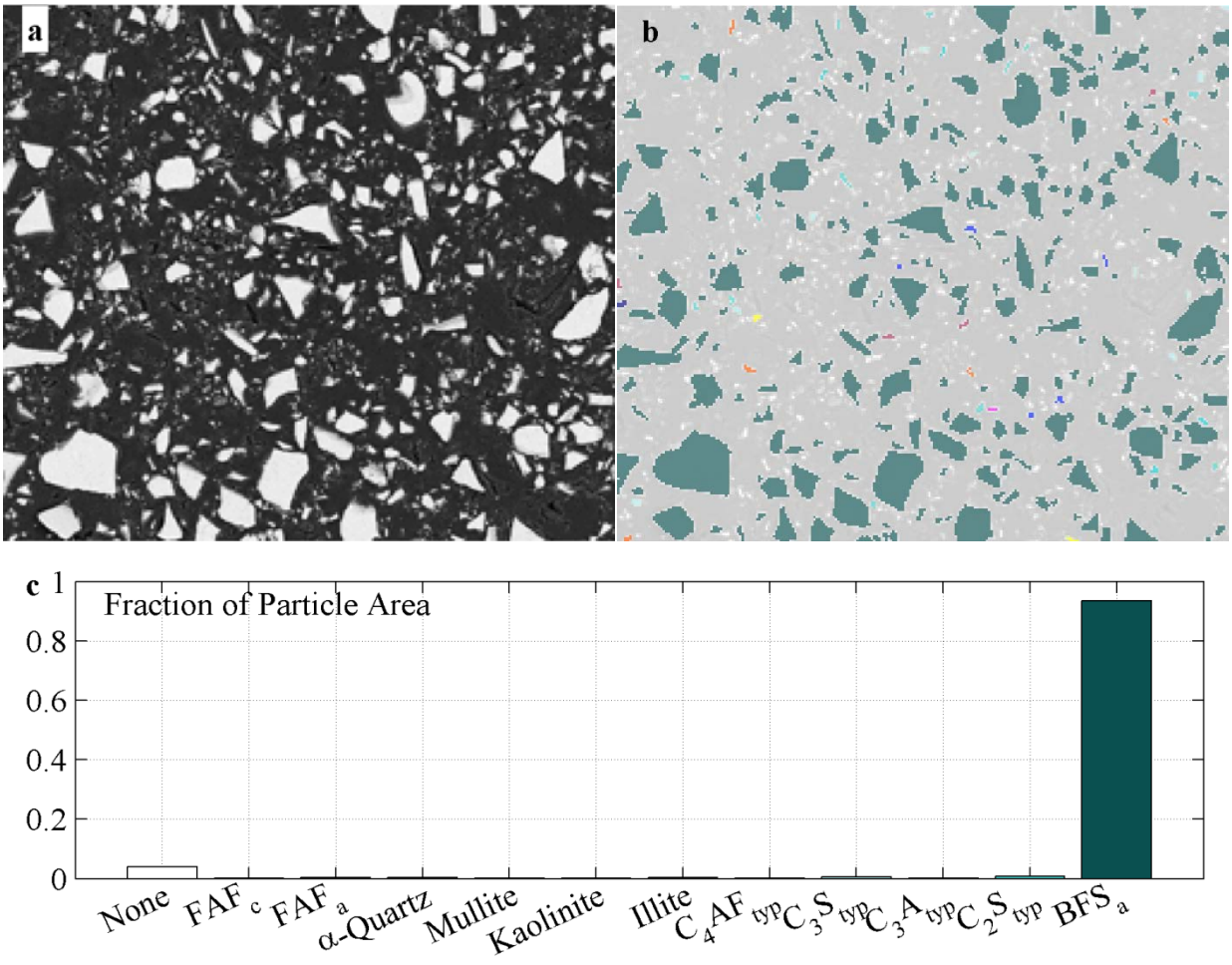

Figure 4.9: Results of the LDA classification algorithm applied to BFS particles mounted in resin. a) The original BSE micrograph of BFS particles, which appear white in the monograph. b) The BSE monograph overlain with each particle mapped with a unique color corresponding to the anhydrous database phases given in c. c) Bar graph illustrating the areas of each particle class identified. Those particles labeled “None” were not identified due to possessing too few particles to estimate the covariance matrix.

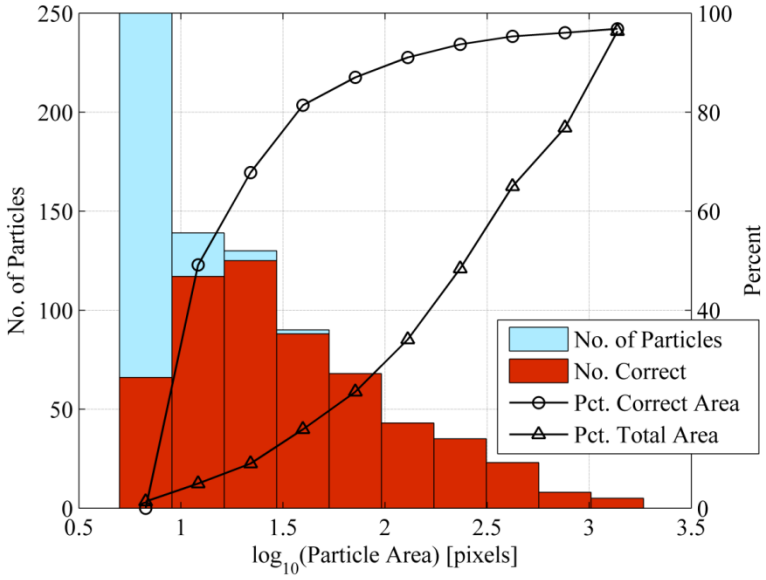

Figure 4.10: Area dependence of the LDA particle classification algorithm illustrated for BFS particles mounted in methacrylate resin. Particles are binned according to the base-10 logarithm of their area [pixels]. “Pct. Correct Area” indicates the area of particles correctly identified within a given bin per total area of particles within that bin. “Pct. Total Area” corresponds to the area contribution of all particles within a bin to the total area of the anhydrous BFS phase.

In Fig. 4.11, the results of the LDA algorithm applied to FAF are presented. The majority of particles identified are fly ash particles of type FAFc, with minor amounts of the higher Fe-content FAFa and FAFb subtypes identified. The algorithm also identifies a number of fly ash particles as quartz, illite, and kaolinite; quartz, along with mullite, is a refractory phase found in X-ray diffraction analyses [161]. As mentioned above, illite and kaolinite are two of the eight most abundant mineral phases found in U.S. coals [160], but these minerals are likely melted in the coal combustion process. Thus, the FAF particles are misidentified; however, these particles are quite dissimilar to fly ash in their appearance. To combat such misidentification, equivalent diameter and eccentricity have been included as auxiliary variables in the LDA analysis. Equivalent particle diameter is defined as the diameter of an ellipsoid with an equivalent first moment as a given region, and eccentricity is the ratio of the distance between foci of the ellipse to the length of its major axis. Using this strategy, LDA is first executed based on elemental composition alone; then, all particles identified as kaolinite, illite, and ash are reclassified considering elemental composition, eccentricity, and diameter. Although a seemingly high number of small particles are falsely identified as quartz, the quartz particles were not considered

in the geometric reclassification because, due to the sampling strategy, the quartz particles are almost always truncated at the boundary of the field of view, leading to unrealistic estimates of their particle size and eccentricities. The choice was made to misclassify a few small particles as quartz rather than to misclassify the large quartz particles.

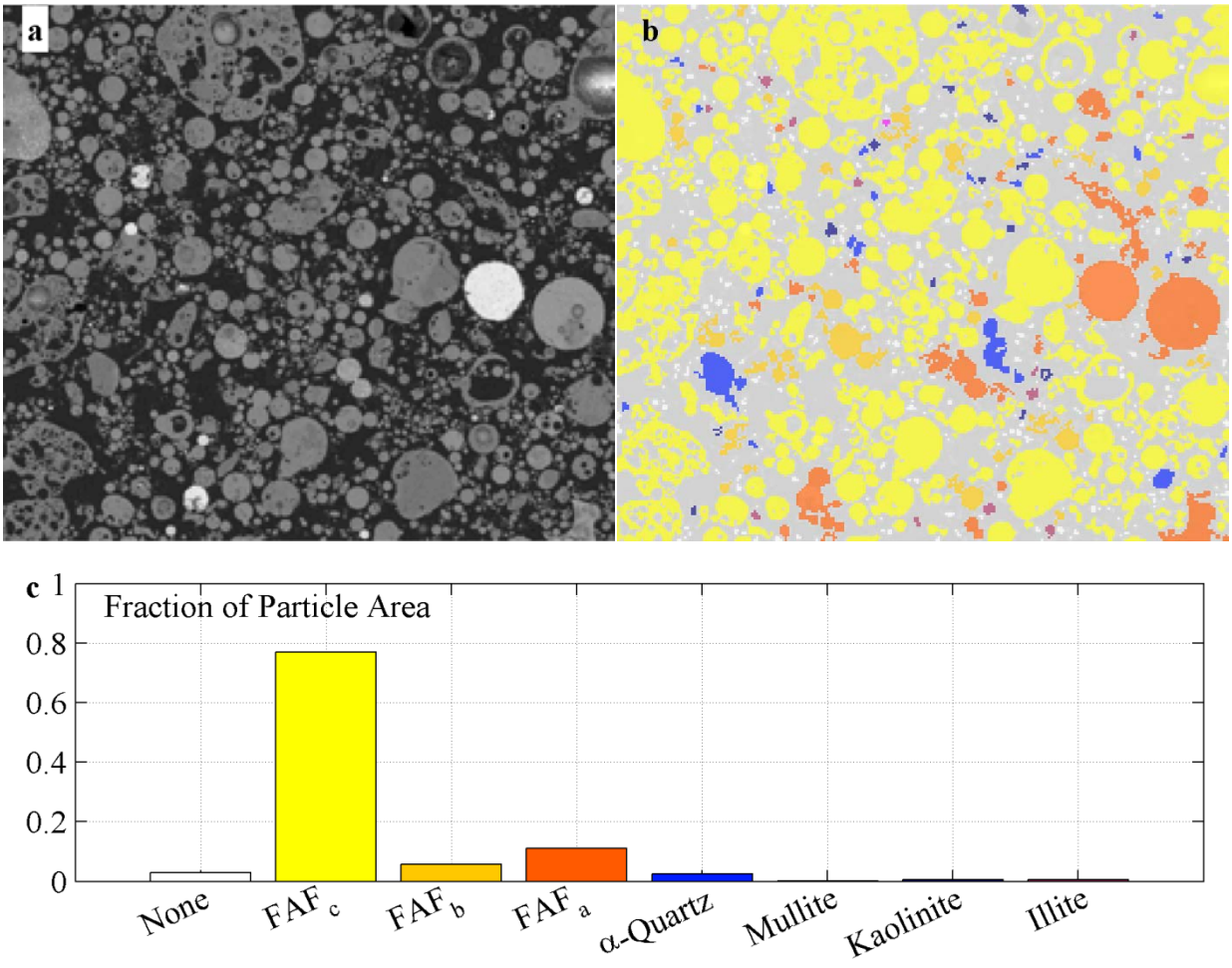

Figure 4.11: Results of the LDA classification algorithm applied to FAF particles mounted in resin. a) The original BSE micrograph of FAF particles, which appear white in the monograph. b) The BSE monograph overlain with each particle mapped with a unique color corresponding to the anhydrous database phases given in c. c) Bar graph illustrating the areas of each particle class identified. Those particles labeled “None” were not identified due to possessing too few particles to estimate the covariance matrix.

4.4.3. Estimation of reacted fractions

The results of the LDA algorithm applied to a random field of view in SVC are presented in Fig. 4.12. The original BSE intensity monograph is presented in Fig. 4.12a, and a phase map indicating the identified phases is presented in Fig. 4.12b. The coloring of phases in Fig. 4.12b corresponds to the bar chart in Fig. 4.12c, which shows the distribution of identified particles in the anhydrous phase. Thus, Fig. 4.12c serves as a legend for Fig. 4.12b. It is apparent in Fig. 4.12b that, although the large quartz grains from the QS fraction (top of image) are properly identified, a number of fly ash grains are also identified as quartz.

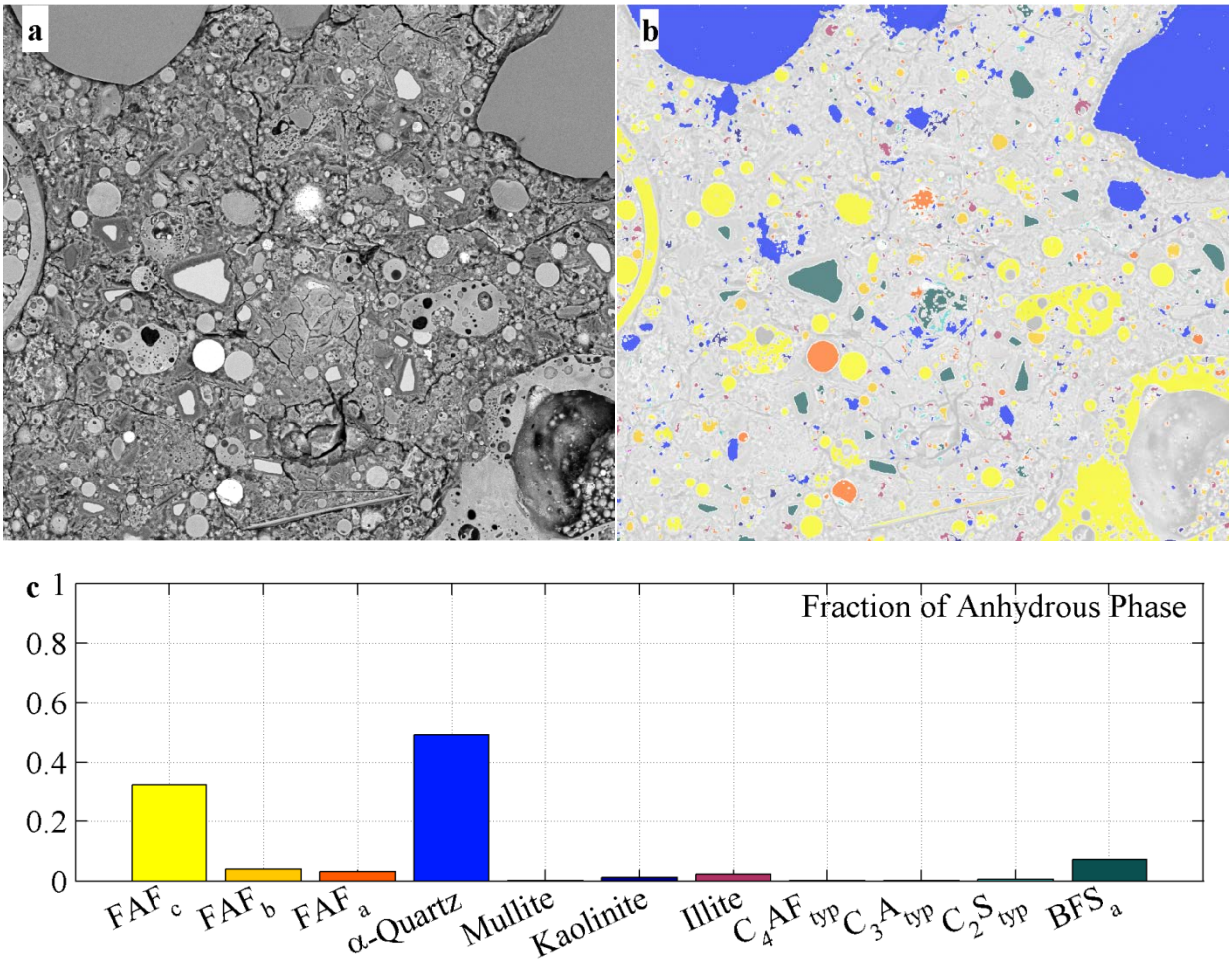

Figure 4.12: a) BSE monograph of an SVC field of view. b) Map of classified particles in the "anhydrous" image segment overlain on the grayscale monograph. Colors of the bars in c correspond to the coloring in b. c) Fractions of the anhydrous phase assigned to distinct classes in the anhydrous particle database.

Fig. 4.13 demonstrates the LDA algorithm without geometric descriptors applied to a field of view of SVC that contains a large kaolinite particle in the northwest quadrant and a large central illite particle that has been identified as FAF_b. Fig. 4.14 shows the same field of view evaluated with the LDA algorithm including the particle area and eccentricity descriptors. In Fig. 4.13, the central illite particle is correctly identified, but two clustered FAF particles in the northeast quadrant are now misidentified, likely as an artefact of their combined eccentricity. Such misclassifications are inevitable given the similarity in phyllosilicate and fly ash compositions; however, the differences in predicted unreacted fractions provide an indicator of the inherent uncertainty of the method. Comparison of Figs. 4.13c and 4.14c reveal that the measured fractions of the anhydrous phase are relatively stable for a number of species. However, the fraction of unreacted BFS varies by approximately 34%, whereas the unreacted fraction of FAF varies by approximately 42%, which is due to the renormalization of measured phase fractions to the non-quartz /illite/kaolinite regions of the field of view. Thus, the error in measuring quartz/illite/kaolinite is propagated through to the calculation of unreacted fraction. This error could be avoided by using a completely unbiased location sampling strategy, but a high time cost (see Section 4.2.2).

Further refinements could be made possible using expert supervision to reclassify apparently mislabeled particles with the added cost of possible human biasing. Such a strategy would likely require far less time to execute than manual identification of phases from scratch. In some situations, the LDA algorithm yields visually satisfactory results, as in Fig. 4.13. LDA lends itself to incorporating other metrics in the classification step, for instance crystallographic information, without the need for arbitrary scaling of the metrics.

In total, BSE and EDX spectra were collected at twelve SVC sites, and from these analyses, the reacted fractions of OPC, FAF, and BFS were estimated to be 100, 37, and 83% reacted. Complete or nearly complete reaction of OPC is feasible given the 30-month cure age of the specimen and comparisons with estimates of alite (C_3S), belite (C_2S), aluminate (C_3A), and ferrite (C_4AF) reacted fractions after 2 weeks of hydration obtained from an independent BSE-EDX investigation of the same OPC [5]. The limited reaction of fly ash is similar to that of other fly ashes reported in the literature [125]. Eighty-three percent slag reaction is also similar in magnitude to other reported values [163].

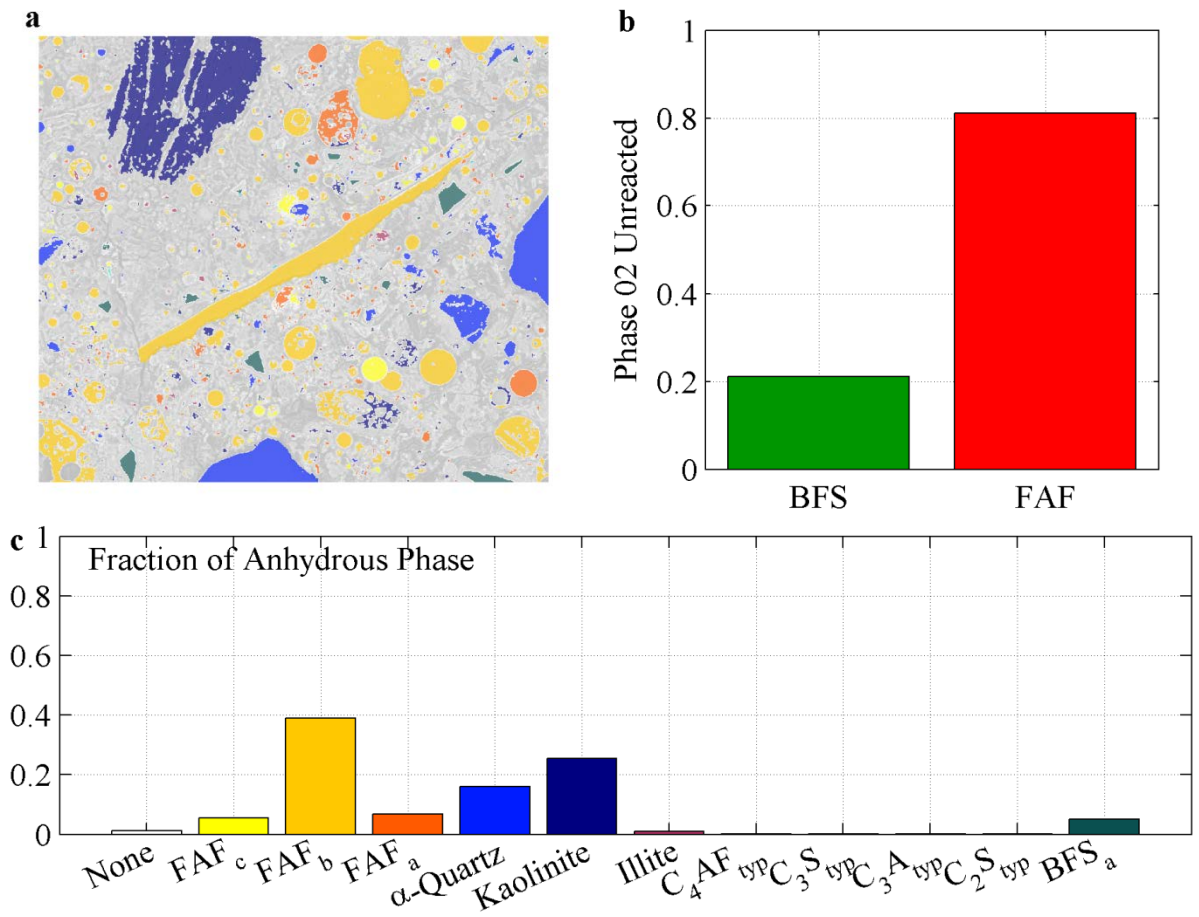

Figure 4.13: a) Map of classified particles in the “anhydrous” image segment overlain on the grayscale monograph. b) Unreacted fraction of BFS and FAF. c) Distribution of phases constituting the anhydrous portion. Colors of the bars in c) correspond to the coloring in a).

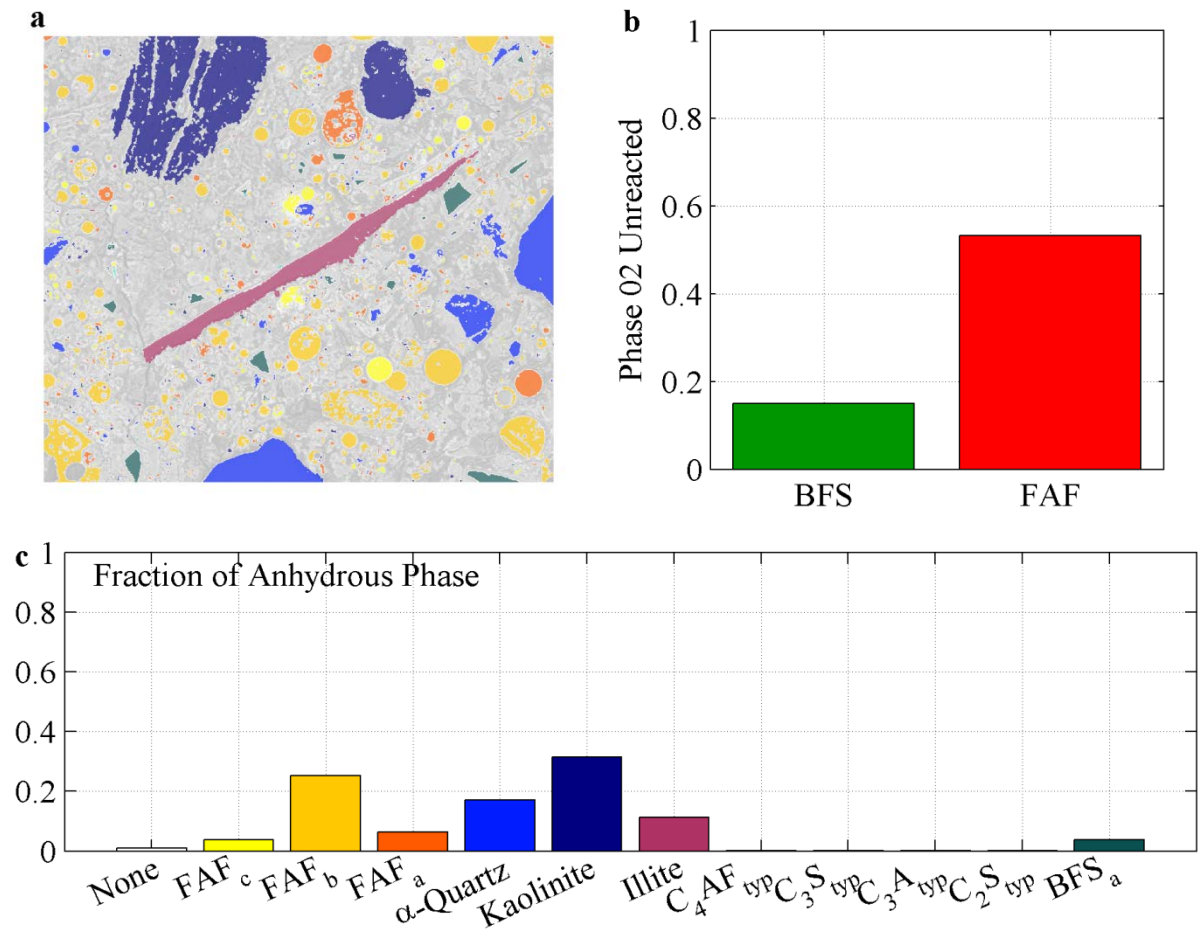

Figure 4.14: a) Map of classified particles in the "anhydrous" image segment using the LDA algorithm with geometric descriptors. b) Unreacted fraction of BFS and FAF. c) Distribution of phases constituting the anhydrous portion. Colors of the bars in c) correspond to the coloring in a).

4.5. Conclusions

A novel method has been presented for identifying the extent of reaction of anhydrous particles in blended cements and mortars containing SCMs using BSE-EDX analysis. Previous methods of particle identification have successfully utilized BSE information in the identification of anhydrous particles, but because blended cement mortars exhibit higher degrees of material heterogeneity than most cementitious materials, a new segmentation algorithm was developed that integrates both BSE intensity information and EDX spectral information to identify likely regions of anhydrous particles within a field of view. Likely anhydrous regions were compared

to a database of representative anhydrous particle compositions using the method of linear discriminant analysis. Results of the classification method applied to a realistic 30-month old blended cement mortar indicate highly satisfactory results for the identification of blast furnace slag particles. The identification of fly ash particles is complicated by the presence of quartz and of phyllosilicate minerals within the fine aggregate fraction of the mortar that exhibit elemental compositions very similar to those of the fly ash. To further enhance the classification procedure of these particles, geometric descriptors of particle shape and size were also integrated into the discriminant analysis, which demonstrated an improved ability to identify these particles. Results of three sampling locations indicate the estimated extent of reaction of blast furnace slag to be 83% with a coefficient of variation of 0.02 and for the fly ash, 35.8% with a coefficient of variation of 0.27. Further refinements to this identification method have been proposed, but at present, the algorithm executes on the order of 10 minutes. Thus, the method shows promise as a practical means of quantifying extent of reaction in realistic, aged cementitious materials.

CHAPTER 5

5. CHARACTERIZATION AND MODELING OF MAJOR CONSTITUENT EQUILIBRIUM CHEMISTRY OF A BLENDED CEMENT MORTAR[2]

Abstract

A blended cement mortar containing Portland cement, granulated blast furnace slag, fly ash and quartz sand was modeled using a set of solid phases known to form in hydrated OPC with the geochemical speciation solver LeachXS/ORCHESTRA. Comparison of modeling results to the experimentally determined pH-dependent batch leaching concentrations (USEPA Method 1313) indicates that major constituent concentrations are described reasonably well with the Portland cement mineral set; however, modeled and measured aluminum concentrations differ greatly. Scanning electron microscopic analysis of the mortar reveals the presence of Al-rich phyllosilicate minerals: kaolinite and potassic phyllosilicates similar in composition to illite and muscovite. Whereas both phyllosilicates are present as part of the fine aggregate, the morphology and saturation index of kaolinite suggest that some may be formed *in situ*. The inclusion of kaolinite in speciation modeling provides a substantially improved description of the release of Al and therefore, suggests that the behavior of phyllosilicate phases may be important for predicting long-term physico-chemical behavior of such systems.

5.1. Introduction

The extensive incorporation of ground granulated iron blast furnace slag (BFS) and coal combustion fly ash (FAF) to cementitious materials used in barriers for nuclear waste management has heightened the need for understanding the physico-chemical behaviors of the resulting grout and concrete systems under use conditions in the environment and over extended time frames. Blended cements exhibit a high degree of complexity due to the variability of both the source and the processing of the parent materials, yielding end products comprised of a

[2] Published in a special issue of the European Physics Journal as part of NUCPERF 2012

mixture of glassy and mineral phases. Ordinary Portland cements (OPC) are also complicated materials but are often well-described by thermodynamic equilibrium models [164]. Whereas the stable solid phases of ordinary Portland cement (OPC) have been studied in great detail, the chemistry fly ash and slag blended cement has received relatively less attention. Given that OPC is generally more reactive than slag and fly ash, the mineralogy of OPC provides a logical starting point for describing the major constituent chemistry of blended cement mortars. To this end, the work presented here represents a preliminary investigation of the applicability of a set of equilibrium phases developed for Portland cement to a blended cement mortar comprised of OPC, FAF, BFS, and quartz sand (QS).

5.2. Methods

5.2.1. Material preparation

Mortar samples for chemical characterization were prepared by mixing ordinary Portland cement, blast furnace slag, coal fly ash, water, and quartz sand in the proportions listed in Table 5.1, resulting in a water-to-binder (w/b) ratio of 0.45. The formulation is analogous to structural vault concretes in nuclear waste management applications [1] and is referred to herein as SVC. Total elemental composition of the binder materials for major constituents, as determined by X-ray fluorescence spectroscopy (XRF) are given in Table 5.2.

Each SVC specimen was cast as a slab measuring 15 cm x 30 cm x 5 cm (width x length x height), removed from its mold after 24 hours, and allowed to cure at 98 ± 2% relative humidity and 25 ± 1 °C in a nitrogen-purged atmosphere. After 30 months of curing, the outer surfaces of the slabs were removed to mitigate the effects of exposed and molded surfaces, and the remaining interior portion of the slab was crushed and sifted to less than 2 mm particle size for use in leaching experiments.

Table 5.1: Raw material properties of the mortar used in this study. Particle size information was determined from particle size information provided by [138].

Material	Abbrev.	Mass %	Density [kg/L]	Mean Particle Diameter [μm]	Median Particle Diameter [μm]
Blast Furnace Slag	BFS	8.03	2.89	3.87	8.12
Type F Fly Ash	FAF	16.93	2.33	6.02	14.90
Type I Cement	OPC	5.40	3.01	4.16	11.30
Quartz Sand	QS	55.02	2.54	590.6	596.45
Water	-	14.62	1.00	-	-

Table 5.2: Major element composition of the binder materials as determined by XRF, in mass percent. Carbon (C) is reported as total carbon.

Binder	C	O	Na	Mg	Al	Si	S	K	Ca	Fe
BFS	---	38.17	0.13	6.88	3.46	17.06	0.82	0.35	23.75	0.21
FAF	1.50	45.49	0.25	0.62	15.08	24.42	0.04	2.14	0.86	4.98
OPC	2.50	31.34	0.13	0.58	2.15	7.67	1.55	0.38	41.30	2.70

5.2.2. pH-dependent leaching test

The USEPA Method 1313 [76] pH-dependent liquid-solid partitioning protocol was used to evaluate major constituent concentrations. Forty grams of SVC were added to 400 mL of solution comprised of deionized water plus HNO_3 or KOH/NaOH for acidification or basification, respectively. The quantities of acid and base additions were prescribed such that nine distinct solution pH values within a tolerance of 0.5 pH units were achieved at the end of the extraction period: 2.0, 4.0, 5.5, 7.0, 8.0, 9.0, 10.5, 12.0, and 13.0. Two replicates of each pH position were achieved, and for the base addition, KOH and NaOH were added to distinct replicates in order to measure the solubility of both Na^+ and K^+ at high pH, respectively. Solid samples and leaching solutions were prepared in sealed high density polyethylene bottles with minimal headspace and tumbled end-over-end for a period of 48 hours. Once tumbled, the pH and electrical conductivity of the leachates were measured, and the leachate was vacuum filtered. The filtered leachate was then analyzed for total cation concentrations using inductively coupled

plasma optical emission spectroscopy; specific methods, detection limits and quality control procedures used during testing are available [165].

5.2.3. Geochemical modeling

LeachXS/ORCHESTRA [63] is a geochemical speciation mass transport solver that solves equilibrium speciation via Newton-Raphson minimization of the system of equations composed of the laws of mass action and conservation of mass, as outlined in Chapter 2. The solid phases considered for thermodynamic equilibrium calculations are given in Table 5.3 with solubility products from Lothenbach, et al. [70]. Additionally, the precipitation of amorphous calcium silicate hydrate (C-S-H) was modeled using the ideal solid solution with Tobermorite-like ($C_{0.8}SH_{1.3}$) and Jennite-like ($C_{1.67}SH_{2.1}$) end-members proposed by Kulik and Kersten [166] with end-member solubilities determined by Lothenbach and Winnefeld [72]. Adsorption of K^+ and Na^+ onto C-S-H was modeled using partition coefficients fitted to experimental data from a study of alkali uptake onto synthetic C-S-H gel [118]. Assuming a C-S-H surface area of 10.04 m^2/kg of C-S-H [167] and a silanol site density of 4.8 mol/nm^2 [168], and specifying the surface acidity as [168]

$$-SiO^- + H^+ \rightleftharpoons -SiOH, \quad K = 1.59 \times 10^{10}, \tag{5.1}$$

the adsorption constants for Na^+ and K^+ were found to be

$$\begin{aligned} -SiO^- + Na^+ &\rightleftharpoons -SiONa, \quad K = 1.53 \times 10^{17} \\ -SiO^- + K^+ &\rightleftharpoons -SiOK, \quad K = 1.31 \times 10^{17} \end{aligned} \tag{5.2}$$

where K is the equilibrium constant and $-SiO^-$ denotes the silanol site. Adsorption onto $-SiO^-$ of the C-S-H is the only mechanism of alkali uptake considered although the alkali filling of interlayer spaces in aluminum-substituted C-S-H proved to be a significant sink for K^+ and Na^+ in synthetic gels [119] as well as for Al^{+3} [169, 170].

Table 5.3: Solid phases considered in the SVC assemblage. Species sharing superscripts indicate solid solution end-members. Mineral names are given in cement chemists' shorthand: C – CaO, A – Al_2O_3, S – SiO_2, F – Fe_2O_3, s – S_2O_3, c, CO_2, M – MgO. Amorphous phases are denoted (am) and microcrystalline phases (mcr).

$Ca(OH)_2$	$CaCO_3$	$CaSO_4 \cdot 2H_2O$	C_3AH_6	$C_{1.67}SH_{2.1}^{*****}$
$Mg(OH)_2$	$MgCO_3$	$C_4AsH_{12}^{***}$	C_3FH_6	$M_4AH_{10}^{******}$
$Al(OH)_3$(am)	$C_4Ac_{0.5}H_{12}^{*}$	$C_4FsH_{12}^{***}$	C_2ASH_8	$M_4FH_{10}^{******}$
$Fe(OH)_3$(mcr)	$C_4Fc_{0.5}H_{12}^{*}$	$C_6As_3H_{32}^{****}$	C_2FSH_8	M_4AcH_9
SiO_2 (am)	$C_4AcH_{11}^{**}$	$C_6Fs_3H_{32}^{****}$	$C_3AS_{0.8}H_{4.4}$	
$C_6Ac_3H_{32}$	$C_4FcH_{12}^{**}$	$K_2Ca(SO_4)_2$	$C_{0.8}SH_{1.3}^{*****}$	

Reacted fractions of OPC, FAF, and BFS were estimated to be 100, 30, and 80% reacted, respectively based on separate electron microscopy evaluations (Chapter 4, Section 4.4.3). Complete or nearly complete reaction of OPC is feasible given the 30-month cure age of the specimen and comparisons with estimates of alite (C_3S), belite (C_2S), aluminate (C_3A), and ferrite (C_4AF) reacted fractions after 2 weeks of hydration obtained from an independent scanning electron microscopy energy dispersive X-ray (SEM-EDX) investigation of the same OPC [5]. The limited reaction of fly ash is similar to that of other fly ashes reported in the literature. Additionally, limited surface reaction of the Fe-rich FAF particles was observed. Such little reaction reflects the very low concentrations of alkali and alkaline species present in FAF, as presented in Table 5.2. Eighty percent of slag reacted is similar in magnitude to other reported values [163].

Assuming a single value for reacted fraction of a component material implies a uniform dissolution of each component material, a situation unlikely to occur in reality. At least one study suggests that the dissolution of slag is substantially incongruent [171]. Indeed, in experiments conducted by the authors, when exposed to strongly acidic solution, the BFS off-gassed H_2S (g) and formed a silicate gel. Incongruent dissolution of fly ash particles is also likely given their glassy nature; moreover, the distinct morphologies and compositions of FAF particles suggest distinct intrinsic solubilities among the subtypes of FAF particles. Nonetheless, a uniform reacted fraction is expected to reflect first-order effects on the extent of binder reaction.

5.3. Results and discussion

Modeled concentrations using the OPC solid phases listed in Table 5.3 are compared to USEPA Method 1313 leachate concentrations (measured in duplicate) in Fig. 5.1. The resultant equilibrium pH without the addition of acid or base was found to be approximately 12.2

In general, the trends observed in the data are well captured by the equilibrium phases listed in Table 5.3. The modeled solubility of Ca falls (Fig. 5.1a) within an order of magnitude of the measured values over the pH range of interest (8<pH<13). Despite good agreement between measured and modeled Si (Fig. 5.1b) concentrations at pH 10 and pH 12, significant discrepancies are apparent at low and high pH. Several factors may be responsible for these differences. First, the solid solution model of C-S-H which has been developed to describe the formation of C-S-H is assumed here to also describe the dissolution of C-S-H; however, this assumption may not hold if the stoichiometries of C-S-H in this study are outside the range of those for which the C-S-H model end-member solubilities were fitted. Second, silicate phases typically exhibit slow reaction kinetics, and therefore, the experimental results may only approximate the final equilibrium state of the system; this scenario should be more likely near neutral pH where reaction kinetics are typically slowest. The specific adsorption of K^+ and Na^+ onto C-S-H also serve as indicators of the performance of the C-S-H model because the number of silanol adsorption sites is fixed by the total mass of C-S-H present in the system. The trends in solubilities of K^+ (Fig. 5.1c) and Na^+ (Fig. 5.1d) are well captured by the geochemical model (the increasing solubility of K^+ at high pH is an artefact of the KOH addition specified by Method 1313), indicating that the mass of C-S-H formed may be well approximated by this model. Differences in measured and modeled alkali concentrations around pH 8 may reflect a limitation of the homogeneous reacted fraction assumption, particularly for fly ash, the most alkali-rich binder material. Nevertheless, these differences are less than an order of magnitude.

The pH-dependent solubility of Mg is described to within an order of magnitude across the pH range of interest (Fig. 5.1e) which suggests that the hydrotalcite-type phase is the key solubility controlling phase for this Mg in this system. Strong correlation between total S prediction and experiment (Fig. 5.1d) was found, owing primarily to the precipitation of ettringite.

An important deficiency in the modeling results is the characterization of aluminum. As demonstrated in Fig. 5.2a, the solubility of Al is overestimated by 2 to 3 orders of magnitude

between pH 8 and 10. To account for this discrepancy, a number of factors were considered. The precipitation of siliceous hydrogarnet ($C_3AS_{0.8}H_{4.4}$), which forms very slowly at ambient temperatures [172], has been suppressed in the modeling results presented in Fig. 5.2, but it was found that the effect of including $C_3AS_{0.8}H_{4.4}$ was to underestimate the solubility of Al by 2 to 3 orders of magnitude at pH 12 and above. Moreover, $C_3AS_{0.8}H_{4.4}$ was only found to precipitate above pH of about 10.5. Crystallographic characterizations of SCM-replaced Portland cements signify the importance of substitution of Al^{+3} into the silicate tetrahedral network of C-S-H [169, 173-175]. Given the lack of thermodynamic data, the formation of Al-substituted C-S-H (C-A-S-H) was assessed provisionally by partitioning 0.17 moles of Al^{+3} into every 1 mole of Tobermorite-like end-member and for every 1 mole of amorphous silica formed; this rate of substitution is on the order of experimentally measured values [174, 175]. As demonstrated in Figs.5. 2b and 5.2d, considering C-A-S-H in this manner results in a redistribution of solid phases signifying that sufficient Al would still be free to precipitate all the Al-bearing phases present in Fig. 5.2b; thus, the solubility prediction of Al is unaffected (Figs. 5.2a and 5.2c). In 5.2a and 5.2b, no Al uptake by the C-S-H is considered whereas in 5.2c and 5.2d, 0.17 moles of Al per mole of Si are partitioned into amorphous silica and Tobermorite-like C-S-H end-member.

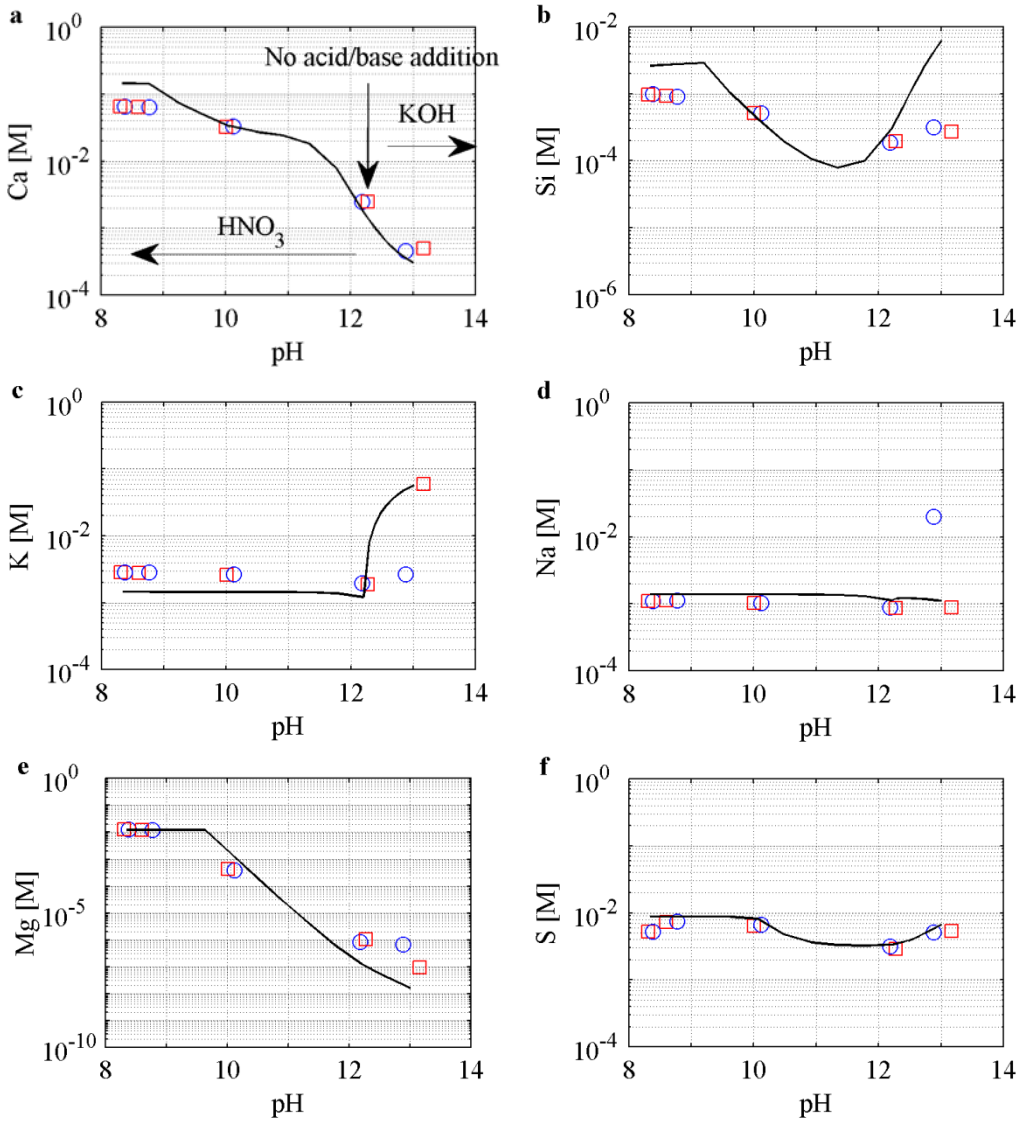

Figure 5.1: Comparison of modeled (black lines) and measured (circles and squares) major constituent leachate concentrations (as total dissolved element concentrations) of USEPA Method 1313 performed on SVC. The increasing concentration of K at high pH in c) and of Na in d) are artefacts of the leaching method: independently KOH solution and NaOH were used to adjust the pH of the leachate to a pH 12.5 ±0.5, although only the KOH addition was modeled.

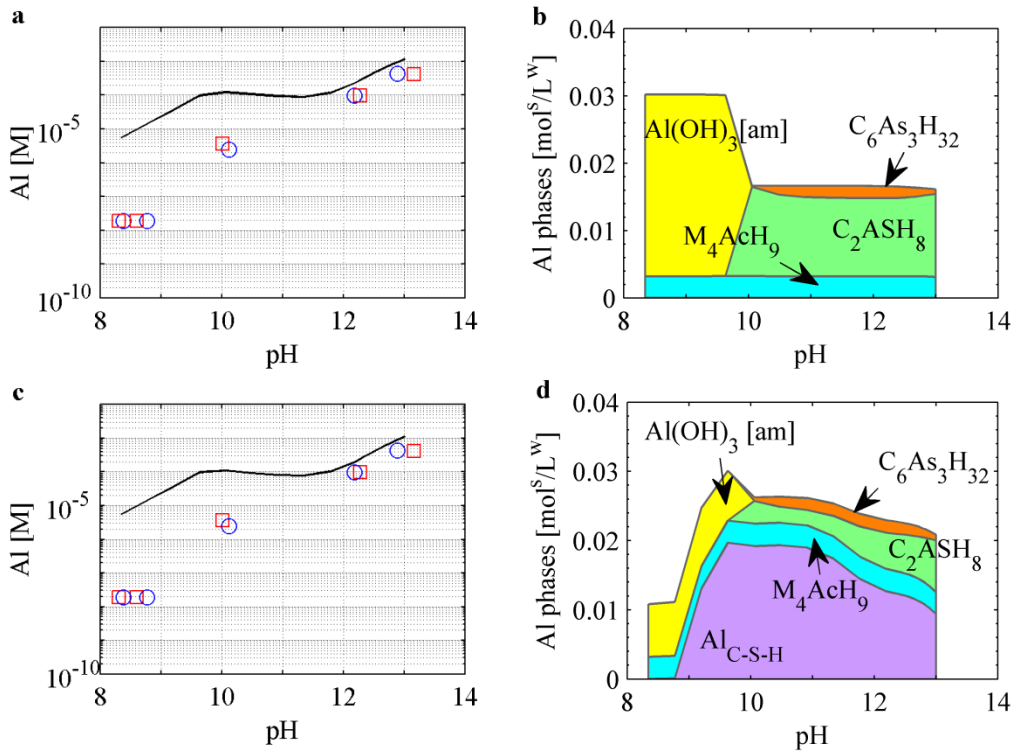

Figure 5.2: a and c) Comparison of modeled (black lines) and measured (circles and squares) major constituent leachate concentrations and b and d). the concentrations of Al-bearing solid phases.

SEM-EDX analyses provide an indication of additional phases that may play a role in determining Al solubility: a number of phyllosilicates (PS) are apparent within the hydrated SVC after 30 months of curing (Fig. 5.3). To the authors' knowledge, such phases have not been identified previously in blends of cement, slag and fly ash, but their formation is plausible given that PS are clay minerals that commonly form as the result of weathering, diagenesis, and low-grade metamorphism in the natural environment. A number of PS grains are present in the component quarts sand aggregate, but the relative abundance and wide range of sizes of these particles in the SVC material, as well as the spatial and stoichiometric correlation of PS to fly ash grains (Fig. 5.3), suggest that alteration of fly ash is a significant if not primary source of PS formation. Quantitative EDX assay, an example of which is illustrated in Fig. 5.4, indicates that these particles exhibit two basic stoichiometries: that of kaolinite ($Al_2Si_2O_5(OH)_4$) and that of the mica mineral muscovite ($KAl_2(Si_3Al)O_{10}(OH)_2$). Whereas kaolinite is a common weathering product of glassy materials such as volcanic tuff and has been shown to form in municipal solid

waste incinerated bottom ash [176, 177], pure muscovite typically forms in hydrothermal environments and weathers to a class of minerals referred to as illite, a PS of the mica group exhibiting a range of compositions somewhat intermediate between kaolinite and muscovite [159]. In order to examine the effects of PS on the geochemical response of the SVC system, the precipitation/dissolution reactions of kaolinite and a typical illite [178] have been considered, although such an abstraction belies the complexity of most clay mineral systems.

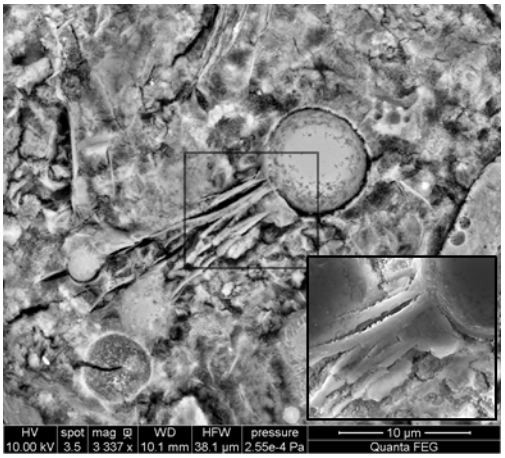

Figure 5.3: BSE micrograph of kaolinite formation in close proximity to a fly ash particle in the SVC material, with an inset of the secondary electron micrograph of the FAF-PS interface.

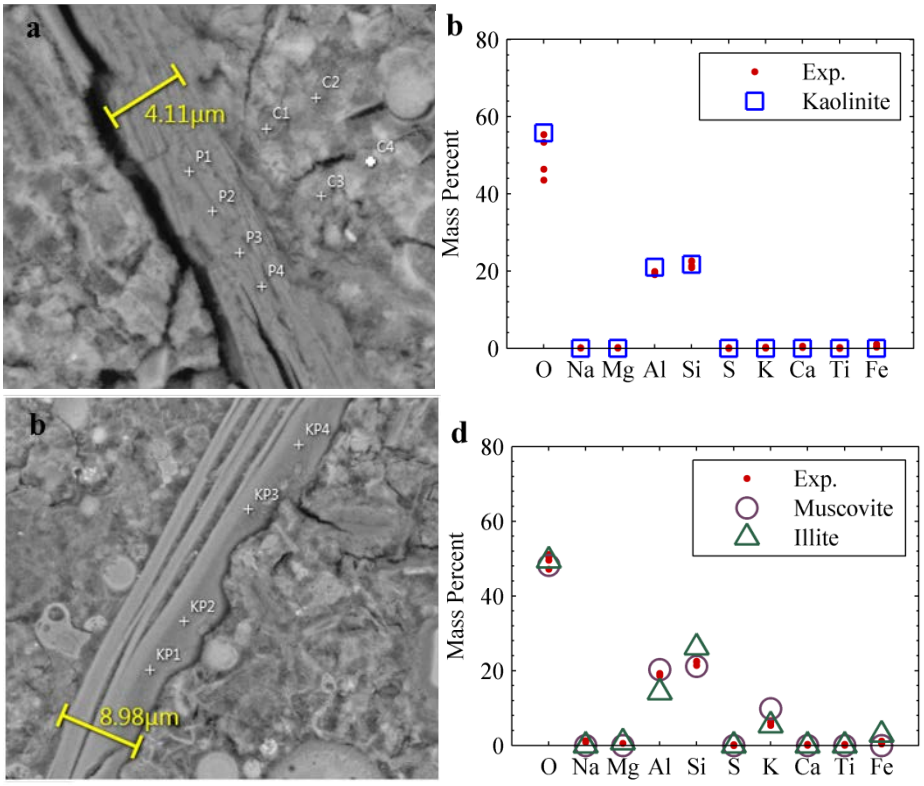

Figure 5.4: a) Backscattered electron micrograph of a phyllosilicate presumed to be kaolinite and b) quantitative EDX spectra results for points P1 to P4 (gray error bars) and the theoretical composition of kaolinite (red star). c) Backscattered electron micrograph of a potassic phyllosilicate presumed to be illite and d) quantitative EDX spectra results for points KP1-KP4 (gray error bars) and the theoretical composition of a typical illite [159] (red star).

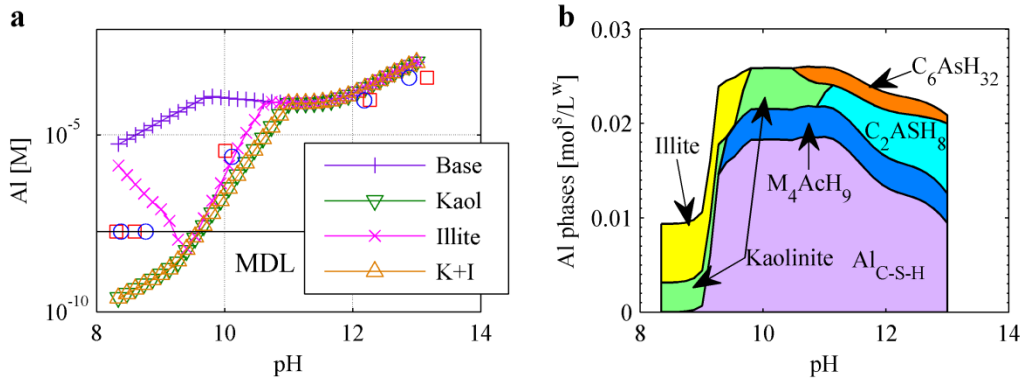

Figure 5.5: a) Modeled (see legend) and experimental (red squares and blue circles) equilibrium concentration of total dissolved Al with base mineral set (Base) when including kaolinite, illite, and kaolinite+illite (K+I). The experimental values between pH 8 and 9 reflect the method detection limit of the IPC-OES technique. b) The distribution of Al-bearing phases when including kaolinite and illite.

Fig. 5.5a demonstrates the effects of including kaolinite and illite on the equilibrium concentrations of Al. In general, the description of Al solubility below pH 10 is much improved, although underestimated, by considering kaolinite in the thermodynamic equilibrium model, but is virtually unaffected by the inclusion of illite. Including illite in the model prediction drastically reduces the predicted solubility of K below pH 10, however, which perhaps suggests that the illite present in SVC was present in the quartz sand parent material plays a relatively small role in the equilibrium chemistry. That illite may be relatively unreactive in this system is further substantiated by the observation that cracking is apparent near kaolinite grains but not illite grains.

A few words of caution are in order concerning the inclusion of PS in thermodynamic equilibrium models. The first is that, in the natural environment, the speciation of PS is often complex in that PS sheets are often intermixed across multiple length scales resulting in polymorphs, solid solutions and mixed-layer assemblages such that crystallographic identification and chemical characterization is difficult. Second, PS undergoing dissolution and precipitation often require months to fully equilibrate, depending on the grain size among other factors. Whereas the mortar used in this study has been size-reduced after curing to facilitate testing, a careful study of reaction rate would be necessary to determine if a near-equilibrium condition has truly been reached. Examination of Fig. 5.5b reveals kaolinite is unstable above pH of around 11.5 whereas the pore water pH of the unaltered SVC was measured as 12.2. Estimation of saturation indices based on experimentally measured concentrations suggests that kaolinite is supersaturated at pH 10 but undersaturated at pH 12. Therefore, from a macroscopic thermodynamic point of view, the kaolinite observed in the SEM micrographs of SVC should be dissolving slowly or the pH of the pore solution is somewhat less than 12 within the material. Thus, the fact that the stoichiometry and solubility constant of kaolinite provide a more reasonable Al response is a necessary but not sufficient condition for stating that kaolinite is indeed the solubility-controlling mineral in this pH range for the SVC material. What can be said is that the physical and chemical evidence strongly suggest that Al-bearing PS phases are important for characterizing the behavior of SVC.

Furthermore, a rigorous characterization of the physico-chemical properties of blended cements may require consideration of phases other than those that control solubility. For example, considering the relatively high loading of slag in the SVC mix (52% of the binder, by mass), a substantial portion of fibrillar magnesium silicate hydrates (M-S-H) may be expected to form upon hydration [179], and indeed, a fibrillar product in the reaction rind of BFS is apparent in backscattered electron micrographs, as shown in Fig. 5.6. Encapsulating the M-S-H zone is what appears to be dense C-S-H; the presence of this sharp compositional interface suggests that migration of constituents from the unreacted slag grain to the surrounding paste would be controlled by the dense C-S-H layer. If M-S-H is effectively sequestered, the thermodynamic behavior of the M-S-H may be of little consequence to the composition of the partial equilibrium assemblage *in situ*; however, cracking, decalcification, and other degradation phenomena, and especially particle size reduction, may degrade the C-S-H barrier, exposing unreacted slag to solution and thereby altering the system equilibrium. Such a phenomenon underscores the need for a mechanistic description of cementitious systems adaptable to a wide range of conditions.

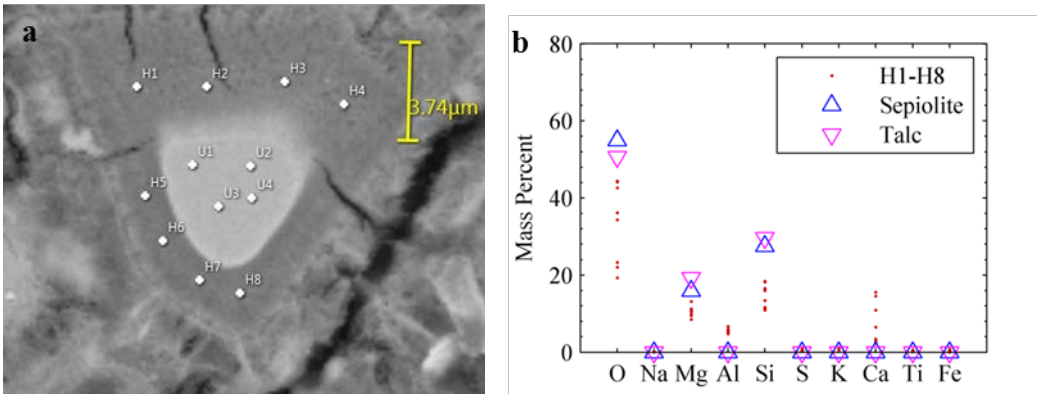

Figure 5.6: a) Backscattered electron micrograph of a partially hydrated slag particle in unaltered SVC. b) Comparison of quantitative EDX analyses of the points H1 to H8 with the stoichiometries of sepiolite and talc, two pure phases to which synthetic M-S-H has been likened on the basis of crystallographic similarities [179].

5.4. Conclusions

A known set of Portland cement solid phases was used to model the equilibrium chemistry of a blended cement mortar. Modeling results generally exhibited the trends and magnitudes observed

in a standard equilibrium pH-dependent leaching experiment, aluminum being the notable exception. The exclusion of siliceous hydrogarnet from equilibrium calculations improved the description of Al solubility above pH 10. Below pH 10, the description of Al solubility is greatly improved by the inclusion of kaolinite whose presence has been inferred through SEM-EDX analysis. The presence of potassic phyllosilicates of similar composition to illite and muscovite was also suggested by SEM-EDX analysis; however, the inclusion of illite in thermodynamic equilibrium model resulted in no demonstrable improvement in Al solubility prediction and a worse prediction of K solubility. Whereas kaolinite was not definitively identified as the Al solubility-controlling species below pH 10, the agreement between equilibrium modeling and experiment and the SEM-EDX evidence strongly implicate Al-bearing phyllosilicates as important species that should be considered when describing both the chemical and physical properties of slag, fly ash and Portland cement blends.

CHAPTER 6

6. REACTIVE TRANSPORT MODELING OF EXTERNALLY-INDUCED AGING OF BLENDED CEMENTITIOUS MATERIALS

Abstract

Predicting the long-term leaching behavior of blended cementitious materials requires knowledge of the solid phases that control constituent solubility. Whereas these phases are largely known for Portland cements, to what extent the chemical description needs to be modified for blended cements remains an open question. Moreover, the chemical description for long-term reactive transport prediction should encompass a number of possible phases depending upon the chemistry of the ambient environment. An augmented set of solid phase thermodynamic constants developed primarily for modeling the hydration of Portland cements has been used to model the equilibrium chemistry of a blended cement mortar. Comparison of equilibrium modeling results to both pH dependence leaching tests and to established methods of defining the partial equilibrium assemblage indicate that the extent of reaction and the modified set of thermodynamic parameters yield reasonable predictions of pH-dependent solubility of major constituents. The thermodynamic model has also been applied to the modeling of aging processes blended cement mortar monoliths, which indicate that many constituent release behaviors seem to be described by the thermodynamic model as well. Notable exceptions and areas for further research are highlighted.

6.1. Introduction

The widespread application of cementitious materials and the ever increasing complexity of blended cement designs, such as those incorporating iron blast furnace slag and coal combustion fly ash, have rendered impractical the experimental characterization of cement-based structures over the entire range of design parameters. Moreover, cements and blended cements have been employed extensively for the immobilization of wastes [180-182], the potency of which may be only slowly diminished if at all. The service life of these cementitious barriers may span

thousands of years, making experimental characterization impossible over the time frames of interest. For these reasons, the mechanistic description of the

The field of cement science has only very recently turned its attention to the rigorous mineralogical characterization of cements that incorporate pozzolanic materials, that is, those containing reactive silica. The additional complexity introduced by the incorporation of wastes into the cementitious matrix exacerbates the need for fundamental understanding of these materials. In the field of waste management, however, the systematic thermodynamic characterization and modeling of cementitious waste forms is highly varied and heterogeneous materials 1) have demonstrated the similarities in leaching behaviors of highly diverse cementitious systems and 2) have led to the inference of a number of underlying mechanisms controlling constituent release in both laboratory and field testing experimental scenarios [6, 183-188]. Such studies are invaluable in assessing both where uncertainties in the mechanistic description lie and in gauging the magnitudes of those uncertainties. It is within this context that the present work seeks to examine a blended cement mortar (denoted SVC) typical of the structural vaults concretes used in cementitious waste barrier applications [1].

In Chapter 4, backscattered electron microscopy coupled with energy dispersive X-ray (BSE-EDX) analysis was used to quantify the extent of reaction of the ordinary Portland cement (OPC), Class-F coal combustion fly ash (FAF), Grade 100 blast furnace slag (BFS), and graded quartz sand (QS) which comprised the mortar. Chapter 5 examined how well a set of equilibrium phases developed for Portland cement [70, 164] described SVC by comparing model predictions to standard pH-dependent batch leaching tests [76, 165, 189]; with a few additions and modifications, it was determined that major constituent solubility as a function of pH was generally well-described by a subset of solid phases developed for modeling the hydration of ordinary Portland cement. The present work builds upon this idea by using standard leaching protocols as a means of investigating the validity of the component masses calculated from reacted fraction measurements. The first objective of this work is to vary the extent of reacted fraction parameters over a feasible range to assess both the sensitivity and the accuracy of the partial equilibrium representation of SVC. Results are compared to established methods of determining component masses.

The second goal of the present work is to investigate the response of the thermodynamic model to chemical aging as a result of exposure to external leaching solutions. Thus, the second primary objective is to compare reactive transport simulations, which employ the thermodynamic description of SVC, to measurements of constituent release and/or uptake in four distinct aging scenarios. The four aging conditions considered herein are exposure to deionized water, sodium sulfate, magnesium sulfate, and sodium carbonate solutions, each of which may be considered an "accelerated" aging solution in that the differences in composition between the cement system and the external solutions are more extreme than would normally be expected in the natural environment.

6.2. Materials and methods

6.2.1. Component materials

The blended cement mortar studied is composed of Type I/II Portland cement OPC [134], grade 100 ground granulated blast furnace slag (BFS) [135], Type F coal combustion fly ash (FAF) [136], and quartz sand (QS) [137]. Total elemental composition for the major constituents of all four materials, as determined by X-ray fluorescence (XRF) spectroscopy (Arcadis, USA) are given in Table 6.1.

Table 6.1: Major element composition of the component materials as determined by XRF, in mass percent. Carbon (C) is reported as total carbon.

Binder	C	O	Na	Mg	Al	Si	S	K	Ca	Ti	Fe
BFS	---	38.17	0.13	6.88	3.46	17.06	0.82	0.35	23.75	.03	0.21
FAF	1.50	45.49	0.25	0.62	15.08	24.42	0.04	2.14	0.86	1.67	4.98
OPC	0.39	34.62	0.21	0.69	2.59	9.15	1.20	0.53	43.90	0.16	4.49
QS	0.93	52.35	0.02	0.00	2.45	43.82	0.00	0.18	0.01	0.02	0.21

Blended mortar samples (SVC) were prepared by mixing OPC, BFS, FAF, and QS in the proportions listed in Table 6.2; this formulation is within the family of compositions used as structural concretes in nuclear waste management applications, with the exception that no coarse

aggregate is present in the mortar presently studied [1]. SVC specimens were cast as slabs measuring 15 cm x 30 cm x 5 cm (width x length x height), removed from their molds after 24 hours, and allowed to cure at 98 ± 2% relative humidity and 25 ± 1°C in a nitrogen-purged atmosphere for 30 months. Samples for granular material leaching tests were generated by first grinding and discarding the outer surfaces of a slab and then crushing and sifting the material to a particle size of less than 2 mm.

Table 6.2: Mix design of the blended cement mortars studied herein, SVC.

Component	Mass %	Vol. %
BFS	8.0	5.8
FAF	16.9	15.1
OPC	5.40	6.0
QS	55.0	45.0
Water	14.6	30.4

6.2.2. pH dependent leaching

The USEPA Method 1313 [76] pH-dependent liquid-solid partitioning protocol was used to evaluate major constituent concentrations. Forty grams of SVC were added to 400 mL of solution comprised of deionized water and HNO_3 or KOH for acidification or basification, respectively. The quantities of acid and base additions were prescribed such that five distinct solution pH values, within a tolerance of 0.5 pH units were achieved at the end of the extraction period: 2.0, 4.0, 5.5, 7.0, 8.0, 9.0, 10.5, 12.0, and 13.0. The acid and base additions and resultant pH are given in Table 6.3 for the pH range of 8 to 14 and for the lowest pH for determination of availability as per Method 1313. The pH point at 12.0±0.5 was obtained without the addition of acid or base and is termed the “own pH” of the material. Solid samples and leaching solutions were prepared in sealed high density polyethylene bottles with minimal headspace and tumbled end-over-end for a period of 48 hours. Once tumbled, the pH and electrical conductivity of the leachates were measured, and the leachate was vacuum filtered. The filtered leachate was then analyzed for total cation concentrations using inductively coupled plasma optical emission

spectroscopy. The entire extraction procedure was performed in duplicate. Specific methods,, detection limits, and quality control procedures used during testing are available in [165].

Table 6.3: Equivalent base additions and resultant pH for the Method 1313 leach test.

Mean equivalent base addition [meq/gram]	Solution pH
0.68	13.02
0.00	12.225
-0.79	10.065
-1.80	8.685
-4.2	1.69

6.2.3. Accelerated aging

After 30 months of curing, cylinders measuring 18.0 ± 0.5mm outside diameter were cored from the slabs. The radial surface of each cylinder was ground using a progression of silicon carbide papers in order to eliminate the annular high-porosity region created by the coring process. The top and bottom of each cored cylinder were sawn off using a low speed saw in order to minimize the effects of air-exposed and molded surfaces, respectively. Each cylinder was then cast into a cylindrical acrylic sleeve with methacrylate resin, and the top of the cylinder and sleeve were again sawn to yield a cylinder of 20 ± 0.5 mm in length with a single exposed face, establishing a one-dimensional diffusion boundary. Sequential grinding and diamond-paste polishing of the exposed face followed by 20 seconds of sonication in acetone was performed in order to eliminate artificial porosity created by sawing.

Leaching of monolith cylinders was accomplished using a modified version of the draft USEPA monolith leaching protocol [68] wherein monolithic materials are exposed to an external solution of deionized water (DI) at a ratio of 10 L of solution per cm^2 of exposed monolith surface area, which is commonly known as the finite bath boundary condition within numerical contexts. Four distinct leaching solutions were chosen to simulate the aging of cementitious samples in aggressive environments: DI and aqueous solutions of 0.250 [M] Na_2SO_4 (NS), 0.015 [M] $MgSO_4$ (MS), and 0.350 [M] Na_2CO_3 (NC). DI leaching was selected to induce decalcification of

the C-S-H phase primarily and serves as a reference condition, whereas NS and MS solutions were expected to form ettringite, hydrotalcite-like minerals, and possibly M-S-H in the case of $MgSO_4$ exposure. NC solution was selected as a means of forming carbonates independent of the pH depression concomitant with gas phase carbonation. Aging solutions were refreshed at approximately 1 week intervals, at which point the leaching solution was measured for pH and electrical conductivity, vacuum filtered, and analyzed for cation composition using inductively coupled plasma optical emission spectroscopy.

6.3. Reactive transport modeling

6.3.1. Geochemical equilibrium modeling

LeachXS/Orchestra (LXO) [63] is a geochemical speciation mass transport solver that solves equilibrium speciation via Newton-Raphson minimization the system of equations comprised of the laws of mass action and conservation of mass, as detailed in Chapter 2, Section 2.2.3. Conservation of mass is imposed by designating a subset of all possible aqueous species as primary species, p and prescribing the mass of p, M_p [mol] that is assumed to take part in equilibrium chemistry assemblage. Using backscattered electron microscopy coupled with energy dispersive X-ray analysis (Chapter 4), reacted fractions of OPC, FAF, and BFS were estimated for the SVC mortar such that the M_p of each major species may be calculated as

$$M_p = \sum_{q \in Q} \alpha_q \varphi_q x_{q,p} \tag{6.1}$$

where α_q is the degree of reaction of the q^{th} reactive constituent material, φ_q is the mass fraction of the q^{th} phase specified in the mix design, and $x_{q,i}$ [mol] is total mass of the i^{th} component of constituent q. Alternatively, M_p may be obtained from the maximum solubility concentrations measured in the Method 1313 pH-dependent leaching test [189], which are herein referred to as “availabilities” of primary species.

Stability constants were obtained for aqueous species known to be important for geologic media and are presented in Appendix A, as described in Chapter 2. The solid phases modeled in this study are typical of those used in the modeling the hydration of Portland cements, and their stability constants are provided in Table 6.4. Notably, the precipitation of calcium silicate

hydrate (C-S-H) was modeled using the ideal solid solution model with Tobermorite-like and Jennite-like end-members proposed in [166]. The layered double hydroxide phases commonly employed in hydration modeling have been omitted from the present modeling, as it was found that the inclusion of the M_4AH_{10} hydrotalcite-like phase, either as a pure phase or as a solid solution end-member, resulted in the underestimation of Mg solubility by two orders of magnitude near the own pH of the material. Brucite, however, was found to yield a very close prediction of Mg solubility. As described in Chapter 5, kaolinite is a solid phase not normally found in Portland cements, but its inclusion in the partial equilibrium assemblage led to an improved pH-dependent description of Al solubility, particularly at low pH. Also described in Chapter 5 is that the uptake of Al into C-S-H (C-A-S-H) is likely an important factor for describing the blended SVC chemistry. Do to the lack of thermodynamic stability parameters for C-A-S-H, the partial equilibrium mass of Al was, therefore, heuristically adjusted prior to each equilibrium calculation; eighty percent of every mole of Si is assumed to form C-S-H, and 0.17 moles of Al per mole of C-S-H are assumed to form C-A-S-H. Therefore, the Al content in partial equilibrium is that specified either by reacted fractions or availabilities less 0.136 moles of Al per mole of Si specified.

Table 6.4: The solid species considered in the model, along with Gibbs free energies of formation [kJ/mol] and molar masses [g/mol], as reported in [a] Matschei et al. [190]; [b] Lothenbach and Winnefeld [72]; [c] Faure [73]. Parenthetical suffixes denoted amorphous (am), crystalline (cr), and microcrystalline (mcr) phases.

Solid phase	ΔG_f	Molar mass	Solid phase	ΔG_f	Molar mass
$Al(OH)_3$ (am) [a]	-1143.21	78.01	Calcite [a]	-1129.18	100.09
Brucite [a]	-832.23	58.31	CSHi - $C_2S_{2.4}H_4$ [b]	-4370.5	328.41
C_2ASH_8 [a]	-5705.15	418.32	CSHi - SiO_2 (am) [a]	-848.9	60.09
C_3AH_6 [a]	-5010.09	378.26	CSHii - $C_{0.83}SH_{1.3}$ [a]	-1744.36	130.83
$C_4Ac_{0.5}H_{12}$ [a]	-7335.97	564.43	CSHii - $C_{1.67}SH_{2.1}$ [a]	-2480.81	191.37
C_4AcH_{11} [a]	-7337.46	568.43	$Fe(OH)_3$ (mcr) [a]	-711.61	106.87
C_4AH_{13} [a]	-7326.56	560.44	Gypsum [a]	-1797.76	172.17
C_4AsH_{12} [a]	-7778.5	622.49	M_4AcH_9 [a]	-6580.15	469.30
$C_6Ac_3H_{32}$ [a]	-14565.6	1146.92	Magnesite [c]	-1030.6	84.31
$C_6As_3H_{32}$ [a]	-15205.9	1255.08	Portlandite [a]	-897.01	74.08
CAH_{10} [a]	-4622.39	338.19	Syngenite [a]	-2802.74	328.42

6.3.2. Mass transport modeling

Solving the reactive transport problem was achieved in LXO using a sequential, non-iterative operator-splitting approach [51], which entails solving first for local equilibrium at each node and then transporting each species, as described in Chapter 2. Solute flux is assumed to proceed according to the Fickian model such that the change in mass of primary species p in a porous medium is given by the divergence theorem as

$$\frac{\partial C_p}{\partial t} = \nabla\left(\tau D_p \nabla C_p\right) \tag{6.2}$$

where $C_p(x,t)$ [mol/m^3] is the porewater concentration of p in the aqueous phase as function of time t [s] and spatial dimension x [m], τ is the scalar-valued tortuosity coefficient (≤ 1) [m/m], and D_p [dm^2/s] is the diffusion coefficient of the component p in bulk solution. Transporting component species p as opposed to each individual species implies that every species composed of p diffuses at the same rate. For simplicity of computation, the values of D_p were taken identically for each p as 2.385×10^{-9} [m^2/s], which was demonstrated in Chapter 2 to produce a

response near the mean rate of migration predicted the Nernst-Planck transport model for solutions typical of cement porewaters.

For the 1-D diffusion regime dictated by the sample geometry, the boundary condition on the right is specified by the zero-flux condition:

$$\tau D_p \frac{\partial C_p}{\partial x} = 0 \, , x = a, t > 0 \tag{6.3}$$

where a is the length of the specimen [m]. On the left, the finite bath condition is given by

$$V_{tank} \frac{\partial C_p}{\partial t} = \tau A_{surf} D_p \frac{\partial C_p}{\partial x} \, , x = 0, t > 0 \tag{6.4}$$

where V_{tank} is the volume of the external solution or tank [m^3], A_{surf} is the surface area of the specimen [m^2], and $x = 0$ specifies the location of the solution-specimen interface. Due to the well-mixed assumption, the concentration p at $x = 0$ is both the concentration at the surface of the porous medium and the concentration of the tank. The solid domain, that is $0 \leq x \leq a$, was divided into 21 nodes using a geometrically increasing node spacing with a 0.75 mm minimum node spacing in order to meet the requirements of the local equilibrium assumption [48]. The simulation timestep was set to a value of 100 s for the first three hours after refresh of the tank solution in order to improve accuracy of the FD scheme; otherwise, a constant timestep of three hours was used.

6.4. Results

6.4.1. Reacted fractions and availabilities

As described in Chapter 4, the reacted fractions of OPC, FAF, and BFS were determined to be 100%, 36%, and 83% reacted, respectively, using BSE-EDX analysis. The values of input primary species masses for equilibrium modeling, M_p, determined through Eq. (6.1) are given in Table 6.5. Also shown in Table 6.5 are the availabilities of primary species as determined by the maximum soluble concentrations measured in the Method 1313 leaching protocol [2].

Table 6.5: Masses of the primary species, M_i, used as input for equilibrium modeling, expressed in units of moles per kg of dry solid.

Component	Reacted Fraction	Availability
CO_3	0.0387	0.0022
Na	0.0147	0.0073
Mg	0.2502	0.2480
Al	0.3629	0.2229
Si	1.028	0.5755
SO_4	0.0622	0.0243
Cl	$1.454(10^{-3})$	$3.393(10^{-4})$
K	0.0428	0.0368
Ca	1.120	0.9003
Fe	0.0869	0.0257
Ca/Si	1.09	1.56
Al/Si	0.36	0.39

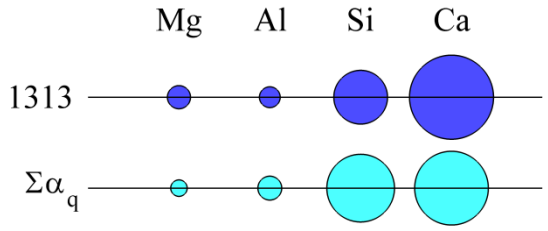

Figure 6.1: Graphical representation of the molar proportions of major primary species participating in the partial equilibrium assemblage as predicted by the availability from Method 1313 ("1313") and from the sum of reacted fractions as measured in Chapter 4.

Fig. 6.1 illustrates the proportions of Mg, Al, Si, and Ca measured by the two techniques relative to one another. The M_p are quite similar for the shown primary speciess; the Method 1313 availabilities indicate higher amounts of Mg and Ca in the partial equilibrium assemblage than those determined via BSE-EDX analysis which may reflect an incongruent reaction of FAF and BFS particles given that Al and Si may be kinetically controlled in certain media.

The sensitivity of primary species' solubilities to M_p is difficult to gauge *a priori* because the predicted solubilities will only change when the stable mineral assemblage changes, that is, when a different stoichiometric reactant becomes limiting for at least one solid phase. Therefore, the chemical response of the system as a function of varying extent of reaction is discussed next.

6.4.2. Geochemical equilibrium modeling

To address the uncertainties in the measurements of reacted fraction in Chapter 4 and to understand better the behavior of the thermodynamic model, the parameters α_{BFS} and α_{FAF} were varied over the intervals [0.6,1.0] and [0.0,0.8], respectively, using a Latin hypercube sampling (LHS) design of experiments [139]. A total of 100 model runs were computed with varied α_q, and modeling outputs were compared to the results of the Method 1313 pH-dependent leaching test at four equivalent base additions of -1.8 [meq/gram] to 0.68 [meq/gram] corresponding to pH points spanning the range of pH 8.7 to 13.0 as listed in Table 6.3. Shown in Fig. 6.2a is the pH response as a function of acid or base addition with continuous simulation between the experimental points at which the residual was calculated. The curve in Fig. 6.2a labeled "RF" corresponds to the thermodynamic response calculated with reacted fractions of $\alpha_{FAF} = 0.20$ and $\alpha_{BFS} = 0.83$ whereas the curve label "1313" shows the same calculation performed using primary species masses calculated using availabilities from Method 1313. Shown in Fig. 6.2b is a contour plot of the mean error computed at all 100 sample points. Unsurprisingly, the pH response is much more sensitive to the reacted fraction of FAF than BFS because FAF constitutes more than twice the total mass of BFS specified in the mix design. The rectangular region highlighted in Fig. 6.2b is centered on the mean values of α_{BFS} and α_{FAF} and spans one standard deviation to either side of the mean. The band of minimum pH residuals situated at approximately on $\alpha_{FAF} = [0.01,0.22]$ is encompassed this "uncertainty region" although it is relatively far from the mean measured value of α_{FAF}. Additionally, annotated on the intensity scale of Fig. 6.2b is the mean error computed when using M_i computed from Method 1313 in lieu of reacted fraction quantities and the same thermodynamic parameters.

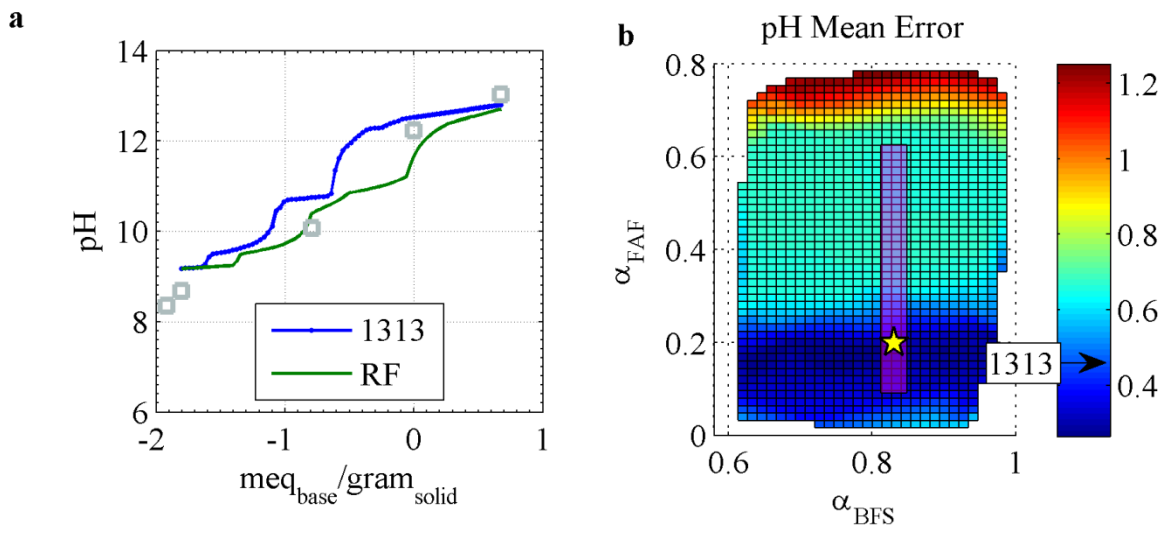

Figure 6.2: a) The response of system pH in both simulation (blue and green lines) and experiment (gray boxes) as a function of milliequivalents of base added per gram of solid material. "1313" denotes the simulation wherein M_i was determined through Method 1313 availability measurement and "RF" denotes the determination of M_i through the reacted fraction BSE-EDX analysis. b) Contour plot of the mean error in pH computed from comparison of model responses to pH-dependent batch leaching as a function of varied reacted fractions. The magnenta rectangle is centered on the measured values of α_{BFS} and α_{FAF} and spans two standard deviations in those measurements, as determined in Chapter 4. The text label "1313" indicates the mean error predicted when the availabilities measured from Method 1313 are used in lieu of the reacted fraction quantities. The yellow star indicates the reacted fractions of $\alpha_{BFS} = 0.83$ and $\alpha_{FAF} = 0.20$ used for calculation of pH in a).

Presented in Fig. 6.3 are the mean errors computed for the primary species Ca, Si, Mg, and Al. Errors have been calculated in base 10 logarithms in order to scale relative solubilities to a more comparable range. Thus, a mean error of one corresponds to an order of magnitude difference in prediction and experiment. Similar to pH, the mean errors of Ca, Si, Mg, and Al are highly correlated to α_{FAF}. Interestingly, the minima for the primary species present in Fig. 6.3 do not necessarily coincide with the minima for pH. The region of minima for Ca (Fig. 6.3a) are banded at a slightly higher value of α_{FAF} than was pH, whereas the Mg minima are nearly coincident with the minima for pH, a correlation that is likely a result of the sensitivity of Mg solubility to pH. The responses of Al and Si are also highly correlated with the exception that the region of minima for Al is bounded for low values of α_{FAF} whereas Si is not.

Figs. 6.4a and 6.4b illustrates the contour plots of Na and K errors, respectively. Both primary species tend to decrease with decreasing α_{FAF}, primarily, although the concentrations of Na

depend upon α_{BFS} as well. Because no solid phase reactions are specified for Na and K, the trends in Fig. 6.4 are a direct reflection the extent of reaction. Also shown in Fig. 6.4 are the measured availabilities of Na and K; since the availabilities are generally lower than the reacted fraction amounts, the mean error observed using available concentrations is generally lower, which suggests an omitted mechanism of alkali uptake in the thermodynamic description.

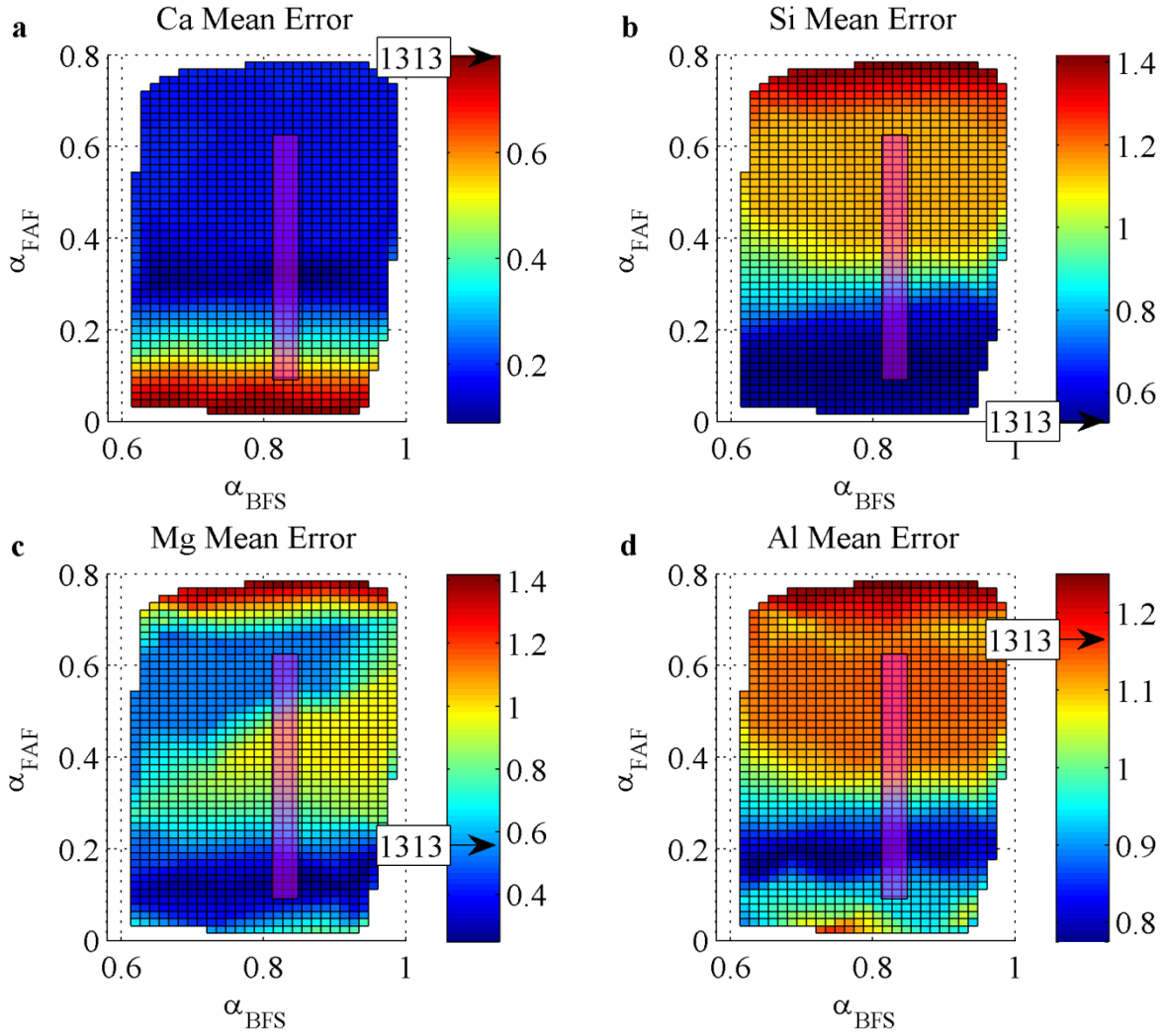

Figure 6.3: Contour plots of the mean errors in major primary species computed from comparison of model responses to pH-dependent batch leaching. The magenta rectangle delineates the BSE-EDX measurements of α_{BFS} and α_{FAF} ± one standard deviation, as measured in Chapter 4. The arrow labeled "1313" corresponds to the error computed by defining component masses with availabilities measured via Method 1313.

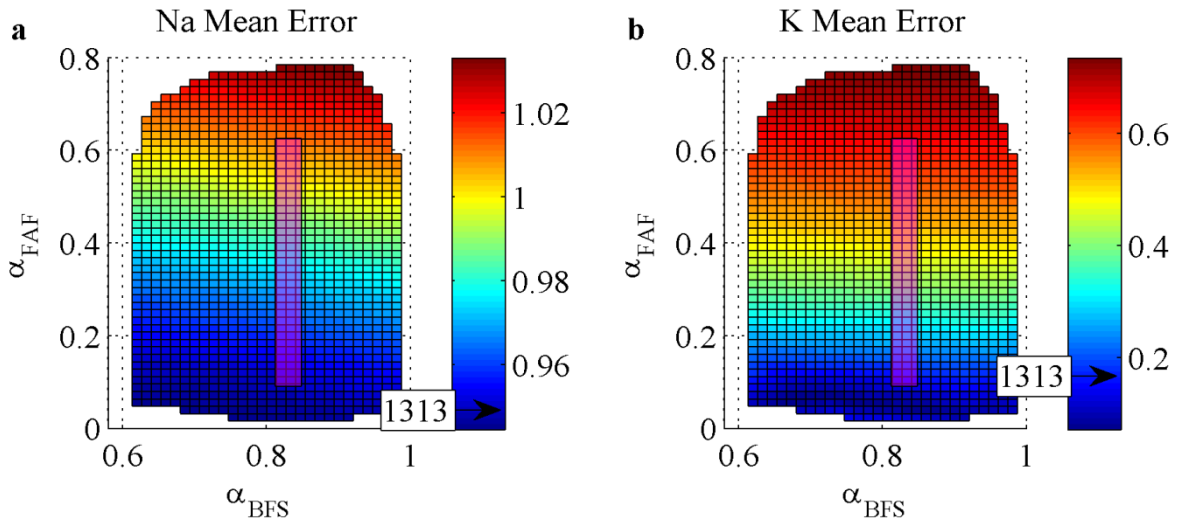

Figure 6.4: Contour plots of the mean errors in alkali primary species computed from comparison of model responses to pH-dependent batch leaching. The magenta rectangle delineates the BSE-EDX measurements of α_{BFS} and α_{FAF} ± one standard deviation, as measured in Chapter 4. The arrow labeled "1313" corresponds to the error computed by defining component masses with availabilities measured via Method 1313.

Examination of Figs. 6.2-6.4 indicates that the region near $\alpha_{BFS} = 0.83$ and $\alpha_{FAF} = 0.20$ contains near-minimal values for the considered primary species and also lies within the uncertainty region of measured reacted fractions. Therefore, the composition of $\alpha_{BFS} = 0.83$ and $\alpha_{FAF} = 0.20$ was chosen as a reasonable approximation of the mass of the partial equilibrium assemblage for subsequent mass transport modeling.

The results of pH-dependent modeling and experiment for Ca, Si, Mg, and Al are depicted in Fig. 6.5. Also shown are the results of the pH dependence test using available M_i measured in Method 1313. The general trends between the two methods of determining M_i are very much the same; the simulation of Mg is nearly identical between the two methods, and the predictions are within an order of magnitude of the experimental values. Al and Si are better predicted with availabilities above pH of approximately 11, and in the case of Al, the difference is nearly an order of magnitude. This result may be indicative of over-estimation of the reacted fractions in Chapter 4 in conjunction with an incongruent reaction of the FAF and BFS materials. The reacted fraction prediction of Ca solubility lies closer to the measured values, and the reason for this may be the higher Ca/Si ratio for the availability measurements.

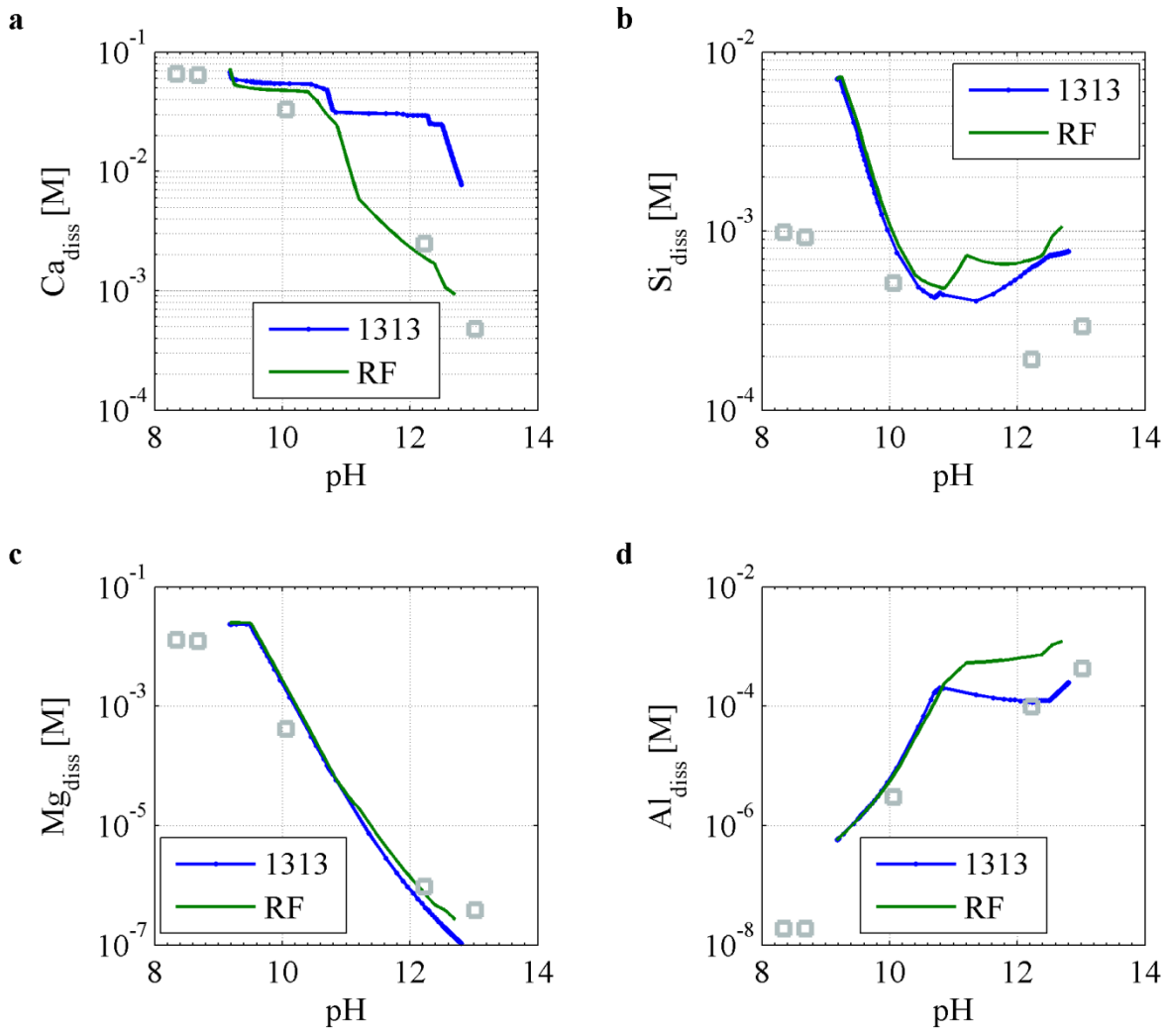

Figure 6.5: Experimentally measured values (gray squares) of component solubility from the Method 1313 leaching protocol and geochemical equilibrium modeling results using both availabilities ("1313") and reacted fractions ("RF").

Overall, neither model attains the full range of measured pH values as a result of acid and base addition, but the agreement between model and prediction is fairly good in the vicinity of the own pH of SVC. It is anticipated that the development of a C-A-S-H solid solution model may greatly improve the description of both Al and Si, as the *ad hoc* approach to mimic C-A-S-H stoichiometry resulted in improved model predictions.

6.4.3. Tortuosity determination

Tortuosity is a necessary parameter for modeling diffusive transport (Eq. 6.2) but, unfortunately, is not directly measurable. A non-reacting species could be used to calibrate the tortuosity to experimental data, but in cementitious materials, even species with characteristically high solubilities may interact with the solid material. Such behavior is suspected in the case for alkalis, which are known to be adsorbed by and substituted in synthetically prepared C-S-H [118] and C-A-S-H [119, 191]. Recently, Chappex and Scrivener [192] reported no significant influence of alumina substitution on the uptake of alkali in "real blended pastes"; however, their study focused on silica fume and metakaolin blends with Ca/Si ratios of the C-S-H in the range of 1.5. In a seminal work by Hong and Glasser [119], the alumina incorporated into C-S-H with Ca/Si of 1.5 was found to have little impact on the sorptive capacity of synthetic gels. Chappex and Scrivener cited this result as evidence of that Al incorporation into C-S-H does not substantially lower the alkalinity of pore waters. However, in the same study by Hong and Glasser, it was found that for gels with Ca/Si of 0.85, the C-A-S-H uptake of alkalis was an order of magnitude higher than that of the equivalent C-S-H paste. Codina et al. [193] found that in 12 month old blended pastes with Ca/Si ratios near 1.0, the alkali concentrations in expressed pore solution were on the order of 10^{-3} M as compared to approximately 0.1 M for a PC paste with comparable initial alkali content. Moreover, the decrease in porewater alkalinity was found to decrease with curing time. In the present study, the calculated Ca/Si of the C-S-H is approximately 0.86, which is very close to the lowest synthetic gel studied by Hong and Glasser. The replacement levels of OPC with slag and fly ash are also similar to those of the study in [193]. Therefore, it seems possible that in the 30-month aged SVC material, a significant level of alkali binding occurs. Furthermore, the possibility of alkali uptake in clay minerals cannot be completely ruled out given the findings in Chapter 5.

Because no mechanisms for alkali adsorption have been considered in the present geochemical model and no alkali-bearing minerals are predicted to be stable in the unperturbed material, the entirety of the Na and K primary species are present as dissolved species. Therefore, to find parameter values which describe the release of Na and K, a Latin hypercube sampling (LHS) scheme was carried out in order to efficiently vary across the parameter space both tortuosity and Na and K input component concentrations, Na_0 and K_0 [M], respectively,. Alkali concentrations

were varied from 0.1% to 110% of their estimated values from the SEM-EDX analysis of Chapter 4, a range which also encompasses their measured availability from Method 1313. Using LHS, 500 sample points were chosen, which for a 3-dimensional problem conforms to the rule of thumb for LHS that the number of points should be ten times greater than the number of dimensions [194]. Mean squared error (MSE) residuals were computed by comparing the base 10 logarithms of simulated concentrations to the experimentally measured concentrations for the DI water monolith leaching case.

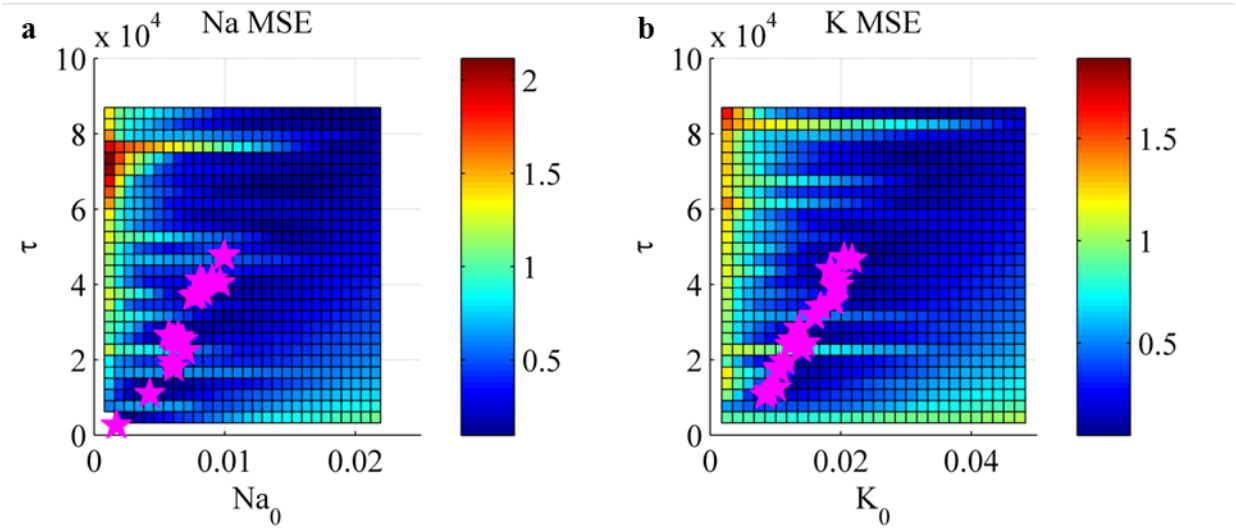

Figure 6.6: Mean squared errors computed from comparison of simulation and experimental data for the DI leaching case. Shown are a) Na MSE as function of initial Na and tortuosity, b) K MSE as a function of initial K and tortuosity. Magenta pentagrams indicated the 20 lowest residuals computed for each ion.

As shown in Fig. 6.6, a diagonal band of minima is apparent for linear combinations of τ and initial concentration variations. As a simplification, it is assumed in this work that the adsorption isotherm reported in [119] may be represented as

$$S_i = RC_i + b \tag{6.5}$$

where S_i [mol_{ads}/L_{sol}] is the sorbed portion of constituent i, R is the retardation factor [-], and b is a fitting parameter [mol_{ads}/L_{sol}]. Eq. (6.5) implicitly assumes that the adsorption isotherm is independent of the liquid-to-solid ratio of the system, and the retardation, and the retardation factors calculated in this manner range between approximately 0.4 and 2.5 for both alkalis. These

values of R seem insufficient *per se* to explain a reduction in porewater alkalinity by two orders of magnitude found in [193]. It is, therefore, concluded, that more fundamental research is needed for describing alkali uptake. Whereas an isotherm could be constructed to fit model alkali uptake in the present material, based upon the results in Fig. 6.6 it seems likely that a semi-infinite number of isotherms parameters may be yield approximately the same response. Therefore, two limit cases are chosen for examination: $\tau = 500$ and $\tau = 60{,}000$. The first proposed value of tortuosity corresponds to a reasonable estimate of the lower limit given that the SVC material had aged for 30 months at the time of testing and it is generally accepted that the addition of pozzolanic materials leads to porosity refinement. The second value corresponds to the tortuosity value assuming all of the alkalis are present in dissolved form. In both cases, a value of initial alkali was roughly fit to the system response. As demonstrated in Fig. 6.7, a slightly better prediction of the alkali release in the DI water case could be achieved using a lower tortuosity value. However, as shown in Fig. 6. 8, the release of precipitating primary species is largely insensitive to the value of tortuosity. Moreover, the pH of the tank solution (Fig. 6.9) is relatively unchanged by the value of tortuosity, as well. This observation is not intended to negate the importance of tortuosity in describing the physical evolution of cementitious materials nor does it discount the relative impact of tortuosity in long time frames, but for the purposes of the materials and time frames considered in this study, the value of tortuosity exerts little influence on the overall predictions. Porosity and tortuosity changes induced by mineralogical changes are also like to play a role, but for the remainder of this work, a constant value of $\tau = 500$ has been prescribed.

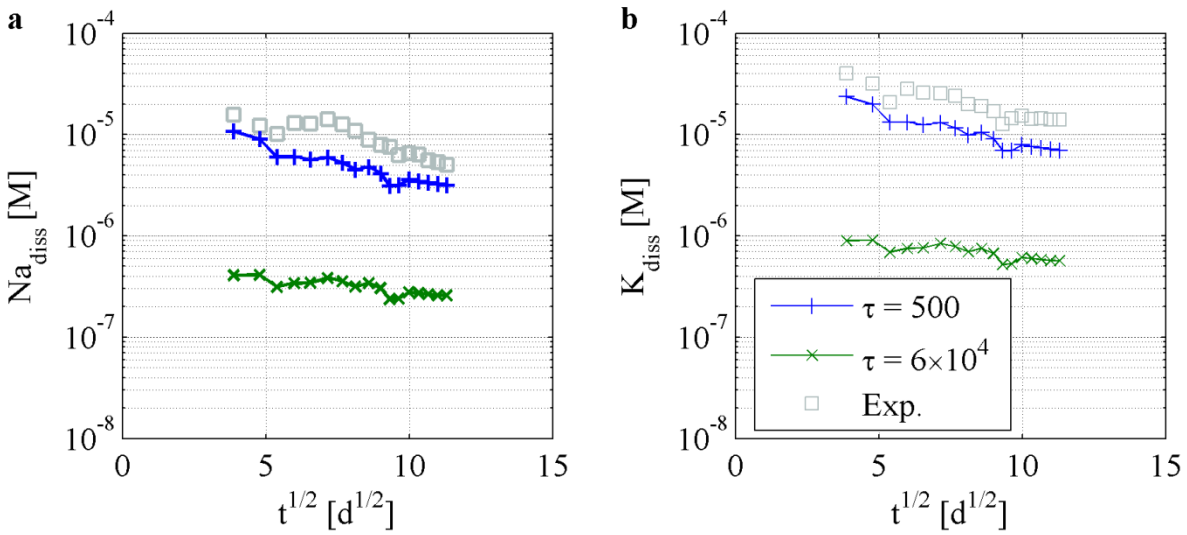

Figure 6.7: Comparison of modeled (blue "+" and green "x") and experimentally measured (gray squares) tank concentrations of alkali ions in the DI water leaching scenario using values of $\tau = 500$ (blue "+" signs) and $\tau = 60{,}000$ (green "x"). Lines connecting data points do not represent interim concentration values; they are simply present to guide the eye.

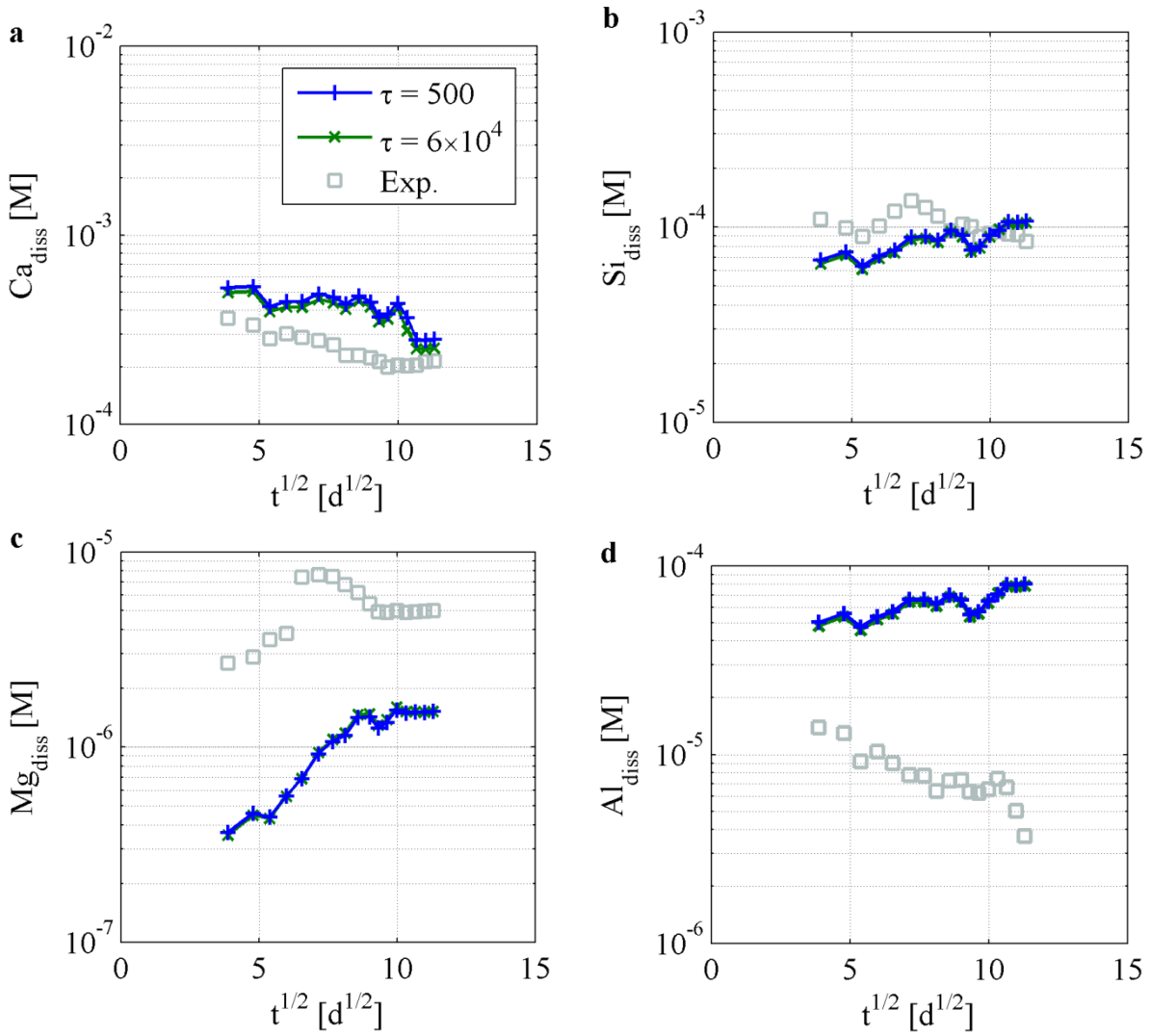

Figure 6.8: Comparison of modeled (blue "+" and green "x") and experimentally measured (gray squares) tank concentrations of major ions in the DI water leaching scenario using values of $\tau = 500$ (blue "+") and $\tau = 60{,}000$ (green "x"). Lines connecting data points do not represent interim concentration values; they are simply present to guide the eye.

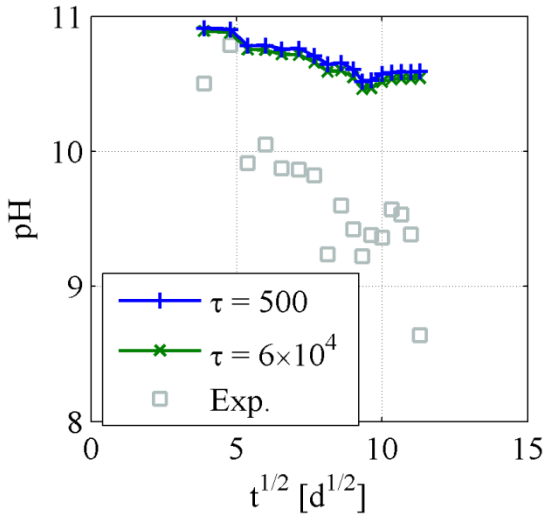

Figure 6.9: Comparison of modeled (blue "+" and green "x") and experimentally measured (gray squares) tank pH in the DI water leaching scenario using values of $\tau = 500$ (blue "+") and $\tau = 60{,}000$ (green "x"). Lines connecting data points do not represent interim concentration values; they are simply present to guide the eye.

6.4.4. SVC leaching

Results of the four accelerated aging cases outlined in Section 2.3 are presented together in this section in order to facilitate comparisons between them. Because no explicit mechanism for alkali adsorption was modeled, the predicted releases of K are essentially the same for all four scenarios. In Fig. 6.10, however, it is apparent that the measured release of K is roughly an order of magnitude lower in the DI leaching scenario than in the other three; a possible explanation is that K^+ bound within the C-S-H phases is displaced by the intruding cations. Such behavior is expected from intruding Na^+ ions which may participate in adsorption and cation exchange reactions in a manner similar to K^+. On the contrary, the divalent Mg^{+2} ion is unlikely to substitute for K^+, yet the releases of Na and K are higher in the MS leaching case than in the DI case. The formation of magnesium silicates, namely magnesium-silicate-hydrate (M-S-H) [179, 195], may explain this higher alkali release, as it is conceivable that the reconfiguration of silica into magnesium silicates liberates alkalis from the gel phase.

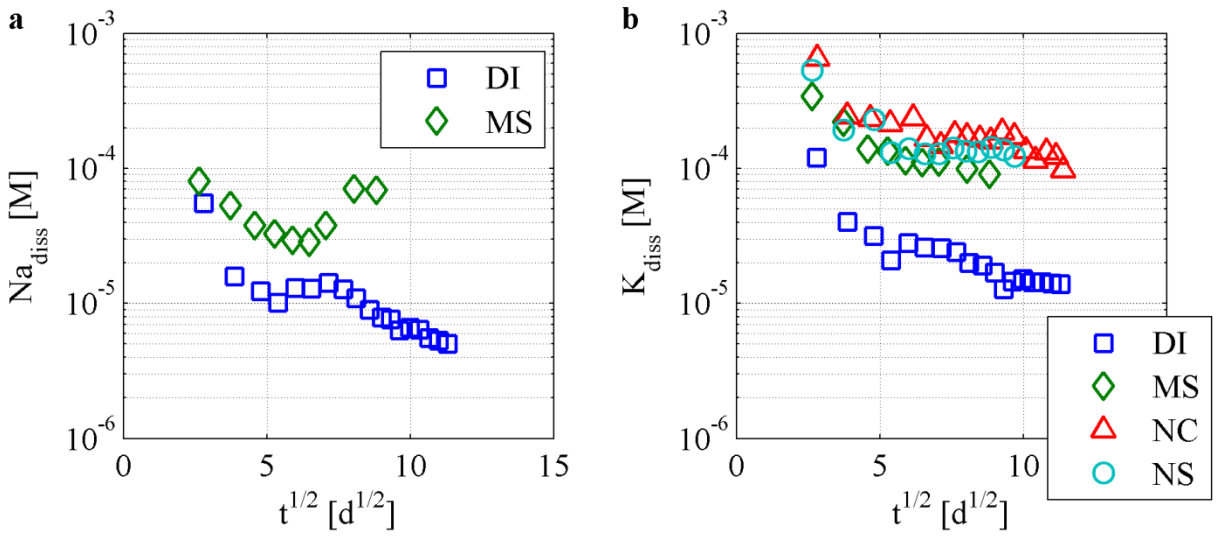

Figure 6.10: Experimentally measured (open symbols) tank concentrations of a) Na and b) K as a function of the square root of leaching time for the four leaching cases.

Further suggestion of the presence of M-S-H in the MS case is apparent in the release of Si (Fig. 6.11b); for the cases of DI, NC, and NS leaching (Fig. 6.11), the prediction of Si release matches the data fairly closely, which may be taken as an indication that the CSHii solid solution model is reasonable for describing Si release in a system that almost assuredly contains Al-substituted C-S-H [173-175, 196, 197]. In the MS case, however, the Si release is overpredicted by approximately 3 orders of magnitude and diverges from the experimental trend. One possible explanation is that Si solubility is being suppressed by an M-S-H phase; an alternative is that the formation hydrotalcite-like phases and ettringite tend to remove Al from the C-A-S-H structure, leading to stronger affinity for Si in the gel phase.

As shown in Fig. 6.12, Al release is overestimated for the DI and NS cases by generally less than an order of magnitude, a difference which may attributable to the lack of a thermodynamic description of C-A-S-H. Examination of the Al release in Fig. 6.12b and the Mg uptake in Fig. 6.13b for the MS case suggest that the hydrotalcite-like phases (M_4AH_{10}) [198, 199] should be stable under these conditions. As discussed in Section 3.1, the hydrotalcite-like phases have been omitted from consideration due to their poor description of the equilibrium solubility of Mg. This discrepancy may be due in part to the fact that the stability constants ascribed to the hydrotalcite-like phases are tentative values [190] and due to a possible kinetic control on Mg [200].

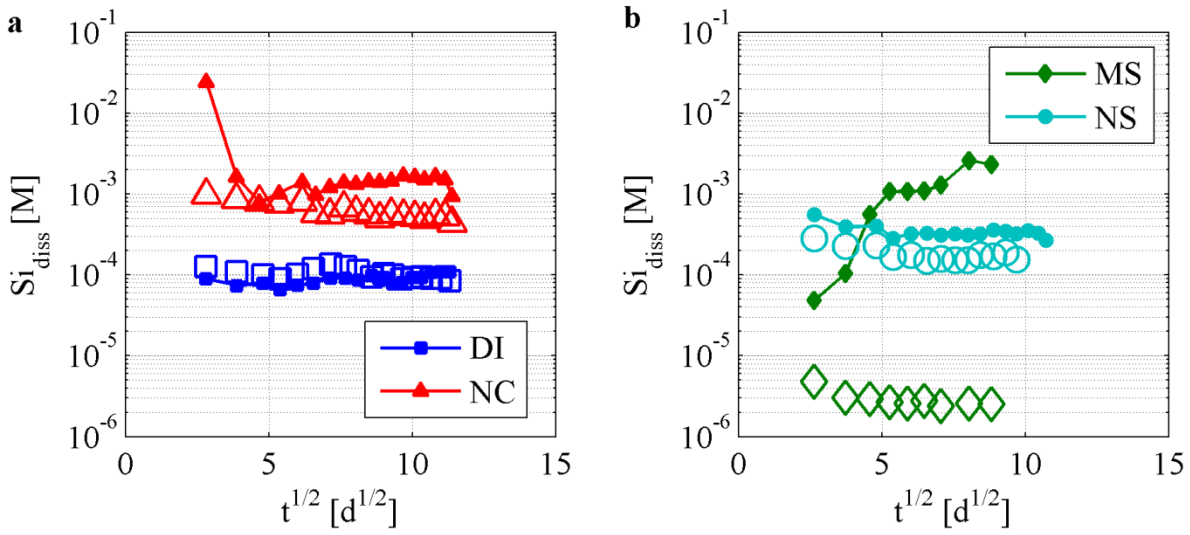

Figure 6.11: Experimentally measured (open symbols) and simulated (filled symbols) tank concentrations of Si as a function of the square root of leaching time for a) DI and NC leaching and b) MS and NS leaching.

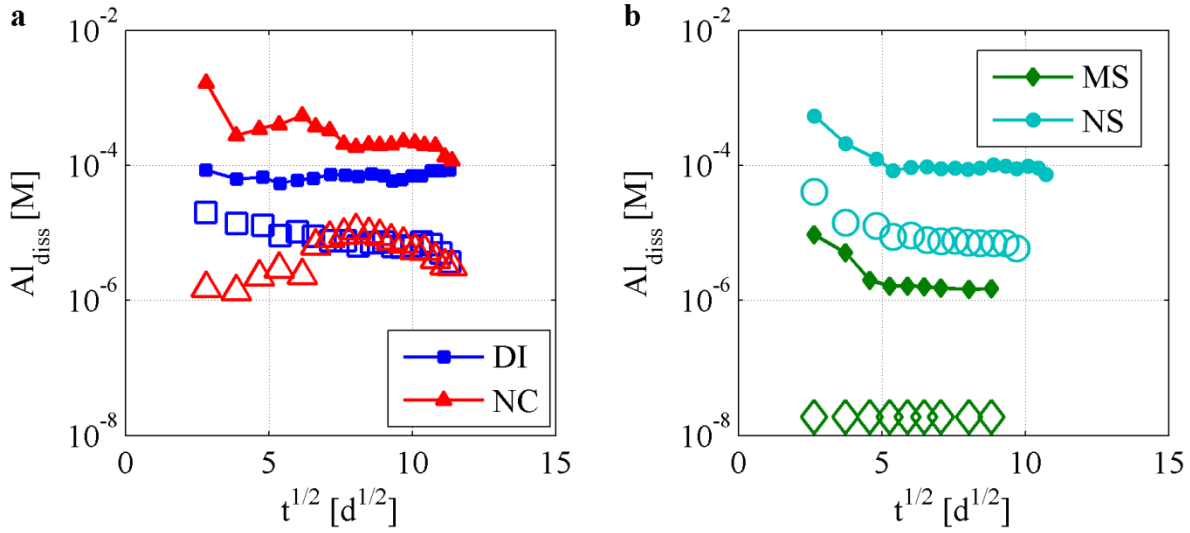

Figure 6.12: Experimentally measured (open symbols) and simulated (filled symbols) tank concentrations of Al as a function of the square root of leaching time for a) DI and NC leaching and b) MS and NS leaching.

As illustrated in Fig. 6.13, Mg release is generally predicted to within an order of magnitude of the measured value. The exception appears in the NC leaching case (Fig. 6.13a)

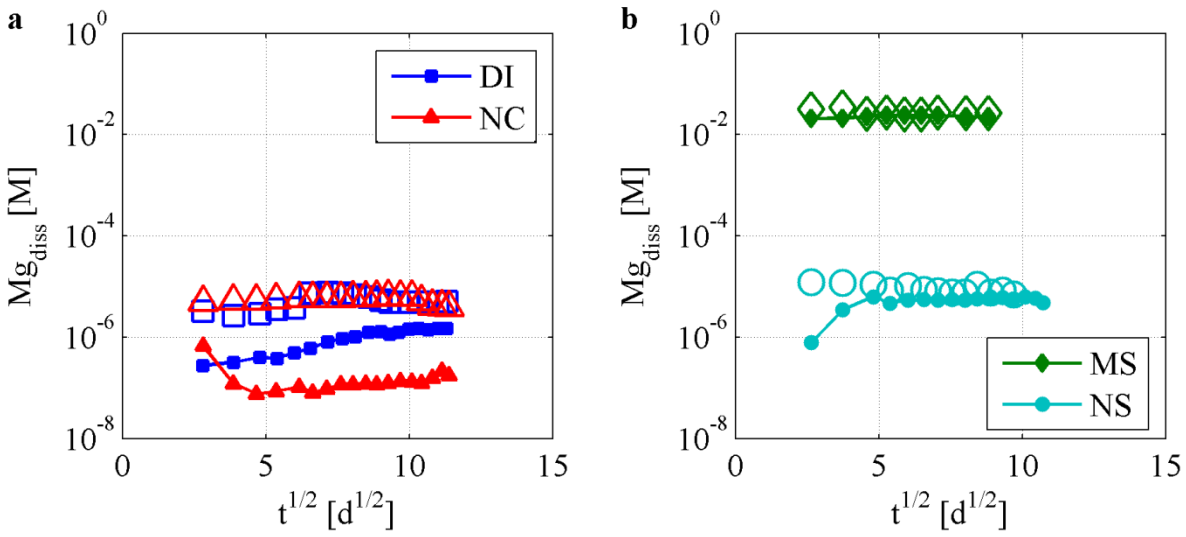

Figure 6.13: Experimentally measured (open symbols) and simulated (filled symbols) tank concentrations of Mg as a function of the square root of leaching time for a) DI and NC leaching and b) NS leaching.

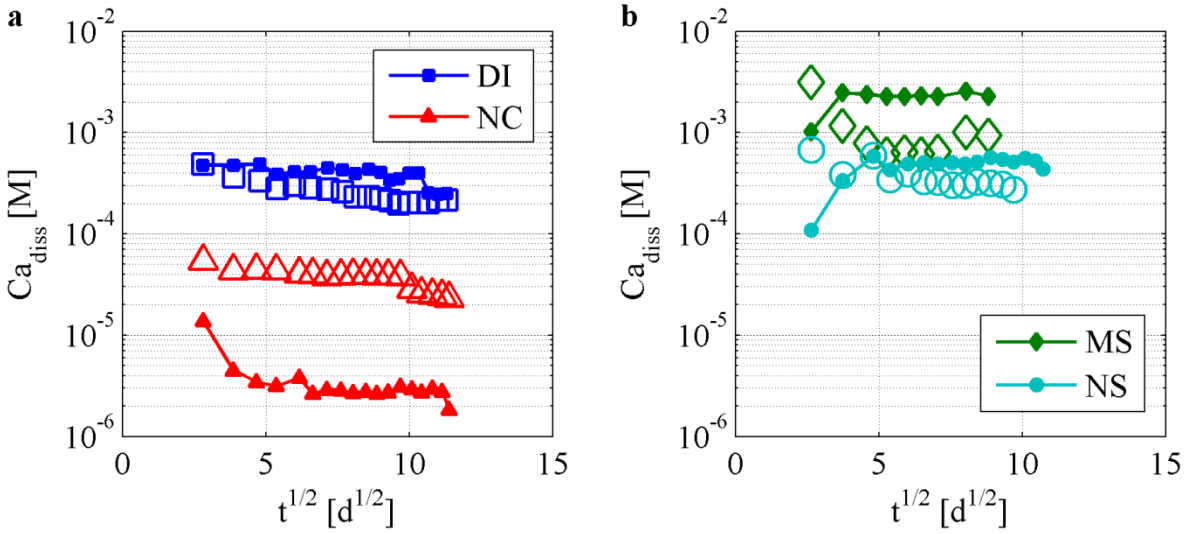

Figure 6.14: Experimentally measured (open symbols) and simulated (filled symbols) tank concentrations of Ca as a function of the square root of leaching time for a) DI and NC leaching and b) MS and NS leaching.

As is the case with Mg, Ca (Fig. 6.14) release seems to be generally well described by the reactive transport model presented herein. The notable exception is the case of NC leaching, for which an order of magnitude difference between prediction and experiment is observed. The

enhanced release of Ca in the MS and NS cases seems to be more or less captured by the prediction.

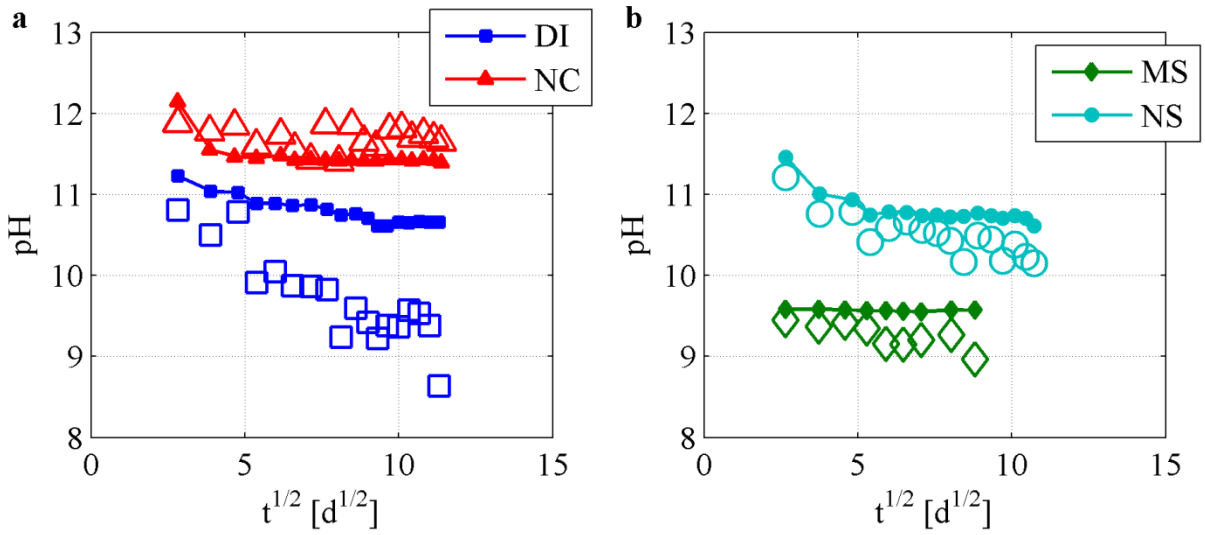

Figure 6.15: Experimentally measured (open symbols) and simulated (filled symbols) values of tank pH as a function of the square root of leaching time for a) DI and NC leaching and b) MS and NS leaching.

The prediction of tank pH illustrated in Fig. 6.15 is fairly consistent for all four leaching solutions with the exception of the DI leaching case. That measured pH is typically lower than predicted may be indicative of a systematic bias in the pH measurement due to atmospheric carbonation, but an alternative hypothesis not addressed in this work is that soluble reduced sulfur species may be present in anionic form such that hydroxide concentrations are suppressed in the SVC porewater.

6.5. Conclusions

The variation of measured reacted fraction values and comparison to pH-dependent batch leaching tests suggest that the resulting partial equilibrium assemblage yields reasonable descriptions of major constituent solubilities. In general, predictions of constituent uptake and release in response to external aging conditions suggest that the thermodynamic model developed primarily for Portland cements likely describes many of the mechanisms controlling constituent solubility. The NC leaching case seems to be the least well-described of the four

examined herein, but given the higher ionic strength of the NC solution, there exists the distinct possibility that the charge-coupling effects described in Chapter 2 may become significant for this case. The thermodynamic description of Al-bearing calcium silicate hydrate and a more coherent description of hydrotalcite phases have been identified as areas of research likely to lead to significant improvements of reactive transport model predictions of blended cements. Furthermore, a deeper understanding of the phenomena responsible for alkali uptake and retention may prove beneficial to the improvement of long-term performance assessment.

CHAPTER 7

7. CONCLUSIONS AND FUTURE WORK

This dissertation thesis has investigated the uncertainties inherent in long-term reactive transport models of blended cement performance. Facets of the reactive transport process have been isolated, when possible, in an effort to elucidate the origins of uncertainties and to suggest paths toward reducing uncertainties. The conclusions of this effort are summarized as follows.

Chapter 2 explored the subject of mass transport by comparing the Fickian and Nernst-Planck (NP) models of mass transport The research compared the results and implications of the Fickian and NP models as well as the parameterization of transport parameters for the the Nernst-Planck equation. The result was that the extent of differences between the two models depended greatly on the composition of the external leachant considered. Differences in Fickian and NP transport predictions are likely enhanced by the presence of multiple major species; in the NP transport model, the combined effect of varied diffusion coefficients and the interaction of Coulombic forces among ions led to different predictions than the Fickian model of concentration profiles in cases where multiple ions were present in high concentrations. However, when only one or two major ions were present in solution, maintaining electroneutrality was, in a sense, “easier” to accomplish. Naturally, these effects cannot be completely divorced of the choice of the chemical reaction model accompanying the transport simulations. A second main conclusion drawn from research is that any differences due to the choice of transport model may in fact be exacerbated by the chemical description of solid and aqueous phase speciation and liquid-solid partitioning. This is especially true for species whose solubilities are highly dependent on pH; small changes in pH can lead to large changes in a species’ solubility which may dramatically influence its rate of transport. Additional efforts to corroborate these observations could take the form of a sensitivity study that varies ionic diffusion coefficients, cement and leaching solution compositions, and spatial and temporal scales. Such a study would provide a more clear understanding of the conditions under which the Fickian and NP models yield significantly different predictions. This work should also be

supported by transport experiments in which species concentrations are measured both in the external solution and as a function of depth, providing a means of model validation.

A natural extension of exploring the Coulombic interaction of ions in free solution, as in the NP model, is to consider the interaction of free ions with the charged surfaces of the cement pore surfaces. Chapter 3 employed the Poisson-Boltzmann equation to describe the concentrations of free ions in the vicinity of the pore surfaces, that is, the diffuse layer. The full solution of the nonlinear Poisson-Boltzmann equation revealed that using usual and customary simplifying assumptions could lead to significant differences in predicted concentration profiles in small pores. More significantly, it was demonstrated for blended cements, the high proportion of fine pores may influence ionic transport through anionic exclusion. Such an effect may be observable through a comparison of through-diffusion and leaching experiments. In through-diffusion experiments, an anion which is excluded from fine, poorly connected porosity may be observed to be diffuse more rapidly than its companion cation. In leaching experiments, the probability of anions originating in both poorly and well-connected pores is likely more or less uniform; therefore, anion-exclusion effects in such a situation would likely be observed through stronger retention within the matrix of a fraction of the anion species..

Chapter 4 explored the subject of mass conservation within the reactive transport problem. Specifically, a method was developed for measuring the extent of reaction of cement, slag, and fly ash in real blended cement systems. The method utilizes information from both backscattered scanning electron microscopy and energy dispersive X-ray analysis to segment unreacted particles from the surrounding matrix and to then classify those unreacted particles according to type. The method yielded estimates of reacted fractions of fly ash and slag similar to those reported in the literature for less complex blends. Strategies for improving the algorithm were discussed, and future work entails the incorporation of more robust segmentation strategies, the inclusion of data from multiple measurement techniques, and, above all, comparisons to ground-truth phase identification by cement microscopy experts.

The uncertainties associated with the thermodynamic description of the blended cement mortar were investigated in Chapters 5 and 6. In Chapter 5, a set of solid phase stability constants developed for Portland cements were applied straightaway to describe major species' solubilities of a blended cement in a standard batch leaching test. Because the hydration products in

supplementary cements are largely uncharacterized, the question examined in Chapter 5 was whether Portland cement thermodynamic descriptions are able to adequately describe the behavior of blended cement systems. It was discovered that major species' solubilities were generally well described by the Portland cement mineral set, with the notable exception being Al. Some of this deviation may well be explained by the lack of thermodynamic data for Al-substituted calcium silicate hydrate, a phase commonly observed in blended cements, but a possible influential factor on Al-solubility was identified, namely the presence of phyllosilicate minerals. Whereas a substantial portion of the phyllosilicates illite and kaolinite were observed in the fine aggregate fraction of the blended cement, it was also postulated that kaolinite could be formed as an alteration product, based on the estimated saturation index, morphology, and stoichiometry of kaolinite. The inclusion of kaolinite in the thermodynamic model yielded a better description of Al solubility, especially in the pH range of 8 to 10. The next logical step for testing this hypothesis is to attempt to induce the formation of kaolinite in cements free from any other source of kaolinite. Confirmation of the inferred phases using crystallographic techniques is also a necessity for substantiating this observation.

Chapter 6 built upon the work of Chapters 2-5 by examining the reactive transport process in full. Experiments and simulations of the leaching of the blended cement mortar exposed to four distinct external solutions revealed that the use of Portland cement stability constants generally led to a good description of the blended cement leaching. As with the equilibrium experiments, the description of Al release proved to be poor in some cases which may be attributed to a lack of proper thermodynamic constants for some solid phases. Additionally, leaching by magnesium sulfate solution indicated that magnesium silicates may be an important phase for describing the stability of Si in the presence of Mg. Further experimental research is needed to identify the altered phases in the near-surface leached zone which may lead to better thermodynamic characterization of blended cement systems.

Given the myriad of uncertainties addressed in the reactive transport problem applied to blended cementitious materials, it is useful to gauge these uncertainties relative to one another. Of the factors examined herein, the choice of thermodynamic parameters seems to exert the greatest influence on model predictions. However, the close agreement between experiment and simulation using Portland cement parameters is encouraging; an apt set of parameters for

blended cements may only require a few key additions. Compared to the influence of thermodynamic parameters, differences between the Fickian and Nernst-Planck transport models seem minor, but when these differences are coupled with the effects of porosity-tortuosity change, cracking, and other transient behaviors, these differences may be magnified. Coulombic interactions between free ions and surface charges in fine pores have the potential to strongly influence constituent transport; indeed, the charged surfaces of silicon nanofluidic devices are already being exploited for this purpose. Of the factors examined in this work, however, the influence of surface charge and free charge interactions may be most difficult to discern. Finally, the quantification of extent of reaction is important for characterizing both chemical and mechanical properties of blended cement systems, but as demonstrated in Chapter 6, a wide range of reacted fraction values yield broadly similar leaching behaviors. Quantification of reacted fractions does become significant, however, in situations where the total amounts of predicted solid phases are important, for instance, when determining porosity alteration due to mineral dissolution and precipitation reactions or simulating mechanical loading. Thus, no one single factor can be deemed insignificant *a priori*. It has been demonstrated that each of these factors has the potential to lead to significantly different assessments of long-term system performance.

APPENDIX A: THERMODYNAMIC CONSTANTS FOR AQUEOUS SPECIES

Gibbs free energies of formation [kJ/mol] of aqueous species as reported in [a] Matschei et al. [190]; [b] Hummel et al. [71]; [c] Faure [73]; and [d] Shock et al. [74]. Zero superscripts denote neutral species.

Species	ΔG_f	Species	ΔG_f	Species	ΔG_f
$Al(OH)^{+2}$ [a]	-692.6	CO_2^0 [a]	-386	$MgCO_3^0$ [b]	-1000
$Al(OH)_2^+$ [b]	-901.5	CO_3^{-2} [a]	-528	$MgCO_3^+$ [b]	-1048
$Al(OH)_3^0$ [b]	-1105	$Fe(OH)^{+2}$ [b]	-229.2	$MgSiO(OH)_3^+$ [b]	-1717
$Al(OH)_4^-$ [b]	-1302	$Fe(OH)_2^+$ [b]	-446.5	$MgSiO_2(OH)_2^0$ [b]	-1665
$Al(OH)_6SiO^-$ [b]	-2398	$Fe(OH)_3^0$ [b]	-664.3	$MgSO_4^0$ [b]	-1213
$Al(SO_4)_2^-$ [a]	-2006	$Fe(OH)_4^-$ [b]	-829.8	Na^+ [a]	-261.9
Al^{+3} [a]	-483.7	$Fe(SO_4)_2^-$ [b]	-1523	$Na_2SO_4^0$ [c]	-1268
AlO^+ [a]	-660.4	Fe^{+3} [b]	-4.6	$NaCO_3^-$ [a]	-797.1
AlO_2^- [a]	-827.5	$Fe_2(OH)_2^{+4}$ [b]	-466.6	$NaHCO_3^0$ [a]	-847.4
AlO_2H^0 [a]	-864.3	$Fe_3(OH)_4^{+5}$ [b]	-926.3	$NaNO_3^0$ [c]	-373.2
$AlSiO(OH)_3^{+2}$ [b]	-1783	$FeCl^{+2}$ [b]	-144.2	$NaOH^0$ [a]	-418.1
$AlSiO_2(OH)^{+2}$ [a]	-1541	$FeCl_2^+$ [b]	-279.2	$NaSO_4^-$ [a]	-1010
$AlSiO_4^-$ [a]	-1681	$FeCl_3^0$ [b]	-404.7	NH_3^0 [b]	-26.7
$AlSO_4^+$ [a]	-1250	$FeHSO_4^{+2}$ [b]	-840.4	NH_4^+ [b]	-79.4
$Ca(NO_3)_2^0$ [c]	-776.2	$FeSiO(OH)_3^{+2}$ [b]	-1313	NH_4Cl^0 [c]	-210.6
$Ca(OH)^+$ [a]	-717	$FeSO_4^+$ [b]	-771.6	$NH_4NO_3^0$ [c]	-190.7
$Ca(OH)_2^0$ [c]	-868.1	H^+ [a]	0	NH_4OH^0 [c]	-263.8
Ca^{+2} [a]	-552.8	HCO_3^- [a]	-586.9	NO_3^- [b]	-110.8
$CaCO_3^0$ [a]	-1099	HSO_4^- [a]	-755.8	NO_3H^0 [c]	-110.7
$CaHCO_3^+$ [a]	-1146	K^+ [b]	-282.5	OH^- [b]	-157.3
$CaNO_3^+$ [c]	-638.5	$K_2SO_4^0$ [c]	1311	$Si(OH)_4^0$ [b]	-1309
$CaSiO(OH)_3^+$ [b]	-1813	KNO_3^0 [c]	-394.6	$SiO(OH)_3^-$ [b]	-1252
$CaSiO_2(OH)^+$ [a]	-1574	KOH^0 [b]	-437.1	SiO_2^0 [a]	-833.4
$CaSiO_2(OH)_2^0$ [b]	-1756	KSO_4^- [b]	-1031	$SiO_2(OH)^-$ [a]	-1015
$CaSiO_3^0$ [a]	-1518	$Mg(NO_3)_2^0$ [c]	-677.4	$SiO_2(OH)_2^{-2}$ [b]	-1177
$CaSO_4^0$ [a]	-1310	$Mg(OH)^+$ [b]	-627.2	SiO_3^{-2} [a]	-938.5
Cl^- [b]	-131.2	Mg^{+2} [b]	-454	SO_4^{-2} [a]	-744.5

APPENDIX B: THERMODYNAMIC CONSTANTS FOR SOLID SPECIES

The solid species considered in the model, along with Gibbs free energies of formation [kJ/mol] and molar masses [g/mol], as reported in [a] Matschei et al. [190]; [b] Lothenbach and Winnefeld [72]; [c] Faure [73]. Parenthetical suffixes denoted amorphous (am), crystalline (cr), and microcrystalline (mcr) phases.

Solid phase	ΔG_f	Molar mass	Solid phase	ΔG_f	Molar mass
$(NH_4)_2SO_4$ (cr) [c]	-901.9	132.14	$C_6S_2s_2c_2H_{30}$ [a]	-15128.5	1245.22
AFm - C_4AsH_{11} [a]	-7778.5	622.49	$Ca(NO_3)_2$ (cr) [c]	-743.209	164.09
AFm - C_4AsH_{11} [c]	-394.9	101.10	CAH_{10} [a]	-4622.39	338.19
AFm - C_4FsH_{12} [a]	-6882.55	680.22	Calcite [a]	-1129.18	100.09
AFm_c - C_4AcH_{11} [a]	-7337.46	568.43	CSHi - $C_2S_{2.4}H_4$ [b]	-4370.5	328.41
AFm_c - C_4FcH_{12} [a]	-6679.2	644.17	CSHi - SiO_2 (am) [a]	-848.9	60.09
AFm_{hc} - $C_4Ac_{0.5}H_{12}$ [a]	-7335.97	564.43	CSHii - $C_{0.83}SH_{1.3}$ [a]	-1744.36	130.83
AFm_{hc} - $C_4Fc_{0.5}H_{12}$ [a]	-6440.19	622.16	CSHii - $C_{1.67}SH_{2.1}$ [a]	-2480.81	191.37
AFt - $C_6As_3H_{32}$ [a]	-15205.9	1255.08	CSHii - $C_{2.5}S_{3.0}H_{3.9}$ [a]	-5233.08	392.50
AFt - $C_6Fs_3H_{32}$ [a]	-14282.4	1312.81	CSHii - $C_5S_3H_{6.3}$ [a]	-7442.43	574.10
$Al(OH)_3$ (am) [a]	-1143.21	78.01	$Fe(OH)_3$ (mcr) [a]	-711.61	106.87
Brucite [a]	-832.23	58.31	Fe_2O_3 [a]	-739.53	159.70
C_2ASH_8 [a]	-5705.15	418.32	Friedel salt	-5860.96	489.25
C_2FSH_8 [a]	-4809.53	476.04	Gypsum [a]	-1797.76	172.17
$C_2S_{2.4}H_4$ [b]	-4370.5	328.41	Halite [c]	-384.154	58.44
C_3AH_6 [a]	-5010.09	378.26	LDH - M_4AH_{10} [a]	-6394.56	443.30
C_3FH_6 [a]	-4116.29	435.99	LDH - M_4FH_{10} [a]	-5498.84	501.03
$C_4Ac_{0.5}H_{12}$ [a]	-7335.97	564.43	M_4AcH_9 [a]	-6580.15	469.30
C_4AcH_{11} [a]	-7337.46	568.43	M_4AH_{10} [a]	-6394.56	443.30
C_4AH_{13} [a]	-7326.56	560.44	M_4FH_{10} [a]	-5498.84	501.03
C_4AsH_{12} [a]	-7778.5	622.49	Magnesite [c]	-1030.6	84.31
$C_4Fc_{0.5}H_{12}$ [a]	-6440.19	622.16	Magnetite [c]	-979.428	231.55
C_4FcH_{12} [a]	-6679.2	644.17	$Mg(NO_3)_2$ (cr) [c]	-589.5	148.31
C_4FH_{13} [a]	-6430.94	618.16	Na_2SO_4 (cr) [c]	-1270.2	142.04
C_4FsH_{12} [a]	-6882.55	680.22	$NaNO_3$ (cr) [c]	-87.73	84.99
$C_6Ac_3H_{32}$ [a]	-14565.6	1146.92	NH_4NO_3 (cr) [c]	-184	80.04
$C_6As_3H_{32}$ [a]	-15205.9	1255.08	Portlandite [a]	-897.01	74.08
$C_6Fs_3H_{32}$ [a]	-14282.4	1312.81	Syngenite [a]	-2802.74	328.42

APPENDIX C: ESTIMATED DIFFUSION COEFFICIENTS

Estimated ionic diffusion coefficient values D_i^u [10^{-9} m^2/s] and estimated van der Waals volumes V_v [$Å^3$] for ions without reported measurements of D_i^u.

Species	V_i	D_i^u	Species	V_i	D_i^u
$Al(OH)^{+2}$	43.37	1.600	$FeCl_2^{+}$	67.4	1.660
$Al(OH)_2^{+}$	53.25	1.653	$FeCl_3^{0}$	84.24	1.620
$Al(OH)_3$	63.17	1.995	$FeHSO_4^{+2}$	97.81	1.649
$Al(OH)_4^{-}$	73.26	1.287	$FeSiO(OH)_3^{+2}$	106.03	1.652
$Al(OH)_6SiO^{-}$	125.24	1.120	$FeSO_4^{+}$	97.81	1.669
$Al(SO_4)_2^{-}$	143.09	1.091	$K_2SO_4^{0}$	238.56	0.592
AlO^{+}	40.28	1.641	KNO_3^{0}	132.09	1.443
AlO_2^{-}	53.25	1.438	KOH^{0}	94.13	1.747
AlO_2H	50.88	2.093	KSO_4^{-}	151.45	1.080
$AlSiO(OH)_3^{+2}$	106.03	1.652	$Mg(NO_3)_2^{0}$	111.65	1.607
$AlSiO_2(OH)^{+2}$	98.83	1.650	$Mg(OH)^{+}$	36.08	1.635
$AlSiO_4^{-}$	106.03	1.163	$MgCO_3^{0}$	64.53	1.984
$AlSO_4^{+}$	97.85	1.669	$MgCO_3^{+}$	64.53	1.659
$Ca(NO_3)_2^{0}$	123.47	1.512	$MgSiO(OH)_3^{+}$	94.21	1.668
$Ca(OH)^{+}$	48.5	1.649	$MgSiO_2(OH)_2^{0}$	94.21	1.746
$Ca(OH)_2^{0}$	63.49	1.992	$MgSO_4^{0}$	86.03	1.812
$CaCO_3^{0}$	81.16	1.851	$Na_2SO_4^{0}$	162.34	1.201
$CaHCO_3^{+}$	81.16	1.665	$NaCO_3^{-}$	91.84	1.206
$CaNO_3^{+}$	78.49	1.664	$NaHCO_3^{0}$	94.26	1.746
$CaSiO(OH)_3^{+}$	106.03	1.671	$NaNO_3^{0}$	93.98	1.748
$CaSiO_2(OH)^{+}$	94.14	1.668	$NaOH^{0}$	62.06	2.004
$CaSiO_2(OH)_2$	106.03	1.652	$NaSO_4^{-}$	113.34	1.145
$CaSiO_3^{0}$	94.14	1.747	NH_3^{0}	22.86	2.317
$CaSO_4^{0}$	97.85	1.717	NH_4Cl^{0}	47.73	2.118
CO_2^{0}	33.19	2.234	$NH_4NO_3^{0}$	70.26	1.938
$Fe(OH)^{+2}$	44.95	1.603	NH_4OH^{0}	44.79	2.142

Continued from previous.

Species	V_i	D_i^u	Species	V_i	D_i^u
$Fe(OH)_2^+$	56.44	1.655	NO_3H^0	41.94	2.164
$Fe(OH)_3^0$	67.85	1.957	$Si(OH)_4$	72.52	1.920
$Fe(OH)_4^-$	79.3	1.257	$SiO(OH)_3^-$	72.52	1.291
$Fe(SO_4)_2^-$	162.19	1.067	SiO_2^0	49.05	2.108
$Fe_2(OH)_2^{+4}$	84.29	1.597	$SiO_2(OH)^-$	72.52	1.291
$Fe_3(OH)_4^{+5}$	135.09	1.617	$SiO_2(OH)_2^{-2}$	72.52	1.697
$FeCl^{+2}$	50.42	1.612	SiO_3^{-2}	60.63	1.857

APPENDIX D: ANHYDROUS PARTICLE DATABASE OF ELEMENTAL COMPOSITIONS

Elemental compositions [mass percentages] of anhydrous particles considered in phase identification.

Phase	H	O	C	Na	Mg	Al	Si	S	K	Ca	Fe
α-Quartz	0.00	53.3	0.00	0.00	0.00	0.00	46.7	0.00	0.0	0.0	0.0
Illite	0.5	49.8	0.00	0.00	0.8	14.3	26.4	0.00	5.4	0.0	2.9
Kaolinite	1.6	55.8	0.00	0.00	0.00	20.9	21.8	0.00	0.0	0.0	0.0
Mullite	0.00	48.5	0.00	0.00	0.00	40.9	10.6	0.00	0.0	0.0	0.0
FAF_a	0.00	42.1	0.00	0.83	0.90	12.5	18.6	0.7	2.1	1.4	18.5
FAF_b	0.00	44.2	0.00	0.61	0.98	13.5	22.4	0.6	2.0	2.5	10.1
FAF_c	0.00	45.6	0.00	0.66	0.81	14.6	24.7	0.6	2.4	1.4	8.5
BFS_a	0.00	41.4	0.00	0.48	8.28	3.8	19.7	1.3	0.9	24.6	0.2
C_3S_{typ}	0.00	35.2	0.00	0.07	0.66	0.5	11.8	0.0	0.1	51.2	0.5
C_2S_{typ}	0.00	36.9	0.00	0.07	0.30	1.1	14.7	0.1	0.8	45.4	0.6
C_3A_{typ}	0.00	35.5	0.00	0.74	0.84	16.6	1.7	0.0	0.6	40.4	3.6
C_4AF_{typ}	0.00	35.8	0.00	0.07	1.81	11.6	1.7	0.0	0.2	34.0	15.0

REFERENCES

[1] C. Langton, D.S. Kosson, A.C. Garrabrants, K.G. Brown, Reference cases for use in the Cementitious Barriers Partnership, in, United States, 2009.

[2] J. Arnold, D.S. Kosson, H.A. van der Sloot, R. DeLapp, P. Seignette, A. Garrabrants, K. Brown, Characterization of reference materials and related materials for the Cementitious Barriers Partnership, in, 2010.

[3] H.A. van der Sloot, D.S. Kosson, Use of characterisation leaching tests and associated modelling tools in assessing the hazardous nature of wastes, Journal of Hazardous Materials, 207–208 (2012) 36-43.

[4] D.S. Kosson, A. Garrabrants, H.A. van der Sloot, K.G. Brown, Application of the New US EPA Leaching Environmental Assessment Framework (LEAF) to DOE Environmental Management Challenges - 14383, in: WM'2014, Phoenix, AZ, 2014.

[5] J. Bullard, P. Stutzman, K. Snyder, E. Garboczi, Task 7 Demonstrations of Thames for Microstructure and Transport Properties, in, 2010, pp. Medium: ED.

[6] J.C.L. Meeussen, H.A. van der Sloot, D.S. Kosson, S. Sarkar, Task 7 Demonstration of LeachXS/ORCHESTRA capabilities by simulating constituent release from a cementitious wate form in a reinforced concrete vault, in, 2010, pp. Medium: ED.

[7] E. Samson, Task 7 Demonstration of STADIUM for the performance assessment of concrete low activity waste storage structures, in, SIMCO Technologies, Inc., Quebec, CA, 2010.

[8] K.G. Brown, J. Arnold, S. Sarkar, G. Flach, H.A. van der Sloot, J.C.L. Meeussen, D.S. Kosson, Modeling carbonation of high-level wate tank integrity and closure, European Physics Journal, (2013).

[9] J. Arnold, D.S. Kosson, A. Garrabrants, J.C.L. Meeussen, H.A. van der Sloot, Solution of the nonlinear Poisson–Boltzmann equation: Application to ionic diffusion in cementitious materials, Cement and Concrete Research, 44 (2013) 8-17.

[10] E. Gregoire, E. Samson, Task 10 – Model improvement: Implementation of density and viscosity effects on ionic transport of highly concentrated solutions, in, Cementitious Barriers Partnership, 2012.

[11] S. Sarkar, S. Mahadevan, J.C.L. Meeussen, H. van der Sloot, D.S. Kosson, Numerical simulation of cementitious materials degradation under external sulfate attack, Cement and Concrete Composites, 32 (2010) 241-252.

[12] S. Sarkar, D.S. Kosson, S. Mahadevan, J.C.L. Meeussen, H.v. der Sloot, J.R. Arnold, K.G. Brown, Bayesian calibration of thermodynamic parameters for geochemical speciation modeling of cementitious materials, Cement and Concrete Research, 42 (2012) 889-902.

[13] K.L. Scrivener, A. Nonat, Hydration of cementitious materials, present and future, Cement and Concrete Research, 41 (2011) 651-665.

[14] A. Fick, Ueber Diffusion, Annalen der Physik, 170 (1855) 59-86.

[15] C.I. Steefel, P.C. Lichtner, Multicomponent reactive transport in discrete fractures: I. Controls on reaction front geometry, Journal of Hydrology, 209 (1998) 186-199.

[16] E.C. Gaucher, P. Blanc, J.-M. Matray, N. Michau, Modeling diffusion of an alkaline plume in a clay barrier, Applied Geochemistry, 19 (2004) 1505-1515.

[17] Y. Xi, Z. Bažant, Modeling Chloride Penetration in Saturated Concrete, Journal of Materials in Civil Engineering, 11 (1999) 58-65.

[18] T. Luping, J. Gulikers, On the mathematics of time-dependent apparent chloride diffusion coefficient in concrete, Cement and Concrete Research, 37 (2007) 589-595.

[19] S.J. Kwon, U.J. Na, S.S. Park, S.H. Jung, Service life prediction of concrete wharves with early-aged crack: Probabilistic approach for chloride diffusion, Structural Safety, 31 (2009) 75-83.

[20] K. Audenaert, Q. Yuan, G. De Schutter, On the time dependency of the chloride migration coefficient in concrete, Construction and Building Materials, 24 (2010) 396-402.

[21] N.C.M. Marty, C. Tournassat, A. Burnol, E. Giffaut, E.C. Gaucher, Influence of reaction kinetics and mesh refinement on the numerical modelling of concrete/clay interactions, Journal of Hydrology, 364 (2009) 58-72.

[22] M. Holst, R.E. Kozack, F. Saied, S. Subramaniam, Treatment of electrostatic effects in proteins: Multigrid-based newton iterative method for solution of the full nonlinear poisson–boltzmann equation, Proteins: Structure, Function, and Bioinformatics, 18 (1994) 231-245.

[23] K. Serdar, A. Olaf Sparre, C. Shin-Ho, Models of permeation in ion channels, Reports on Progress in Physics, 64 (2001) 1427.

[24] R.D. Coalson, M.G. Kurnikova, Poisson-Nernst-Planck theory approach to the calculation of current through biological ion channels, NanoBioscience, IEEE Transactions on, 4 (2005) 81-93.

[25] Q. Cai, J. Wang, H.-K. Zhao, R. Luo, On removal of charge singularity in Poisson--Boltzmann equation, The Journal of Chemical Physics, 130 (2009) 145101-145108.

[26] M.S. Kilic, M.Z. Bazant, A. Ajdari, Steric effects in the dynamics of electrolytes at large applied voltages. II. Modified Poisson-Nernst-Planck equations, Physical Review E, 75 (2007) 021503.

[27] M.S. Kilic, M.Z. Bazant, A. Ajdari, Steric effects in the dynamics of electrolytes at large applied voltages. I. Double-layer charging, Physical Review E, 75 (2007) 021502.

[28] M.Z. Bazant, Induced-Charge Electrokinetic Phenomena

Electrokinetics and Electrohydrodynamics in Microsystems, in: A. Ramos (Ed.), Springer Vienna, 2011, pp. 221-297.

[29] M. Schmuck, M.Z. Bazant, Homogenization of the Poisson-Nernst-Planck Equations for Ion Transport in Charged Porous Media, arXiv preprint arXiv:12021916, (2012).

[30] D. Stein, M. Kruithof, C. Dekker, Surface-Charge-Governed Ion Transport in Nanofluidic Channels, Physical Review Letters, 93 (2004) 035901.

[31] A. Plecis, R.B. Schoch, P. Renaud, Ionic Transport Phenomena in Nanofluidics: Experimental and Theoretical Study of the Exclusion-Enrichment Effect on a Chip, Nano Letters, 5 (2005) 1147-1155.

[32] R.B. Schoch, J. Han, P. Renaud, Transport phenomena in nanofluidics, Reviews of Modern Physics, 80 (2008) 839-883.

[33] W. Sparreboom, A. van den Berg, J.C.T. Eijkel, Principles and applications of nanofluidic transport, Nat Nano, 4 (2009) 713-720.

[34] C.A.J. Appelo, L.R. Van Loon, P. Wersin, Multicomponent diffusion of a suite of tracers (HTO, Cl, Br, I, Na, Sr, Cs) in a single sample of Opalinus Clay, Geochimica et Cosmochimica Acta, 74 (2010) 1201-1219.

[35] C.A.J. Appelo, P. Wersin, Multicomponent Diffusion Modeling in Clay Systems with Application to the Diffusion of Tritium, Iodide, and Sodium in Opalinus Clay, Environmental Science & Technology, 41 (2007) 5002-5007.

[36] C. Tournassat, C.A.J. Appelo, Modelling approaches for anion-exclusion in compacted Na-bentonite, Geochimica et Cosmochimica Acta, 75 (2011) 3698-3710.

[37] A. Revil, N. Linde, Chemico-electromechanical coupling in microporous media, Journal of Colloid and Interface Science, 302 (2006) 682-694.

[38] A. Revil, N. Linde, A. Cerepi, D. Jougnot, S. Matthäi, S. Finsterle, Electrokinetic coupling in unsaturated porous media, Journal of Colloid and Interface Science, 313 (2007) 315-327.

[39] A. Revil, D. Jougnot, Diffusion of ions in unsaturated porous materials, Journal of Colloid and Interface Science, 319 (2008) 226-235.

[40] E. Samson, J. Marchand, Numerical Solution of the Extended Nernst-Planck Model, Journal of Colloid and Interface Science, 215 (1999) 1-8.

[41] E. Samson, J. Marchand, K. Snyder, Calculation of ionic diffusion coefficients on the basis of migration test results, Materials and Structures, 36 (2003) 156-165.

[42] O. Truc, J.-P. Ollivier, L.-O. Nilsson, Numerical simulation of multi-species transport through saturated concrete during a migration test — MsDiff code, Cement and Concrete Research, 30 (2000) 1581-1592.

[43] E. Samson, J. Marchand, J.J. Beaudoin, Describing ion diffusion mechanisms in cement-based materials using the homogenization technique, Cement and Concrete Research, 29 (1999) 1341-1345.

[44] K. Krabbenhøft, J. Krabbenhøft, Application of the Poisson–Nernst–Planck equations to the migration test, Cement and Concrete Research, 38 (2008) 77-88.

[45] Q. Liu, L. Li, D. Easterbrook, J. Yang, Multi-phase modelling of ionic transport in concrete when subjected to an externally applied electric field, Engineering Structures, 42 (2012) 201-213.

[46] J. Xia, L.-y. Li, Numerical simulation of ionic transport in cement paste under the action of externally applied electric field, Construction and Building Materials, 39 (2013) 51-59.

[47] K.A. Snyder, J. Marchand, Effect of speciation on the apparent diffusion coefficient in nonreactive porous systems, Cement and Concrete Research, 31 (2001) 1837-1845.

[48] E. Samson, J. Marchand, Modeling the transport of ions in unsaturated cement-based materials, Computers & Structures, 85 (2007) 1740-1756.

[49] J.M. Galíndez, J. Molinero, On the relevance of electrochemical diffusion for the modeling of degradation of cementitious materials, Cement and Concrete Composites, 32 (2010) 351-359.

[50] P. Bescop, B. Lothenbach, E. Samson, K. Snyder, Modeling Degradation of Cementitious Materials in Aggressive Aqueous Environments, in: M. Alexander, A. Bertron, N. De Belie (Eds.) Performance of Cement-Based Materials in Aggressive Aqueous Environments, Springer Netherlands, 2013, pp. 177-218.

[51] G.T. Yeh, V.S. Tripathi, A critical evaluation of recent developments in hydrogeochemical transport models of reactive multichemical components, Water Resources Research, 25 (1989) 93-108.

[52] A.L. Walter, E.O. Frind, D.W. Blowes, C.J. Ptacek, J.W. Molson, Modeling of multicomponent reactive transport in groundwater: 1. Model development and evaluation, Water Resources Research, 30 (1994) 3137-3148.

[53] J. Crank, The Mathematics of Diffusion, Oxford University Press, London, UK, 1975.

[54] J. Bear, Y. Bachmat, Introduction to modeling of transport phenomena in porous media, Springer, 1990.

[55] C. Nicholson, Diffusion and related transport mechanisms in brain tissue, Reports on Progress in Physics, 64 (2001) 815.

[56] E.L. Cussler, Diffusion Mass Transfer in Fluid Systems, 2 ed., Cambridge University Press, New York, 2003.

[57] J.R. Vinograd, J.W. McBain, Diffusion of Electrolytes and of the Ions in their Mixtures, Journal of the American Chemical Society, 63 (1941) 2008-2015.

[58] S. Ben-Yaakov, Diffusion of sea water ions—I. Diffusion of sea water into a dilute solution, Geochimica et Cosmochimica Acta, 36 (1972) 1395-1406.

[59] A.C. Lasaga, Multicomponent exchange and diffusion in silicates, Geochimica et Cosmochimica Acta, 43 (1979) 455-469.

[60] A.C. Lasaga, The treatment of multi-component diffusion and ion pairs in diagenetic fluxes, American Journal of Science, 279 (1979) 324-346.

[61] I. Rubinstein, Electro-diffusion of ions, SIAM, 1990.

[62] J.W. Alexander, On the Decomposition of Tensors, Annals of Mathematics, 27 (1926) 421-423.

[63] J.C.L. Meeussen, ORCHESTRA: An Object-Oriented Framework for Implementing Chemical Equilibrium Models, Environ Sci Technol, 37 (2003) 1175-1182.

[64] C.M. Bethke, Geochemical and Biogeochemical Reaction Modeling, Second ed., Cambridge University Press, New York, 2008.

[65] J.C. Strikwerda, Finite Difference Schemes and Partial Differential Equations, Second Edition ed., Society for Industrial and Applied Mathematics, Philadelphia, 2004.

[66] M. Rudolph, Digital simulations with the fast implicit finite difference (FIFD) algorithm: Part II. An improved treatment of electrochemical mechanisms with second-order reactions, Journal of Electroanalytical Chemistry, 338 (1992) 85-98.

[67] C. Langton, Evaluation of sulfate attack on saltstone vault concrete and saltstone: SIMCO Technologies, Inc. Part 1 Final Report, in, 2008.

[68] USEPA, Draft Method 1315: Mass Transfer Rates in Monolithic and Compacted Granular Materials, in: Test Methods for Evaluating Solid Waste, Physical/Chemical Methods (SW-846), 2012.

[69] C. Carde, G. Escadeillas, A. François, Use of ammonium nitrate solution to simulate and accelerate the leaching of cement pastes due to deionized water, Magazine of Concrete Research, 49 (1997) 295-301.

[70] B. Lothenbach, T. Matschei, G. Möschner, F.P. Glasser, Thermodynamic modelling of the effect of temperature on the hydration and porosity of Portland cement, Cement and Concrete Research, 38 (2008) 1-18.

[71] W. Hummel, U. Berner, E. Curti, F.J. Pearson, T. Thoenen, Nagra/PSI Chemical Thermodynamic Data Base 01/01, Universal Publishers, Parkland, Florida, 2002.

[72] B. Lothenbach, F. Winnefeld, Thermodynamic modelling of the hydration of Portland cement, Cement and Concrete Research, 36 (2006) 209-226.

[73] G. Faure, Principles and Applications of Inorganic Geochemistry, Macmillan Publishing Company, New York, 1991.

[74] E.L. Shock, H.C. Helgeson, Calculation of the thermodynamic and transport properties of aqueous species at high pressures and temperatures: Correlation algorithms for ionic species and equation of state predictions to 5 kb and 1000°C, Geochimica et Cosmochimica Acta, 52 (1988) 2009-2036.

[75] E.L. Shock, D.C. Sassani, M. Willis, D.A. Sverjensky, Inorganic species in geologic fluids: Correlations among standard molal thermodynamic properties of aqueous ions and hydroxide complexes, Geochimica et Cosmochimica Acta, 61 (1997) 907-950.

[76] USEPA, Method 1313: Liquid-solid partitioning as a function of extract pH using a parallel batch extraction procedure, in: Test Methods for Evaluating Solid Waste, Physical/Chemical Methods (SW-846), 2012.

[77] E. Samson, G. Lemaire, J. Marchand, J.J. Beaudoin, Modeling chemical activity effects in strong ionic solutions, Computational Materials Science, 15 (1999) 285-294.

[78] E.H. Oelkers, H.C. Helgeson, Calculation of the thermodynamic and transport properties of aqueous species at high pressures and temperatures: Aqueous tracer diffusion coefficients of ions to 1000°C and 5 kb, Geochimica et Cosmochimica Acta, 52 (1988) 63-85.

[79] H.S. Frank, W.-Y. Wen, Ion-solvent interaction. Structural aspects of ion-solvent interaction in aqueous solutions: a suggested picture of water structure, Discussions of the Faraday Society, 24 (1957) 133-140.

[80] Y. Marcus, Effect of ions on the structure of water: structure making and breaking, Chemical reviews, 109 (2009) 1346-1370.

[81] S. Koneshan, J.C. Rasaiah, R.M. Lynden-Bell, S.H. Lee, Solvent Structure, Dynamics, and Ion Mobility in Aqueous Solutions at 25 °C, The Journal of Physical Chemistry B, 102 (1998) 4193-4204.

[82] CRC Handbook of Chemistry and Physics, in, Taylor and Francis Group, LLC, 2010.

[83] K.A. Snyder, The relationship between the formation factor and the diffusion coefficient of porous materials saturated with concentrated electrolytes: theoretical and experimental considerations, Concrete Science and Engineering, 3 (2001) 216-224.

[84] J. Marchand, B. Gérard, A. Delagrave., Ion transport mechanisms in cement-based materials, Materials Science of Concrete, V (1998) 307–400.

[85] A. Atkinson, A.K. Nickerson, The diffusion of ions through water-saturated cement, Journal of Materials Science, 19 (1984) 3068-3078.

[86] S. Chatterji, M. Kawamura, Electrical double layer, ion transport and reactions in hardened cement paste, Cement and Concrete Research, 22 (1992) 774-782.

[87] S. Goto, D.M. Roy, Diffusion of ions through hardened cement pastes, Cement and Concrete Research, 11 (1981) 751-757.

[88] S. Chatterji, Transportation of ions through cement based materials. Part 3 experimental evidence for the basic equations and some important deductions, Cement and Concrete Research, 24 (1994) 1229-1236.

[89] E. Nägele, The zeta-potential of cement, Cement and Concrete Research, 15 (1985) 453-462.

[90] E. Nägele, The Zeta-potential of cement: Part II: Effect of pH-value, Cement and Concrete Research, 16 (1986) 853-863.

[91] E. Nägele, U. Schneider, The zeta - potential of cement: Part IV. Effect of simple salts, Cement and Concrete Research, 17 (1987) 977-982.

[92] S. Chatterji, Colloid Electrochemistry of Saturated Cement Paste and Some Properties of Cement Based Materials, Advanced Cement Based Materials, 7 (1998) 102-108.

[93] D.L. Chapman, A Contribution to the Theory of Electrocapillarity, Philos Mag, 25 (1913).

[94] P. Debye, E. Hückel, De la theorie des electrolytes. I. Abaissement du point de congelation et phenomenes associes, Physikalische Zeitschrift, 24 (1923) 185-206.

[95] M. Gouy, Sur la constitution de la charge electrique a la surface d'un electrolyte, Journal de physique theorique et appliquee, 9 (1910) 457-468.

[96] G.R. Dutt, P.F. Low, Diffusion of Alkali Chlorides in Clay-Water Systems, Soil Science, 93 (1962) 233-240.

[97] P.N. Sen, Unified model of conductivity and membrane potential of porous media, Physical Review B, 39 (1989) 9508.

[98] A. Revil, Ionic Diffusivity, Electrical Conductivity, Membrane and Thermoelectric Potentials in Colloids and Granular Porous Media: A Unified Model, Journal of Colloid and Interface Science, 212 (1999) 503-522.

[99] T. Kozaki, K. Inada, S. Sato, H. Ohashi, Diffusion mechanism of chloride ions in sodium montmorillonite, Journal of Contaminant Hydrology, 47 (2001) 159-170.

[100] F.T. Madsen, Clay mineralogical investigations related to nuclear waste disposal, Clay Minerals, 33 (1998) 109-129.

[101] M. Ochs, B. Lothenbach, H. Wanner, H. Sato, M. Yui, An integrated sorption–diffusion model for the calculation of consistent distribution and diffusion coefficients in compacted bentonite, Journal of Contaminant Hydrology, 47 (2001) 283-296.

[102] I.C. Bourg, G. Sposito, A.C.M. Bourg, Modeling Cation Diffusion in Compacted Water-Saturated Sodium Bentonite at Low Ionic Strength, Environmental Science & Technology, 41 (2007) 8118-8122.

[103] L.R. Van Loon, M.A. Glaus, W. Müller, Anion exclusion effects in compacted bentonites: Towards a better understanding of anion diffusion, Applied Geochemistry, 22 (2007) 2536-2552.

[104] H. Friedmann, O. Amiri, A. Aït-Mokhtar, Physical modeling of the electrical double layer effects on multispecies ions transport in cement-based materials, Cement and Concrete Research, 38 (2008) 1394-1400.

[105] R.S. Barneyback, S. Diamond, Expression and analysis of pore fluids from hardened cement pastes and mortars, Cement and Concrete Research, 11 (1981) 279-285.

[106] E. Samson, Personal communication, in, 2011.

[107] F. Moro, H. Bohni, Ink-Bottle Effect in Mercury Intrusion Porosimetry of Cement-Based Materials, Journal of Colloid and Interface Science, 246 (2002) 135-149.

[108] S. Brunauer, P.H. Emmett, E. Teller, Adsorption of Gases in Multimolecular Layers, Journal of the American Chemical Society, 60 (1938) 309-319.

[109] ASTM C 642, Standard Test Method for Density, Absorption, and Voids in Hardened Concrete, in: Annual Book of ASTM Standards, American Society for Testing and Materials, Philadelphia, 2002.

[110] A.W. Adamson, A.P. Gast, Physical Chemistry of Surfaces, Sixth ed., Wiley-Interscience, New York, 1997.

[111] O. Stern, Zur Theorie der Electrolytischen Doppelshicht, Z Electrochem, 30 (1924) 508-516.

[112] D.C. Grahame, The Electrical Double Layer and the Theory of Electrocapillarity, Chemical Reviews, 41 (1947) 441-501.

[113] K. Andersson, B. Allard, M. Bengtsson, B. Magnusson, Chemical composition of cement pore solutions, Cement and Concrete Research, 19 (1989) 327-332.

[114] A. Nicholls, B. Honig, A rapid finite difference algorithm, utilizing successive over-relaxation to solve the Poisson–Boltzmann equation, Journal of Computational Chemistry, 12 (1991) 435-445.

[115] H. Viallis-Terrisse, A. Nonat, J.-C. Petit, Zeta-Potential Study of Calcium Silicate Hydrates Interacting with Alkaline Cations, Journal of Colloid and Interface Science, 244 (2001) 58-65.

[116] Y. Elakneswaran, T. Nawa, K. Kurumisawa, Electrokinetic potential of hydrated cement in relation to adsorption of chlorides, Cement and Concrete Research, 39 (2009) 340-344.

[117] Y. Elakneswaran, A. Iwasa, T. Nawa, T. Sato, K. Kurumisawa, Ion-cement hydrate interactions govern multi-ionic transport model for cementitious materials, Cement and Concrete Research, 40 (2010) 1756-1765.

[118] S.-Y. Hong, F.P. Glasser, Alkali binding in cement pastes: Part I. The C-S-H phase, Cement and Concrete Research, 29 (1999) 1893-1903.

[119] S.-Y. Hong, F.P. Glasser, Alkali sorption by C-S-H and C-A-S-H gels: Part II. Role of alumina, Cement and Concrete Research, 32 (2002) 1101-1111.

[120] T. Luping, L.-O. Nilsson, Chloride binding capacity and binding isotherms of OPC pastes and mortars, Cement and Concrete Research, 23 (1993) 247-253.

[121] W. Chen, H.J.H. Brouwers, Alkali binding in hydrated Portland cement paste, Cement and Concrete Research, 40 (2010) 716-722.

[122] D. Smith, P. Pivonka, C. Jungnickel, S. Fityus, Theoretical Analysis of Anion Exclusion and Diffusive Transport Through Platy-Clay Soils, Transport in Porous Media, 57 (2004) 251-277.

[123] S. Kaufhold, M. Plötze, M. Klinkenberg, R. Dohrmann, Density and porosity of bentonites, Journal of Porous Materials, (2012) 1-18.

[124] R.H. Nilson, S.K. Griffiths, Influence of atomistic physics on electro-osmotic flow: An analysis based on density functional theory, The Journal of Chemical Physics, 125 (2006) 164510-164513.

[125] M.B. Haha, K. De Weerdt, B. Lothenbach, Quantification of the degree of reaction of fly ash, Cement and Concrete Research, 40 (2010) 1620-1629.

[126] V. Kocaba, E. Gallucci, K.L. Scrivener, Methods for determination of degree of reaction of slag in blended cement pastes, Cement and Concrete Research, 42 (2012) 511-525.

[127] F. Deschner, F. Winnefeld, B. Lothenbach, S. Seufert, P. Schwesig, S. Dittrich, F. Goetz-Neunhoeffer, J. Neubauer, Hydration of Portland cement with high replacement by siliceous fly ash, Cement and Concrete Research.

[128] R. Yang, N.R. Buenfeld, Binary segmentation of aggregate in SEM image analysis of concrete, Cement and Concrete Research, 31 (2001) 437-441.

[129] C. Langton, H. Burns, D. Stefanko, Cementitious grout for closing SRS high level waste tanks - #12315, 2012.

[130] D.P. Bentz, P.E. Stutzman, C.J. Haecker, S. Remonds, SEM/X-ray imaging of cement-based materials, in: H.S. Pietersen, J.A. Larbi, H.H.A. Janssen (Eds.) 7th Euroseminar on Microscopy Applied to Building Materials, Delft University of Technology, 1999, pp. 457-466.

[131] J.W. Bullard, P.E. Stutzman, Analysis of CCRL proficiency cements 151 and 152 using the Virtual Cement and Concrete Testing Laboratory, Cement and Concrete Research, 36 (2006) 1548-1555.

[132] R.A. Fisher, Sir, The Use of Multiple Measurements in Taxonomic Problems, Annals of Eugenics, 7 (1936) 179-188.

[133] C. Fraley, A.E. Raftery, How Many Clusters? Which Clustering Method? Answers Via Model-Based Cluster Analysis, The Computer Journal, 41 (1998) 578-588.

[134] ASTM C150, Standard Specification for Portland Cement, in: Annual Book of ASTM Standards, American Society for Testing and Materials, Philadelphia, 2002a.

[135] ASTM C 989, Standard Specification for Ground Granulated Blast Furnace Slag for Use in Concrete and Mortars, in: Annual Book of ASTM Standards, American Society for Testing and Materials, Philadelphia, 1999.

[136] ASTM C 618, Standard Specification for Coal Fly Ash and Raw or Calcined Natural Pozzolan for Use as a Mineral Admixture in Concrete, in: Annual Book of ASTM Standards, American Society for Testing and Materials, Philadelphia, 2005.

[137] ASTM C 33, Standard Specification for Concrete Aggregates, in: Annual Book of ASTM Standards, American Society for Testing and Materials, Philadelphia, 2002a.

[138] E.J. Garboczi, K. Snyder, Personal communication, in, 2012.

[139] M.D. McKay, R.J. Beckman, W.J. Conover, Comparison of Three Methods for Selecting Values of Input Variables in the Analysis of Output from a Computer Code, Technometrics, 21 (1979) 239-245.

[140] K. Kanaya, S. Okayama, Penetration and energy-loss theory of electrons in solid targets, Journal of Physics D: Applied Physics, 5 (1972) 43.

[141] P. Hovington, D. Drouin, R. Gauvin, CASINO: A new monte carlo code in C language for electron beam interaction —part I: Description of the program, Scanning, 19 (1997) 1-14.

[142] H.S. Wong, N.R. Buenfeld, Monte Carlo simulation of electron-solid interactions in cement-based materials, Cement and Concrete Research, 36 (2006) 1076-1082.

[143] J. Delon, A. Desolneux, J.L. Lisani, A.B. Petro, A Nonparametric Approach for Histogram Segmentation, Image Processing, IEEE Transactions on, 16 (2007) 253-261.

[144] R.E. Barlow, Statistical inference under restrictions; the theory and application of isotonic regression, Wiley, New York, 1972.

[145] J.I. Goldstein, C.E. Lyman, D.E. Newbury, E. Lifshin, P. Echlin, L. Sawyer, D.C. Joy, J.R. Michael, Scanning Electron Microscopy and X-Ray Microanalysis, 3rd ed., Kluwer Academic / Plenum Publishers, New York, 2003.

[146] K.L. Scrivener, Backscattered electron imaging of cementitious microstructures: understanding and quantification, Cement and Concrete Composites, 26 (2004) 935-945.

[147] N. Otsu, A threshold selection method from gray-level histograms, Automatica, 11 (1975) 23-27.

[148] P. Perona, J. Malik, Scale-space and edge detection using anisotropic diffusion, Pattern Analysis and Machine Intelligence, IEEE Transactions on, 12 (1990) 629-639.

[149] L.A. Zadeh, Fuzzy sets, Information and Control, 8 (1965) 338-353.

[150] F. Murtagh, A.E. Raftery, Fitting straight lines to point patterns, Pattern Recognition, 17 (1984) 479-483.

[151] J.D. Banfield, A.E. Raftery, Model-based Gaussian and non-Gaussian clustering, Biometrics, 49 (1993) 803-821.

[152] C. Fraley, A.E. Raftery, MCLUST: Software for Model-Based Cluster Analysis, Journal of Classification, 16 (1999) 297-306.

[153] C. Fraley, Algorithms for Model-Based Gaussian Hierarchical Clustering, SIAM Journal on Scientific Computing, 20 (1998) 270-281.

[154] A.P. Dempster, N.M. Laird, D.B. Rubin, Maximum likelihood from incomplete data via the EM algorithm, Journal of the Royal Statistical Society Series B (Methodological), (1977) 1-38.

[155] G. Schwarz, Estimating the dimension of a model, The annals of statistics, 6 (1978) 461-464.

[156] R Development Core Team, R: A language and environment for statistical computing, R Foundation Statistical Computing, (2008).

[157] A.R. Martinez, W.L. Martinez, Model-based clustering toolbox for MATLAB, Naval Surface Warfare Center, Dahlgren Division, Tech Rep, (2004).

[158] C. Fraley, A.E. Raftery, Model-Based Clustering, Discriminant Analysis, and Density Estimation, Journal of the American Statistical Association, 97 (2002) 611-631.

[159] A. Meunier, B. Velde, Illite: Origins, Evolution and Metamorphism, Springer, New York, 2004.

[160] S.P. Schweinfurth, R.B. Finkelman, Coal--a complex natural resource: an overview of factors affecting coal quality and use in the United States, US Dept. of the Interior, US Geological Survey, 2003.

[161] K.A. Snyder, P.E. Stutzman, J. Philip, D. Esh, Hydrated phases and pore solution composition in cement-solidified saltstone waste forms, EPJ Web of Conferences, 56 (2013) 01001.

[162] H.F.W. Taylor, Cement chemistry, T. Telford, London, 1997.

[163] G. Le Saoût, M. Ben Haha, F. Winnefeld, B. Lothenbach, Hydration Degree of Alkali-Activated Slags: A 29Si NMR Study, Journal of the American Ceramic Society, 94 (2011) 4541-4547.

[164] D. Damidot, B. Lothenbach, D. Herfort, F.P. Glasser, Thermodynamics and cement science, Cement and Concrete Research, 41 (2011) 679-695.

[165] D.S. Kosson, L. Stefanski, R. Delapp, P.F.A.B. Seignette, H. van der Sloot, P. Kariher, M. Baldwin, Interlaboratory Validation of the Leaching Environmental Assessment Framework (LEAF) Method 1313 and Method 1316, in, USEPA Office of Research and Development, 2012.

[166] D.A. Kulik, M. Kersten, Aqueous Solubility Diagrams for Cementitious Waste Stabilization Systems: II, End-Member Stoichiometries of Ideal Calcium Silicate Hydrate Solid Solutions, Journal of the American Ceramic Society, 84 (2001) 3017-3026.

[167] J.J. Thomas, H.M. Jennings, A.J. Allen, The surface area of cement paste as measured by neutron scattering: evidence for two C-S-H morphologies, Cement and Concrete Research, 28 (1998) 897-905.

[168] C. Labbez, I. Pochard, B. Jönsson, A. Nonat, C-S-H/solution interface: Experimental and Monte Carlo studies, Cement and Concrete Research, 41 (2011) 161-168.

[169] I.G. Richardson, G.W. Groves, The incorporation of minor and trace elements into calcium silicate hydrate (C-S-H) gel in hardened cement pastes, Cement and Concrete Research, 23 (1993) 131-138.

[170] B. Lothenbach, K. Scrivener, R.D. Hooton, Supplementary cementitious materials, Cement and Concrete Research, 41 (2011) 1244-1256.

[171] M. Regourd, J.H. Thomassin, P. Baillif, J.C. Touray, Blast-furnace slag hydration. Surface analysis, Cement and Concrete Research, 13 (1983) 549-556.

[172] B. Lothenbach, Thermodynamic equilibrium calculations in cementitious systems, Materials and Structures, 43 (2010) 1413-1433.

[173] P. Faucon, T. Charpentier, A. Nonat, J.C. Petit, Triple-Quantum Two-Dimensional 27Al Magic Angle Nuclear Magnetic Resonance Study of the Aluminum Incorporation in Calcium Silicate Hydrates, Journal of the American Chemical Society, 120 (1998) 12075-12082.

[174] G.K. Sun, J.F. Young, R.J. Kirkpatrick, The role of Al in C–S–H: NMR, XRD, and compositional results for precipitated samples, Cement and Concrete Research, 36 (2006) 18-29.

[175] X. Pardal, I. Pochard, A. Nonat, Experimental study of Si–Al substitution in calcium-silicate-hydrate (C-S-H) prepared under equilibrium conditions, Cement and Concrete Research, 39 (2009) 637-643.

[176] C. Zevenbergen, L.P. Van Reeuwijk, J.P. Bradley, R.N.J. Comans, R.D. Schuiling, Weathering of MSWI bottom ash with emphasis on the glassy constituents, Journal of Geochemical Exploration, 62 (1998) 293-298.

[177] C. Zevenbergen, P. Van Reeuwijk, J.P. Bradley, P. Bloemen, R.N.J. Comans, Mechanism and conditions of clay formation during natural weathering of MSWI bottom ash, Clays and Clay Minerals, 44 (1996) 546-552.

[178] R.C. Routson, J.A. Kittrick, Illite Solubility1, Soil Sci Soc Am J, 35 (1971) 714-718.

[179] D.R.M. Brew, F.P. Glasser, Synthesis and characterisation of magnesium silicate hydrate gels, Cement and Concrete Research, 35 (2005) 85-98.

[180] C.A. Langton, P.B. Wong, Properties of slag concrete for low-level waste containment, in, United States, 1991, pp. Size: Pages: (12 p).

[181] C.A. Langton, Slag-based saltstone formulations, in, United States, 1987, pp. Pages: 8.

[182] A.R. Brough, A. Katz, G.K. Sun, L.J. Struble, R.J. Kirkpatrick, J.F. Young, Adiabatically cured, alkali-activated cement-based wasteforms containing high levels of fly ash: Formation of zeolites and Al-substituted C-S-H, Cement and Concrete Research, 31 (2001) 1437-1447.

[183] H.A. van der Sloot, Comparison of the characteristic leaching behavior of cements using standard (EN 196-1) cement mortar and an assessment of their long-term environmental behavior

in construction products during service life and recycling, Cement and Concrete Research, 30 (2000) 1079-1096.

[184] H.A. van der Sloot, Characterization of the leaching behaviour of concrete mortars and of cement-stabilized wastes with different waste loading for long term environmental assessment, Waste Management, 22 (2002) 181-186.

[185] H.A. van der Sloot, P. Seignette, R.N.J. Comans, A.v. Zomeren, J.J. Dijkstra, H. Meeussen, D.S. Kosson, O. Hjelmar, Evaluation of environmental aspects of alternative materials using an integrated approach assisted by a database/expert system, in: Advances in Waste Management & Recycling, Dundee, Scotland, 2003, pp. 769-790.

[186] C.J. Engelsen, H.A. van der Sloot, G. Wibetoe, G. Petkovic, E. Stoltenberg-Hansson, W. Lund, Release of major elements from recycled concrete aggregates and geochemical modelling, Cement and Concrete Research, 39 (2009) 446-459.

[187] H.A. van der Sloot, D.S. Kosson, A.C. Garrabrants, J. Arnold, The Impact of Coal Combustion Fly Ash Used as a Supplemental Cementitious Material on the Leaching Constituents from Cements and Concretes, in, USEPA, 2012.

[188] H.A. van der Sloot, A. van Zomeren, J.C.L. Meeussen, D. Hoede, R.P.J.J. Rietra, R. Stenger, T. Lang, M. Schneider, G. Spanka, E. Stoltenberg-Hansson, A. Lerat, P. Dath, Environmental Criteria for Cement Based Products, in, ECN, Petten, The Netherlands, 2011.

[189] D.S. Kosson, H.A. van der Sloot, F. Sanchez, A.C. Garrabrants, An Integrated Framework for Evaluating Leaching in Waste Management and Utilization of Secondary Materials, Environmental Engineering Science, 19 (2002) 159-204.

[190] T. Matschei, B. Lothenbach, F.P. Glasser, Thermodynamic properties of Portland cement hydrates in the system CaO-Al2O3-SiO2-CaSO4-CaCO3-H2O, Cement and Concrete Research, 37 (2007) 1379-1410.

[191] I. Lognot, I. Klur, A. Nonat, NMR and Infrared Spectroscopies of C-S-H and Al-Substituted C-S-H Synthesised in Alkaline Solutions, in: P. Colombet, H. Zanni, A.-R. Grimmer, P. Sozzani (Eds.) Nuclear Magnetic Resonance Spectroscopy of Cement-Based Materials, Springer Berlin Heidelberg, 1998, pp. 189-196.

[192] T. Chappex, K. Scrivener, Alkali fixation of C–S–H in blended cement pastes and its relation to alkali silica reaction, Cement and Concrete Research, 42 (2012) 1049-1054.

[193] M. Codina, C. Cau-dit-Coumes, P. Le Bescop, J. Verdier, J.P. Ollivier, Design and characterization of low-heat and low-alkalinity cements, Cement and Concrete Research, 38 (2008) 437-448.

[194] J.L. Loeppky, J. Sacks, W.J. Welch, Choosing the Sample Size of a Computer Experiment: A Practical Guide, Technometrics, 51 (2009) 366-376.

[195] D.M.R. Brew, F.P. Glasser, The magnesia–silica gel phase in slag cements: alkali (K, Cs) sorption potential of synthetic gels, Cement and Concrete Research, 35 (2005) 77-83.

[196] I.G. Richardson, A.R. Brough, R. Brydson, G.W. Groves, C.M. Dobson, Location of Aluminum in Substituted Calcium Silicate Hydrate (C-S-H) Gels as Determined by 29Si and 27Al NMR and EELS, Journal of the American Ceramic Society, 76 (1993) 2285-2288.

[197] A. Hidalgo, S. Petit, C. Domingo, C. Alonso, C. Andrade, Microstructural characterization of leaching effects in cement pastes due to neutralisation of their alkaline nature: Part I: Portland cement pastes, Cement and Concrete Research, 37 (2007) 63-70.

[198] I.G. Richardson, A.R. Brough, G.W. Groves, C.M. Dobson, The characterization of hardened alkali-activated blast-furnace slag pastes and the nature of the calcium silicate hydrate (C-S-H) phase, Cement and Concrete Research, 24 (1994) 813-829.

[199] R. Taylor, I.G. Richardson, R.M.D. Brydson, Composition and microstructure of 20-year-old ordinary Portland cement–ground granulated blast-furnace slag blends containing 0 to 100% slag, Cement and Concrete Research, 40 (2010) 971-983.

[200] J.J. Dijkstra, H.A. van der Sloot, R.N.J. Comans, The leaching of major and trace elements from MSWI bottom ash as a function of pH and time, Applied Geochemistry, 21 (2006) 335-351.